THE EFFECT OF STRAND ARCHITECTURE ON THE FRACTURE PROPENSITY OF Nb_3Sn COMPOSITE WIRES

by

MATTHEW C. JEWELL

A dissertation submitted in partial fulfillment

of the requirements for the degree of

DOCTOR OF PHILOSOPHY

(MATERIALS SCIENCE)

UNIVERSITY OF WISCONSIN – MADISON

2008

© Copyright by Matthew C. Jewell 2008
Free redistribution is allowed under the terms of the GNU Free Documentation License, version 1.2 or higher.

EXECUTIVE SUMMARY

With apologies to J.M. Pfotenhauer

Two mice went for a stroll one day
Their pace it was quite slack.
I say, said One, *I'm rather glum*
My strand has got a crack!

I know, said Two, *I've been there too!*
Your J_c's low again.
That phase ain't tough – it's brittle stuff
It's N-B-3-S-N.

But if, said Two, *we took a view*
Of what's inside that strand.
We might learn 'bout the structures there
And make the design planned.

I see said One, *that sounds like fun*
Let me just think a bit.
The fil'ment spacing, size, and shape
Are factors we might get.

Agreed, said Two, *although it's true*
To get topography,
We'll need to open up the strand
With metallography.

You're right, said One, *I'm back to glum*
That's after all not fun.
But as they say – the easy things
Have already been done…

The truth of the flower is, not the facts about it, be they correct as ideal science itself, but the shining, glowing, gladdening, patient thing throned on its stalk – the compeller of smile and tear.

- George MacDonald

Test everything; hold fast to what is good.

- I Thessalonians 5:21

ACKNOWLEDGEMENTS

I am very grateful to the many individuals and institutions that have invested in my graduate career over the past five and a half years. Financially, I have been supported throughout my graduate career by the U.S. Department of Energy Office of High Energy Physics and the Office of Fusion Energy Sciences. Significant funding for this thesis work has also been supplied by the ITER International Organization, for which I am most grateful. Earlier in my graduate career, I benefited from my position as a UW University Fellow and also as a K-through-infinity Graduate Fellow, funded by the National Science Foundation. The latter experience (which included teaching 8th grade science for a year at Wright Middle School in Madison, WI) was a formative experience in my intellectual development, and I am grateful to the many individuals that managed such a high quality systemic KTI initiative at UW-Madison, including Eileen Callahan with the UW Graduate School, and Lisa Wachtel with the Madison Metropolitan School District.

Good science, of course, requires relationships in addition to funding. My advisor, David Larbalestier, has faithfully shepherded me through five and a half years of graduate school and has been a constant source of wisdom, wit, and good cheer as we have pursued our research efforts in both Madison and Tallahassee. I realize now the extent to which I, as a senior undergraduate student, was ill-equipped to make a cogent choice of thesis advisor – but make the right choice I did. Peter Lee is the most exceptional microscopist I have ever met and has taught me everything I know about acquiring photomicrographs and finding joy in both a beautiful image and a beautiful Excel macro. Bill Starch has been an invaluable

help in keeping our furnaces and metallography labs running, performing machining magic at 4:30pm on a Friday, and teaching me to identify a ¼-inch #20 socket cap screw by sight. I'm graduating now, Bill, so you can retire. You have my permission. Bob Goddard has faithfully, and at times heroically, maintained the two scanning electron microscopes without which I would have neither a thesis nor the 2,900 images on which it is based. The many graduate students who have gone before me have made my road much smoother. I am grateful in particular to Mike Naus, Arno Godeke, and Ben Senkowicz, for both their science and their friendship.

The broader low-temperature superconductivity community of which I am a part has been a very significant factor in my professional development. I am grateful to Lance Cooley for his novel insights into every problem I have ever brought to him, to Bruce Strauss for teaching me to be a *professional* scientist, and to Neil Mitchell and Arnaud Devred at ITER for helping to make this thesis a project with some real utility for real magnets. I am also indebted to the Low Temperature Superconductivity Workshop community for their many fruitful interactions.

It is customary, in the acknowledgements section of a thesis, to thank one's family for their support and encouragement. In my case, a note of thanks is hardly sufficient to convey my appreciation to and deep love for my wife, children, and extended family who have endured – and persevered – through the inevitable trials of any graduate career. It wouldn't have happened without you – I love you all.

Matthew C. Jewell

Madison, WI, August 2008

THE EFFECT OF STRAND ARCHITECTURE ON THE FRACTURE PROPENSITY OF Nb_3Sn COMPOSITE WIRES

Matthew C. Jewell

Under the Supervision of Professor David C. Larbalestier

University of Wisconsin - Madison

Nb_3Sn is a brittle superconducting material used to carry electric current in large fusion and high energy physics magnets. Usually fabricated in the form of a composite multifilamentary wire, Nb_3Sn strands can be susceptible to filament-level fracture under Lorentz forces during magnet operation. This can lead to degradation of the critical electric current density and subsequent underperformance of the magnet. To understand the effect of strand architecture (filament size, spacing, and arrangement) on fracture propensity, we have developed a metallographic technique to image Nb_3Sn strands in longitudinal cross-section after mechanical and/or electrical testing. Deformation conditions included pure bending at 77 K, uniaxial tension at 4.2 K, electromagnetic (TARSIS) testing at 4.2 K, and microindentation at room temperature. Under bend strain, ITER-style strands exhibit primarily individual filament cracking, with some collective cracking occurring in internal tin strands that have agglomerated filaments near the sub-bundle core. This cracking occurred primarily at local bend strain values above 0.7% for strands with reacted filaments of 3 – 4 μm diameter, and at local bend strain values above 0.4% for strands with reacted filaments of 6 μm diameter. The high energy physics strands, by contrast, exhibited long, collective cracks under bending

that propagated across entire sub-bundles and even from sub-bundle to sub-bundle, beginning at the tensile bend axis and ending near the geometric neutral bend axis. Additionally, the fracture morphology is shown to be constant for a wide variety of HEP strands, with critical current density values ranging from 1700 A/mm^2 to 3000 A/mm^2.

Under electromechanical loading in the TARSIS apparatus at the University of Twente, the most significant strain sensitivity (i.e. the fastest degradation of critical current with applied load) was shown to occur in those strands with the most agglomerated filament structures, which also had the most collective (non-cumulative) fracture pattern.

Under indentation testing, crack propagation was shown to be a strong function of the local strain state, with even small tensile stresses producing extended fracture fields, while indents in a region under compressive stress showed almost no fracture at all. The clear implication is that the local stress state is the most critical parameter to be controlled for preventing fracture in the conductor. These findings should provide significant guidance to the Nb_3Sn wire manufacturing community as they develop more fracture-resistant strands for magnet applications.

TABLE OF CONTENTS

CHAPTER 1 – Nb_3Sn AS A CONDUCTOR FOR HIGH FIELD MAGNETS

1.1 The ITER fusion reactor

Because they can conduct electricity without any resistive loss, superconducting materials have been used as conductors for electromagnet windings since 1954, when G.B. Yntema built a 4296-turn solenoid using 50 micron (μm) diameter cold-worked Nb wire [1]. That simple conductor carried 1.8 amps (A) and generated 0.71 Tesla (T) in the magnet. Today, superconducting magnets enable technologies as diverse as magnetic resonance imaging (MRI) [2] equipment at 1 – 3 T, magnetic confinement nuclear fusion reactors at 5 – 13 T [3, 4], particle accelerator dipoles [5] and quadrupoles [6] at 5 – 16 T, and nuclear magnetic resonance imaging (NMR) [7] equipment at 18 – 21 T. By far the most ambitious (in terms of scale and cost) superconducting magnet system currently under development is the ITER nuclear fusion reactor [8], an experimental magnetic confinement reactor being constructed in the south of France under a seven-party multinational agreement. ITER (formerly an acronym for International Thermonuclear Experimental Reactor), which is scheduled to begin burning plasma in 2018, is designed to be the first fusion reactor to achieve a net energy gain, with a Q factor (the ratio of energy output to energy input) greater than or equal to ten, with sustained a power output of 500 MW [9]. With an anticipated

plasma burn time of > 300 seconds (s) and a plasma volume of 837 m^3, ITER will also provide critical large-scale experimental magnetohydrodynamic plasma information that will enable the continued refinement of the magnetic confinement scheme. If successful on both these fronts, ITER will pave the way for the development of commercial energy production via fusion.

1.2 The ITER superconducting magnet system

Nuclear fusion is a process whereby the nuclei of small atoms (usually isotopes of hydrogen) combine to form a larger atom. This reaction is the most energy-dense exothermic reaction known in the universe, and indeed it is the mechanism powering both the sun and many modern nuclear weapons. With 17.6 MeV liberated by each fusion event in a deuterium-tritium reaction (3.5 MeV as heat, 14.1 MeV as a fast neutron), fusion is also prized as a future peaceful energy source for humans, since the fuel precursor (hydrogen) is abundant and the waste products (helium and free neutrons) are considerably more benign than those of a nuclear fission reaction involving uranium and other heavy metal isotopes.

The most significant challenge associated with generating and controlling a fusion reaction for energy extraction is creating the necessary conditions for fusion to occur. On the sun, enormous gravitational forces produce a plasma

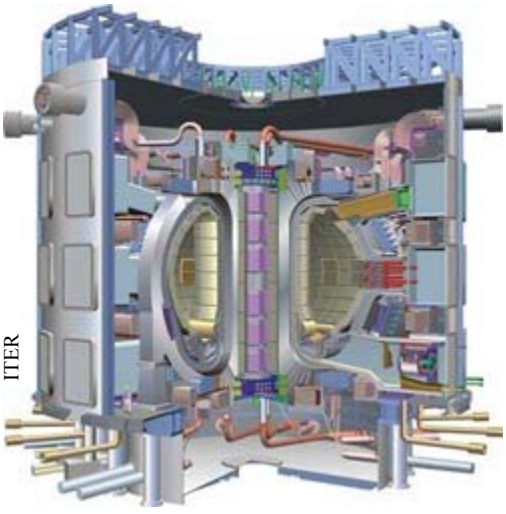

Figure 1.1 Cut-away view [10] of the ITER magnetic confinement fusion reactor. The plasma circulates in the toroidal (doughnut-shaped) vacuum chamber shown here.

density that, combined with a temperature over 10,000,000 Kelvin (K), allows fusion to proceed in a controlled fashion. Here on the earth, generation of similar plasma densities is impossible, forcing plasma physicists to rely on further increases in the plasma temperature – to over 100,000,000 K – to produce a sustained fusion reaction. This approach raises an obvious containment question, for which the most promising solution is magnetic confinement. In this scheme, the plasma is trapped in a toroid-shaped magnetic field and allowed to circulate in an annular fashion. As the fusion reaction progresses, the free neutrons liberated by the reaction strike the wall of the containment vessel and, in a power plant design (which ITER is not), could subsequently be used to turn water into steam and generate electric power.

ITER confines and drives plasma using a tokomak design (see figure 1.1) [10], in which an oscillating central solenoid (CS) magnet system drives the plasma, while toroidal field (TF) and poloidal field (PF) magnets confine and shape the plasma. The technical parameters of these three systems are outlined in table 1.1 [11,12,13]. As indicated, ITER will require approximately 237 tons of superconducting NbTi wire and 516 tons of superconducting Nb_3Sn wire, with a cost (for the latter) of almost 400 M€. This will make ITER, upon construction, one of the largest and most expensive superconducting magnet systems in the world. Since Nb_3Sn wire does not have a consistent large-scale commercial

Table 1.1 Technical parameters of the ITER superconducting magnet systems

	Peak field (T)	**Operating current (kA)**	**Conductor choice**	**Mass of conductor required (tons)**	**Estimated cost of conductor procurement (M€)**
PF	6.0	45	NbTi	237	N/A
CS	12.5	41.5	Nb_3Sn	123	94
TF	11.8	68	Nb_3Sn	393	300

application (as does NbTi wire for MRI machines), these procurement goals will require increasing the world-wide output of Nb_3Sn by a factor of five by 2011.

1.3 Nb_3Sn as a conductor for ITER magnet systems

The ITER toroidal field and central solenoid magnet systems will use Nb_3Sn composite wires to carry supercurrent and generate the required magnetic field. Nb_3Sn was chosen for a combination of superconducting properties, fabricability, and cost. The most common (and cheapest) superconductor for magnet applications, NbTi, with an upper critical field ($\mu_0 H_{c2}$) near 12 T at 0 K, is incapable of producing the fields required by the TF and CS systems. Other high-field superconductors, such as MgB_2, Nb_3Al, $YBa_2Cu_3O_{7-x}$, and Bi-based superconductors, are unable to be fabricated with the current densities, piece length, scale, and cost required by a project the size of ITER. Nb_3Sn, with a $\mu_0 H_{c2}$ of 30 T at 0 K and a critical temperature of 18.3 K [14], matches well with the operating envelope of the ITER magnet systems (H_{max} = 13 T; T = 4.5 K). This point is demonstrated in figure 1.2 [15],

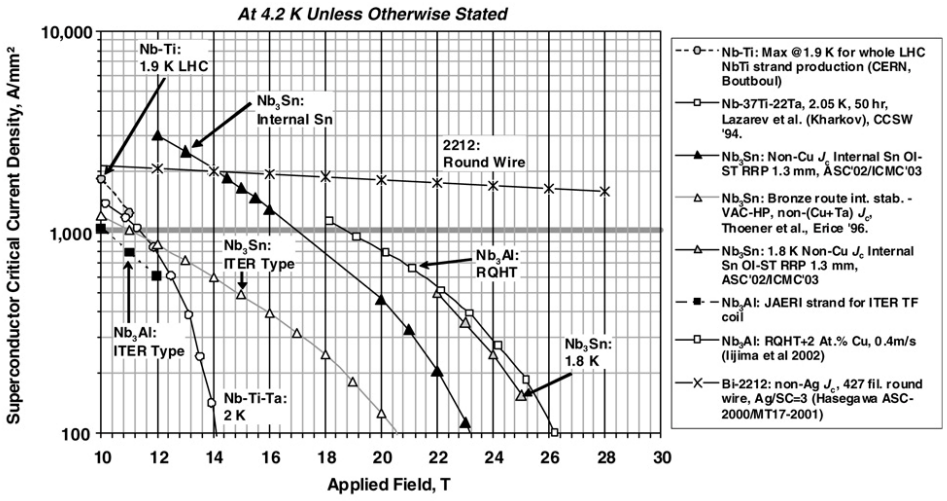

Figure 1.2 Critical current densities available for superconductors with low-temperature applications, as a function of magnetic field. Note that Nb_3Sn is surpassed by both Nb_3Al and Bi-2212 round wire, but these technologies are too immature and too expensive to fulfill a major conductor procurement such as ITER. Adapted from [15].

which shows the critical current densities available (at 4.2 K) for a variety of superconducting materials as a function of magnetic field.

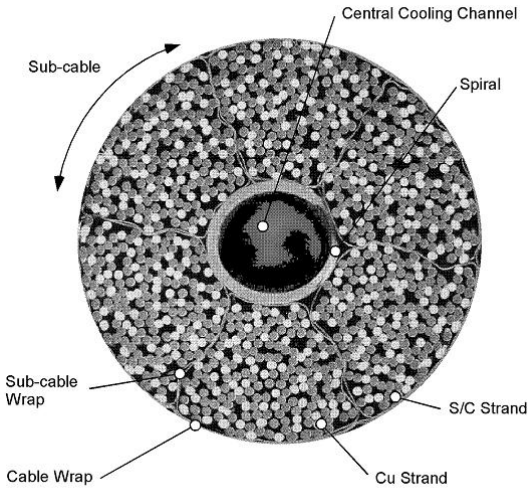

Figure 1.3 A representative CIC conductor, using mixed superconducting and pure Cu strands. Note the significant void fraction within the strand bundle, allowing for more intimate contact with liquid helium.

Nb_3Sn strand for ITER will be cabled into a cable-in-conduit (CIC) configuration. While each magnet system (TF and CS) has a unique design (currently being finalized), both consist of approximately 1000 superconducting Nb_3Sn strands (at 0.8 mm diameter) in a stainless steel jacket of approximately 40 mm diameter, with a small central cooling channel that promotes the flow of liquid helium through the conductor (see figure 1.3 for a representative cross-section of a CIC conductor [12]). This channel, along with a natural void fraction of 25% - 33% that results from stacking and twisting the round wires, maximizes the heat removal rate in the conductor to help maintain electrical stability during magnet operation. This feature is absolutely crucial in a fusion reactor, both because of the heat load from neutrons in the reaction chamber, and also due to the possibility of plasma disturbances and other peak-load conditions unique to a fusion device. Stability is further paramount because of the enormous stored energy in the system, which is 41 GJ [16] in the ITER TF magnet system alone.

In addition to heat removal rate, the CIC design also allows for significant flexibility in the cable architecture specification, very high mechanical strength in the cable (thanks to

the stainless steel jacket), and a very high electric current per turn, providing the large stored energy needed for plasma stability. This flexible, adaptable design will continue to be an important part of magnetic confinement fusion magnet systems, and is also beginning to find applications outside the fusion community. For example, Nb_3Sn CIC conductors have been proposed for the European dipole (EDIPO) test magnet [17, 18] and the series connected hybrid (SCH) magnet [19] at the National High Magnetic Field Laboratory (NHMFL) in Tallahassee, FL.

1.4 Fracture in Nb_3Sn CIC conductors

The significant advantages of the CIC design are tempered by one significant drawback, which is the propensity of brittle superconducting filaments to fracture during magnet operation. In a magnet, electric current produces a force (called the Lorentz Force, or F_L), that can be described as the cross product of the magnetic field vector and the electric current vector. Symbolically,

$$F_L \propto \vec{B} \times \vec{I} \tag{1.1}$$

where B is the magnetic field intensity and I is the electric current. Since this force acts perpendicular to the current direction, it necessarily acts perpendicular to the wire axis as well. Thus, the Lorentz force is constantly attempting to displace the superconducting wire from its neutral position, which can cause filaments of Nb_3Sn (a classic brittle intermetallic) to fracture. To combat this, many magnet systems use an epoxy impregnation technique (combined with a complicated mechanical support structure) to immobilize the strand and

prevent filament fracture. This is a generally effective mechanical stabilization technique that has been used widely in both solenoid [20] and dipole [21] magnet configurations.

The CIC design, however, must necessarily eschew an epoxy matrix, since the principal performance feature of the design is the increased heat transfer achieved by allowing individual superconducting strands to come into intimate contact with liquid helium. Without an immobilizing epoxy matrix, then, individual Nb_3Sn strands in a CIC conductor are allowed to move relative to each other under Lorentz forces, which introduces the possibility of local strain values exceeding the irreversible strain limit (ε_{irr}) for Nb_3Sn. This concern has, in the past, produced significant critical current (J_c) degradation in several important test magnets and cables. In 2001, a degradation of the current-sharing temperature from 7.7 K to 7.2 K (6%) was observed in the ITER Central Solenoid Model Coil (CSMC) [22], a test magnet built to qualify the ITER CS design for operation. ITER responded by raising the J_c specification for the Nb_3Sn strand [23], but the degradation problem has persisted through a variety of cable tests over the subsequent seven years, manifesting itself particularly clearly in cables for ITER [24] and the EFDA dipole [25]. Ameliorating this degradation is absolutely critical to the success of ITER as a fusion project. The electric current sustained in the TF and CS magnet systems determines the maximum magnetic field achievable, which in turn dictates the density, temperature, and burn time of the plasma. The TF magnets, in particular, would require several years and over a half billion dollars to replace, so a sufficiently degraded TF system would likely bring to an end this $12 billion international project.

In the face of these challenges, ITER has been able to largely mitigate the degradation problems through an expensive series of strand and cable tests that probed the extent to which cable architecture (void fraction, twist pitch, twist geometry etc.) variables minimize strand movement and therefore reduce internal damage to the Nb_3Sn filaments themselves. Although conductor qualification is not yet complete, by lengthening the cable twist pitch and reducing the cable void fraction [26], ITER has significantly improved the performance of most TF cables.

What the cable optimization approach does not address, however, is the extent to which the internal wire architecture affects the propensity of filaments to crack. That is, in a cable architecture optimization, the individual strands are treated as a black box, with different strands requiring different cable layouts. Such an approach is problematic on several levels. First, since cable optimization is largely an empirical effort (most existing cable models do not yet have proven predictive power, with one significant exception [27]), direct testing of a full-size cable is required for each redesign. This comes with a price tag of about $300,000 per test [12]. Second, using the cable design as a tool to improve fracture behavior limits the flexibility of the design for other considerations. For example, lengthening the cable twist pitch [28] reduces the ability of the conductor to recover from an electromagnetic perturbation such as a plasma disturbance in a fusion reactor, since the twisted strand helps to cancel the effect of magnetic hysteresis losses. Similarly, reducing the cable void fraction [28] reduces the heat removal rate of the liquid helium by restricting flow. As a final example, changing the twist geometry (from triplets to 6 x 1, for example

[29]) requires redesigning the diameter of the superconducting strand – not a trivial fabrication challenge.

Finally, and most importantly, the cable-design approach to filament protection severely restricts the design flexibility of the strands themselves. Since there is little fundamental understanding of how changes to the filament architecture affect the mechanical toughness of the wire, the strand design is frozen once the cable design is deemed sufficiently optimized. This is problematic for two reasons. First, in large strand procurements such as ITER, manufacturers will be delivering strand for 3 – 5 years, which provides an obvious opportunity for in-house improvement of the strand design. However, if that design is frozen by the procuring agency, these potential improvements cannot be exploited. Second, as procurement managers from the Large Hadron Collider (LHC) can attest [30], significant billet-to-billet microstructural variation can occur even in a very well-understood wire material like NbTi. Without some basis for evaluating the impact of architectural anomalies in a billet, the procurement engineers lack a basis for accepting or rejecting strand from that billet on the grounds of harming fracture toughness.

For each of these reasons, then, it is imperative to understand how the internal strand architecture (the number, size, spacing, and arrangement of the filaments and other strand components) affects the fracture properties of the filaments within the strand. Doing this will not only allow magnet builders to select the most optimized strand, but will also allow them to maximize flexibility in the design of the cable, minimize the number of full-size cable tests required to qualify the conductor, and assess the potential impact of architectural anomalies encountered during strand production.

CHAPTER 2 – BACKGROUND AND CONTEXT

To understand how filament architecture affects the fracture behavior of Nb_3Sn composite strands, we first need to understand what variables determine the strand architecture, what properties a strand manufacturer hopes to optimize by choosing a particular strand design, and how the superconducting community models and tests critical current degradation in Nb_3Sn strands.

2.1 Nb_3Sn structure and mechanical properties

Nb_3Sn is a classic brittle solid, first discovered to be a superconductor in 1954 by Matthias [31]. The material owes its poor mechanical properties to its A15 crystal structure, shown in figure 2.1 [32]. This cubic structure contains a body-centered cubic (BCC) sublattice of Sn atoms, with orthogonal chains of Nb atoms on each face of the cube. Each of the six faces contains 2 x ½ = 1 Nb atom for a total of 6 Nb atoms per unit cell, and the BCC Sn sublattice

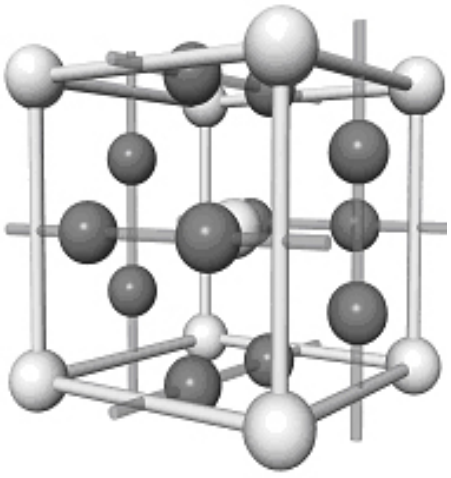

Figure 2.1. The Nb_3Sn (A15) unit cell, adapted from [32]. The lighter atoms are Sn and the darker atoms are Nb. Note that in this crystal structure, the Nb atoms sit in a chain configuration that spaces them more closely than in pure BCC Nb.

contains 8 x 1/8 + 1 = 2 Sn atoms per unit cell. Mechanically, Nb_3Sn has been shown to deform elastically to failure, with plastic deformation possible only at elevated temperatures (above 900°C [33, 34]) via a creep mechanism. Room temperature measurements of the elastic modulus range from 127 GPa [35] to 165 GPa [36], with the cryogenic (4 K) modulus decreasing by 30% (for alloyed Nb_3Sn) [37] to 60% (for binary Nb_3Sn) [38]. This surprise reduction in modulus is believed to be related to the cubic-to-tetragonal phase transformation that occurs around 45 K in Nb_3Sn [39]. A very thorough 2005 review by Mitchell [40] suggests using a value of 100 GPa for Nb_3Sn filaments in practical wires below 35 K. Interestingly, this is actually lower than the 4 K elastic modulus of Cu (137 GPa) [41].

2.2 Chemistry and phase formation

Because of the brittle nature of the A15 phase, Nb_3Sn cannot be directly processed from bulk form to a useable high-current wire. As a consequence, the composite wire must be drawn to final size from ductile (or powder) precursors and subsequently reacted to form the superconducting phase. Unlike the other stable Nb-Sn intermetallics (Nb_6Sn_5 and $NbSn_2$), Nb_3Sn exhibits a significant range of solid solubility, extending from ~18 – 25 at.% Sn, as shown in figure 2.2

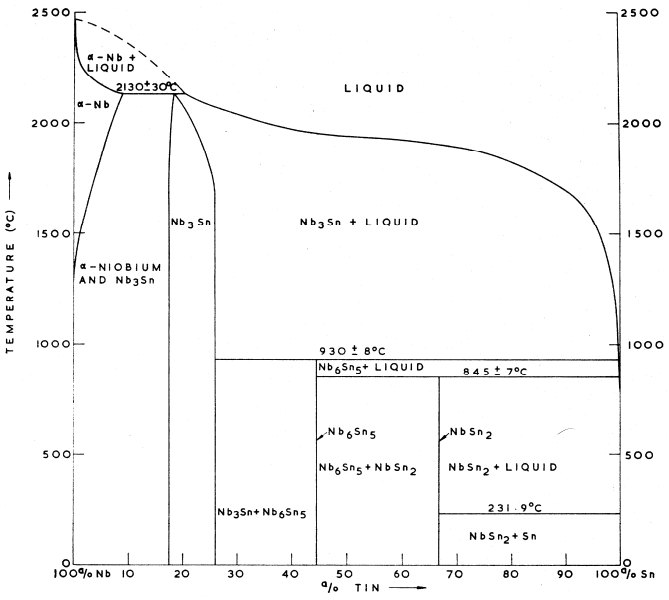

Figure 2.2. The most widely-accepted version of the Nb-Sn binary phase diagram, adapted from [42]. Note the range of solid solubility in Nb_3Sn extending from ~ 18 – 25 at.% Sn.

[42]. Because of the range of solubility, this peritectic phase is often referred to as the "A15" phase, since, from a stoichiometric point of view, the low-Sn crystal structure is much closer to Nb_4Sn than Nb_3Sn. Since the chemical activity of Sn in Nb_3Sn is necessarily fixed (by the Gibbs Phase Rule) at the Nb-A15 interface, a chemical gradient will always be present unless all the Nb can be consumed and the layer reacted to equilibrium. In practice this is impossible to accomplish, since the long, hot heat treatment required for equilibration would grow the Nb_3Sn grains too large to allow the grain boundaries to act as effective magnetic flux pinning sites. However, some minimization of the chemical gradient is desired, since

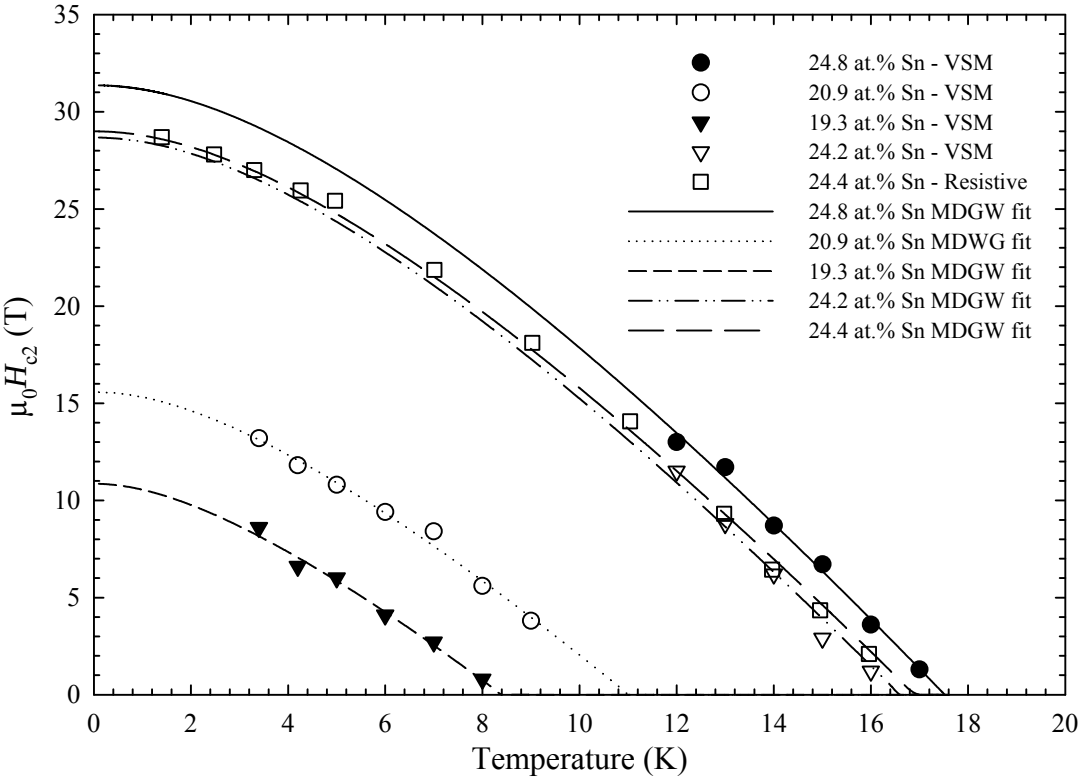

Figure 2.3. The field-temperature superconducting phase boundary for stoichiometric and off-stoichiometric bulk Nb_3Sn, adapted from [43]. A significant focus of Nb_3Sn strand design is driving as much Sn as possible into the A15 layer, in order to maximize the superconducting properties of the material.

high-Sn Nb_3Sn has been shown to have significantly better superconducting properties than low-Sn Nb_3Sn, as shown in figure 2.3 [43]. The wire manufacturer, then, is faced with a delicate kinetic balancing act in trying to form an optimized A15 superconducting layer. Heat treatments too long or too hot will destroy the J_c by lowering the grain boundary density, while heat treatments too short or too cool will suppress J_c by suppressing the primary superconducting properties (H_{c2}, T_c).

2.3 Nb_3Sn wire architectures

To enable formation of a useable wire from a fabrication billet, and to efficiently accomplish the subsequent diffusional heat treatment, wire manufacturers have developed three primary wire architectures. Each is discussed briefly here.

2.3.1 Bronze process

In the bronze process, Nb filaments are embedded in a Cu-Sn bronze matrix (figure 2.4), whose maximum Sn content is ~ 9 at.%. Upon heat treatment, Sn diffuses through the bronze and nucleates Nb_3Sn grains at the Nb-bronze interface. Because of the relatively low activity of Sn in Cu, A15 layer growth is quite slow, and heat treatments of > 200 hours (h) at ~650°C are needed to react through a few microns of Nb. Because of this, the bronze process requires very small filaments (3 – 5 μm diameter), which is not an unreasonable goal thanks to easy co-reduction between bronze and Nb (the result of a close match in mechanical properties). The bronze process was the first Nb_3Sn composite wire technology to achieve long, uniform piece lengths, and remains an important technology for applications requiring small filaments. Filaments in a bronze strand tend to be well-separated, since

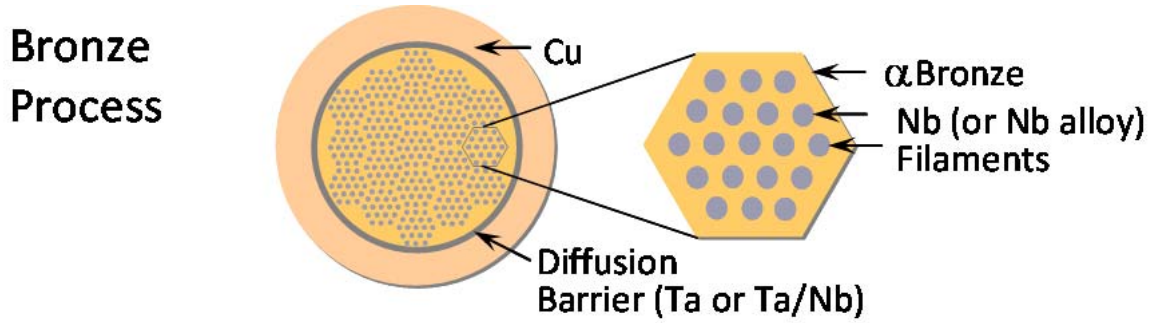

Figure 2.4. Schematic of the bronze process design for Nb_3Sn wire fabrication. Nb filaments are surrounded by a bronze matrix and a single diffusion barrier. Upon heat treatment, the Sn in the bronze diffuses into the Nb and reacts to form Nb_3Sn. Image courtesy Peter J. Lee.

intimate contact with the bronze (and significant diffusion of the Sn within the bronze) is required to form the A15 phase. The J_c in the superconducting layer of a bronze strand, however, tends to be lower than the J_c in other strand architectures [15], since the Sn gradient is steep within the layer [44].

Two examples of applications for bronze strand are (1) rapidly cycled magnets, because the hysteretic losses are proportional to the effective filament diameter, and (2) nuclear magnetic resonance imaging (NMR) magnets, where high field homogeneity and very low persistent-current losses are required.

2.3.2 Internal-Sn

In the internal Sn (IT) process, the wire cross-section is divided into individual sub-bundles, each of which contains an array of Nb filaments embedded in Cu, with a core of pure (or alloyed) Sn. The sub-bundles may be enclosed by a single diffusion barrier (figure 2.5), which is preferred for fusion and other low-hysteretic loss applications, or each sub-bundle may be enclosed by an individual diffusion barrier (figure 2.6), which is preferred for

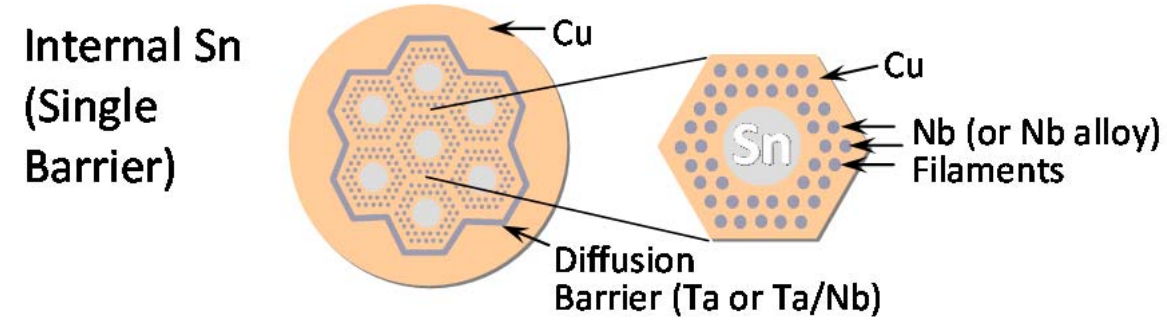

Figure 2.5. Schematic of the single barrier internal tin Nb_3Sn wire design. The single diffusion barrier allows Sn from all sub-bundles to contribute to filament reaction in a homogeneous fashion. This design is usually preferred when the filaments are well-spaced and do not agglomerate significantly upon heat treatment. Image courtesy Peter J. Lee.

high-J_c applications. In this geometry, low-temperature (200°C – 500°C) heat treatment steps are used to mix the Sn from the core with the interfilamentary Cu. A subsequent higher-temperature step (~650°C) is then used to convert the Nb to Nb_3Sn. This process has the advantage of allowing more Sn into the overall package and increasing the Sn activity at the Nb-Cu interface (which increases the reaction rate) but has the disadvantage of being more difficult to uniformly reduce from billet to final size as a result of the large difference in mechanical properties amongst Nb, Cu, and elemental Sn. The IT design also allows the

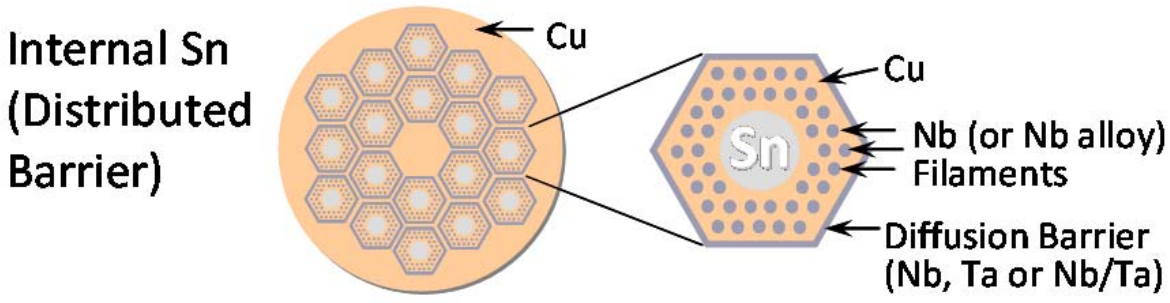

Figure 2.6. Schematic of the distributed-barrier internal tin Nb_3Sn wire design. This design concentrates the Sn in individual sub-bundles, and is usually employed when the most efficient use of volume is required to maximize J_c. Image courtesy Peter J. Lee.

Nb filaments to be spaced more closely than in a bronze strand, since the interfilamentary matrix material (Cu) is not in itself a Sn source. This has the advantage of further increasing J_c by increasing the volume fraction available for conversion to Nb_3Sn, but also can result in filament agglomeration after reaction, due to the fact that the molar volume of Nb_3Sn is 37% larger than the molar volume of Nb.

To improve the matching amongst the mechanical properties of the wire components, many attempts have been made to harden the Sn by alloying. Since, with a melting point of 232°C, Sn is constantly annealing at room temperature, work hardening the material is generally infeasible, and hence reducing the strand to achieve small final filament size remains a significant challenge. However, despite these practical difficulties, IT conductors are currently state-of-the art in terms of J_c [45]. Additionally, it is likely that stable IT reduction processes will ultimately be cheaper than bronze or powder-in-tube (PIT) routes, since they avoid the in-process anneals required for bronze and the expensive powder fabrication of PIT.

2.3.3 Powder-in-Tube

In the powder-in-tube (PIT) process, the inner radius of a Nb annulus is sleeved with a thin Cu tube, and subsequently filled with frangible $NbSn_2$ powder and sometimes elemental Sn and Cu (figure 2.7). This technology suffers from the general problems associated with PIT wire drawing [46], but provides relatively high Sn contents and Sn activities without the large mechanical strength disparity of the internal Sn process. The lower cross-sectional area available for A15 reaction results in 10 – 20% lower J_c values than for IT strands [47], but long piece lengths of high-quality, multifilamentary PIT wire are

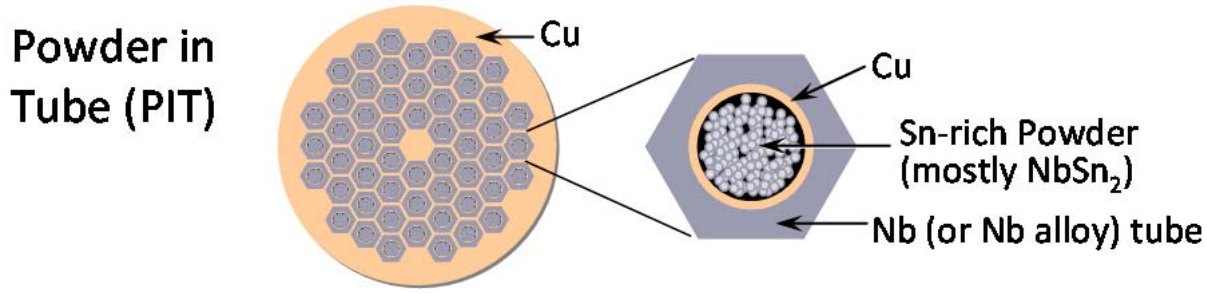

Figure 2.7. Schematic of the powder-in-tube (PIT) Nb_3Sn wire design. Here, a Sn-rich powder is used to react a Nb tube and form the A15 phase. PIT is a tremendously flexible design, since the powder composition can be easily altered. However, the increased cost of Nb tubes and powder fabrication make it difficult for PIT to compete economically with bronze and IT. Image courtesy Peter J. Lee.

now routinely fabricated [48] and incorporated into accelerator R&D programs [49,50]. Very recent optimizations of the PIT heat treatment have resulted in J_c values very close to IT values [51], suggesting that layer J_c values are actually significantly better than in IT, since there is less cross-section available to react in a PIT design.

The primary concern with PIT is the cost of the conductor, mainly attributed to powder fabrication, powder handling, and Nb tube procurement. Because of these concerns, PIT is not likely to be a conductor choice for ITER, and thus has not been included in most of the experimental work presented here.

2.4 Wire selection criteria

Higher critical current density has been the primary goal of the superconducting wire community for the past 20 years. Higher critical current density in the wire affords the magnet builder (1) flexibility in choosing magnet design (2) a smaller profile for the magnet (which reduces materials and cryogenic costs), and (3) a lower price, based on a $/amp-meter normalization. As a result of this singular focus, strand architecture design over the past 15 years has focused almost exclusively on optimizing the strand critical current density for

magnetic fields around 12 T. In the past three years, there has also been development towards strands with a smaller effective filament diameter (d_{eff}), in order to reduce hysteretic losses during magnet cycling. Improving the residual resistivity ratio (*RRR*) of the stabilization Cu has also become a point of emphasis, as dynamic stabilization of electromagnetic perturbations has become important [52].

These design parameters highlight the inherent compromises involved in Nb_3Sn strand design. Consider the following examples. To increase J_c, strand manufacturers would like to allocate as much of the cross-section as possible to Nb and Sn (or Sn-bearing) components. But because the A15 phase formation is limited to diffusional techniques, and because a fine (< 200 nm) Nb_3Sn grain size is desired, some diffusion pathways must exist in the system. Thus, in IT designs, for example, some interfilamentary Cu is required, reducing the areal fraction available for conversion to Nb_3Sn, and thus limiting J_c. Similarly, to increase J_c the strand manufacturer would like to convert as much of the Nb as possible to Nb_3Sn. But the extended reaction required to achieve this has been shown to cause Sn to migrate through the diffusion barrier and into the stabilization Cu, where it dramatically lowers the *RRR* [53]. As a final example, to reduce hysteretic losses, a small filament size is desirable. But the co-reduction of mechanically mismatched pre-reaction constituents like Cu, Nb, and Sn (required since Nb_3Sn is brittle!) limits the fabricability of the composite.

Considering these already-complicated optimization parameters, it is no surprise that other strand considerations (such as fracture toughness) have received very little attention from the wire manufacturers. The primary applications for Nb_3Sn strand have been accelerator (dipole, quadrupole) and solenoid magnet systems, where fully-impregnated coils

leave little room for the conductor to move during magnet operation. This, combined with the lack of a quantitative test for fracture toughness in the composite, has been responsible for this lack of focus.

In summary, the brittle nature of the A15 Nb_3Sn phase constrains the strand design and imposes limits on the strand parameters of interest to magnet designers. The optimization efforts of wire manufacturers have very rightly been focused on parameters such as J_c, *RRR*, and d_{eff}, and in fact extraordinary progress has been made over the last decade to improve all three of these parameters. In a sense, then, the brittleness problem has been ameliorated by a combination of clever strand architecture and clever thermomechanical treatment. However, this has come at the expense of the strand design being largely dictated by fabrication and heat treatment concerns.

2.5 Reversible and irreversible strain

In a Nb_3Sn composite strand, strain is produced from Lorentz forces (during magnet operation), thermal stresses due to differential thermal contraction of the interfilamentary Cu with the Nb_3Sn [54], and stresses induced in the individual filaments during heat treatment. Since strain (by definition) distorts the atomic lattice of the superconducting material, all strain will influence the superconducting properties of the material. In some high-T_c superconductors, this effect can be positive. However, for most low-T_c superconductors, the effect of strain is uniformly negative [55]. This was first observed in Nb_3Sn in 1963 by Müller and Saur [56], but a plausible scaling relationship for the phenomenon was not developed until the 1980s with the work of Ekin [57, 58], who developed a power-law fit for the degradation of critical current and upper critical field as a function of uniaxial strain. The

Ekin model fits a simple, though asymmetric, power law function to J_c data as it deviates from zero strain in either the compressive or the tensile direction.

This work was advanced by ten Haken [59] and Godeke [60], who considered the effect on J_c of the deviatoric component of the strain, which is particularly important for high energy physics accelerator magnets that experience significant transverse compressive stress. Other significant efforts to model J_c degradation include the work of Hampshire [61], who has developed a very precise, though empirical, polynomial fit to scale J_c data with strain, and the work of Summers [62]. More recently, Markiewicz [63] has developed a more fundamental model of strain dependence that takes into account the change in phonon frequency distribution resulting from an arbitrary strain imposed on the Nb_3Sn lattice.

The significant point here, however, is that none of these sophisticated models draw a distinction between reversible strain (caused by elastic deformation to the Nb_3Sn lattice) and irreversible strain (caused by filament fracture or permanent changes to the strain state in the matrix surrounding the Nb_3Sn filaments). While these models are still valid over a wide strain domain (including the compressive strain domain relevant to many accelerator dipole and quadrupole magnets), the failure to include fracture in the tensile domain limits the extent to which these models can move beyond phenomenology. There is very little data available in the literature to make this connection. In short, the effect of fracture on critical current degradation is very poorly understood.

Additionally, direct observation of the number, size, and distribution of fracture events in Nb_3Sn composite wire has received surprisingly little attention by the superconducting community. Zhang, Ochiai, and Osamura [64] evaluated fracture using

metallography in bronze-processed wires in 1989. Their uniaxial strain test (conducted at room temperature) concluded that lower Nb_3Sn fractions in the composite actually increased fracture due to the matrix more effectively transferring load to the filaments. Van Oort [65] also examined fracture behavior after cabling by metallography and noticed that fracture incidents seemed to be correlated with microstructural features such as Kirkendall voids. Lee [66] has detected fracture events in Nb_3Sn tape conductor using an acoustic emission (AE) technique. While AE is attractive because it is non-destructive, the spatial resolution of the technique is not sufficient to image cracks in the 3 – 5 μm filaments of modern Nb_3Sn strand.

At the cable level, there are several very advanced models that predict the current-carrying capability of the CIC conductor as a function of field, temperature, and strain [25, 26, 67]. Of these, only one [25] incorporates filament fracture, and even then only as a homogenized quantity within the strand.

On both an experimental and a computational level, then, the significant resources being dedicated to optimizing Nb_3Sn CIC conductors ignore the very mechanism that causes irreversible degradation – the fracture of the brittle Nb_3Sn filaments. In this work, we will attempt to elucidate some of the underlying mechanisms that cause crack initiation and propagation in these composite strands, and also quantify the density and distribution of cracks under a variety of loading conditions. Such information should guide manufacturers towards designing more strain-tolerant strand, provide interpretation for the experimental cable testing, and inform strand and cable modeling efforts.

Chapter 3 will discuss the development of a metallographic technique to image cracks in these delicate composite strands. Chapter 4 presents the quantitative metallography of the

strands under examination, and chapters 5 – 7 will present results of various fracture tests that have been carried out on candidate ITER and HEP strands. The implications of these results for future strand design are presented in chapter 8.

2.6 Nomenclature

The nomenclature used to describe the various components of a Nb_3Sn composite wire can be confusing and sometimes contradictory. Throughout this thesis, we will attempt to use the following definitions:

1. **Cable** – This is the primary current-carrying unit in a magnet. It can contain anywhere from less than 20 (in a small Rutherford-type cable) to over 1000 (in a large CIC conductor) superconducting strands.
2. **Strand** – This is the entire Nb_3Sn wire, usually less than 1 mm in diameter. It contains Nb_3Sn filaments, one or more diffusion barriers (usually Nb or Ta), and stabilization Cu.
3. **Bundle** – This is the set of all Nb_3Sn filaments in the strand. The filaments can be all contained within a single diffusion barrier, or segregated by multiple diffusion barriers.
4. **Sub-bundle** – Almost all bronze and internal tin strands stack the Nb filaments into smaller groupings within the bundle, often called sub-bundles. These sub-bundles can range in filament count from a few tens of filaments to many hundreds of filaments, depending on the strand architecture. This sub-bundle is normally the principal unit drawn to fine size before restacking to make the final billet.

5. **Filament** – This is the individual Nb_3Sn fiber that carries electric current. Filaments usually range in diameter from 3 – 6 μm, and in internal tin designs, filaments may grow together, with agglomerated units as small as two filaments or as large as the entire sub-bundle. This agglomeration increases the effective filament diameter (d_{eff}) for both electrical and mechanical properties, relative to individual filament size.

Each of these features is shown in figure 2.8.

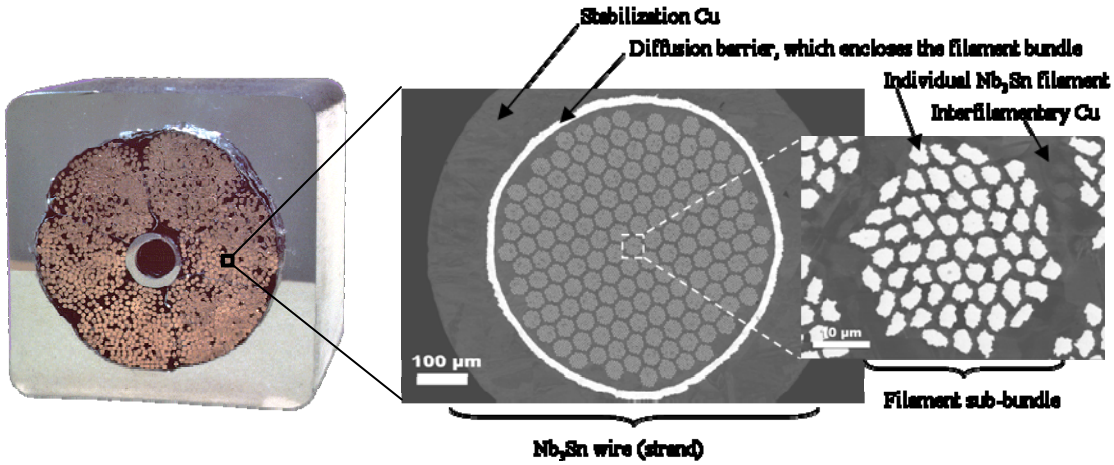

Figure 2.8. Composite image of a superconducting cable (left panel, image courtesy Peter J. Lee), Nb_3Sn strand (center panel), and filament sub-bundle (right panel) with individual filaments surrounded by interfilamentary Cu. With ~1000 strands/cable, and ~10,000 filaments/strand, a 40,000 A superconducting cable can easily contain over 10^7 individual filaments throughout which the electrical load is distributed.

CHAPTER 3 – METALLOGRAPHIC PREPARATION TECHNIQUES

3.1 Transverse sample preparation

A metallographic examination of the filament structure in a Nb_3Sn strand can be conducted on the transverse or the longitudinal cross-section of the sample. The transverse cross-section (shown schematically as region **a** in figure 3.1) is perpendicular to the wire axis, and the longitudinal cross-section (region **b** in figure 3.1) is parallel to the wire axis, which is indicated by the arrow in figure 3.1. This nomenclature can become confusing in the context of identifying cracked filaments, since transverse cracks will appear in the longitudinal cross-section, and longitudinal cracks will appear in the transverse cross-section. Because the filaments themselves run parallel to the wire axis, it is almost impossible to locate and identify a transverse crack from a transverse cross-section, since the sampled area will be parallel to the crack direction. Thus, some care is required to design an experiment that will sample the desired data. For current density considerations, the transverse cracks are almost certainly the primary degradation artifacts, since these cracks physically obstruct the axial flow of electric current along the filament. As

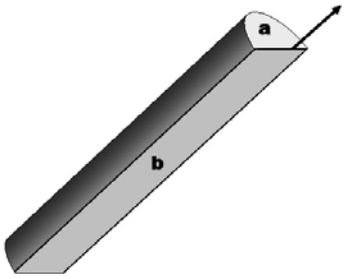

Figure 3.1. Schematic of a round wire that has been sectioned transversely (region a) and longitudinally (region b). The arrow indicates the direction of the wire axis.

a result, longitudinal cross-sections will be the primary orientation used to identify degraded filaments.

However, the transverse cross-section does contain some important information. Because these strands are multifilamentary and twisted (the twist pitch is usually between 10 – 20 mm), obtaining accurate strand geometric information (such as filament number, size, and spacing) and extent of reaction from the longitudinal cross-section can be very difficult.

To ensure that a truly transverse cross-section is mounted, the usual procedure is to first cure an empty, 1 inch (25.4 mm) metallographic puck made from conductive phenolic resin (such as Buehler Konductomet or similar), and then drill a hole just large enough to fit one (or more) of each strand being investigated, and then re-cure the puck with a small amount of additional resin. With a properly sized drill hole and samples at least 5 mm long, a very close approximation to a true transverse cross-section can be obtained.

One common polishing simplification, given sufficient quantity of strand, is to mount three identical wires in the same drill hole, thus decreasing the chance that a single rogue scratch from the polishing procedure will interfere with sample imaging. The theoretical radius of a drill hole to exactly circumscribe three cylindrical strands in a close-packed arrangement can be obtained as follows:

$$R_H = r_w\left(1+\sqrt{3}-\frac{1}{\sqrt{3}}\right) \cong 2.155 * r_w \qquad (3.1)$$

where R_H is the radius of the drill hole and r_w is the radius of the wires being circumscribed.

Polishing of a transverse cross-section of Nb_3Sn strand is relatively straightforward, although some care should be exercised to avoid undercutting in the final polishing steps,

since the composite contains very soft Cu and very hard Nb_3Sn in an intimate mechanical mixture. If applicable to the analysis, smearing of the Cu should also be closely monitored to avoid obscuring the Kirkendall voids that develop during heat treatment. A typical procedure might involve coarse grinding sequentially at 240, 320, 400, 600, and 800 grit, using SiC abrasive paper. Note that abrasive particle sizes in this thesis will either be reported in microns or in U.S. grit sizes, which is a convention defined by the mesh of a screen through which particles are sifted prior to being applied to the backing paper. Note also that U.S. grit sizes differ from European grit sizes, as shown in Table 3.1 (adapted from [68]).

Table 3.1
European and U.S. grit sizes

FEPA (Europe)		**ANSI/CAMI (USA)**	
Grit number	**Size (μm)**	**Grit number**	**Size (μm)**
P60	269.0	60	268.0
P80	201.0	80	188.0
P100	162.0	100	148.0
P120	127.0	120	116.0
P180	78.0	180	78.0
P240	58.5	220	66.0
P280	52.2	240	51.8
P320	46.2		
P360	40.5	280	42.3
P400	35.0	320	34.3
P500	30.2	360	27.3
P600	25.8		
P800	21.8	400	22.1
P1000	18.3	500	18.2
P1200	15.3	600	14.5
P1500	12.6	800	12.2
P2000	10.3	1000	9.2
P2500	8.4	1200	6.5

The coarse grinding steps through 600 grit are intended to remove the damaged layer introduced by sectioning the sample with wire cutters (more detail on the effects of sectioning technique in section 3.2, below) and to flatten the sample prior to fine polishing. As such, these coarse grit steps can be performed on a manual or semi-automatic polishing wheel, with water lubrication, a wheel speed of ~200 revolutions per minute (RPM), and a grinding time of 2 – 4 minutes per step. The SiC abrasive papers are semi-fixed abrasives, which means the abrasive is released from the backing paper during polishing, allowing the SiC particles to grind by rolling between the paper and the sample. This causes the papers to suffer a significant decrease in sample material removal rate after 1 – 2 minutes of continuous grinding, so a new abrasive paper is suggested beyond this time interval. Hand force (manual wheel) should be light to moderate to avoid sample beveling, while the machine force (semi-automatic wheel) is recommended in the range of 3 – 5 pounds (13 – 22 newtons). These initial steps should remove 0.5 mm – 1.0 mm of sample depth, which can be checked with a precision calipers or micrometer if an initial measurement after mounting but before polishing was obtained. If polishing by hand, rotating the sample 90 degrees between steps is recommended to verify that the scratches from the previous step have been completely removed. With experience, some of these initial steps can be combined or removed without sacrificing the final quality of the polished surface.

At and beyond 800 grit, use of a semi-automatic polisher is no longer recommended, since the particle sizes are sufficiently small that the backing paper on the abrasive disc can easily become an abrasive itself and destroy the quality of the sample surface. At 800 grit, a SiC abrasive paper is still recommended, though with very light manual force and a

somewhat extended polishing time (5 – 6 minutes). Beyond 800 grit, two additional polishing steps are usually required before the sample is ready for final polishing at 0.05 μm. These intermediate steps usually involve diamond paste or other fixed abrasives (at 6 μm and 1μm, for example) on a low-nap cloth such as the Buehler TexMet 1500 pad with a water-based lubricant, slow (50 RPM) wheel speed, and a counter-rotating manual polishing technique. Polishing times at each step can range from 5 to 15 minutes, depending on the quality of the sample after coarse grinding. At these intermediate steps, the trade-off between polishing quality and polishing efficiency is most pronounced. A faster polish can be obtained by using a more aggressive cloth (longer nap), faster wheel speeds, and higher sample pressure. However, all these modifications will also increase the difference between the Cu and Nb_3Sn polishing rates, leading to significant undercutting of the soft Cu and possible subsequent damage to the filament pack.

After intermediate polishing to 1 μm, final polishing is recommended at 0.05 μm, using colloidal silica (or similar abrasive) on either a medium nap cloth or a napless synthetic "sponge" cloth such as the Buehler Chemomet pad. Other polishing parameters (wheel speed, technique, time) should be similar to the intermediate polishing steps. In addition to the manual final polish, vibrational polishing was shown to be very effective at removing damage caused by previous polishing steps. This technique will be described in much greater detail in section 3.2 below, but as it relates to transverse polishing, figure 3.2 (next page) shows the progression of a common sub-bundle as it progresses from (a) manual polishing only, to (b) manual polishing + 3 hr vibrational polishing, to (c) manual polishing + 7 hr vibrational polishing. Vibrational polishing reduces the instances of fractured filaments

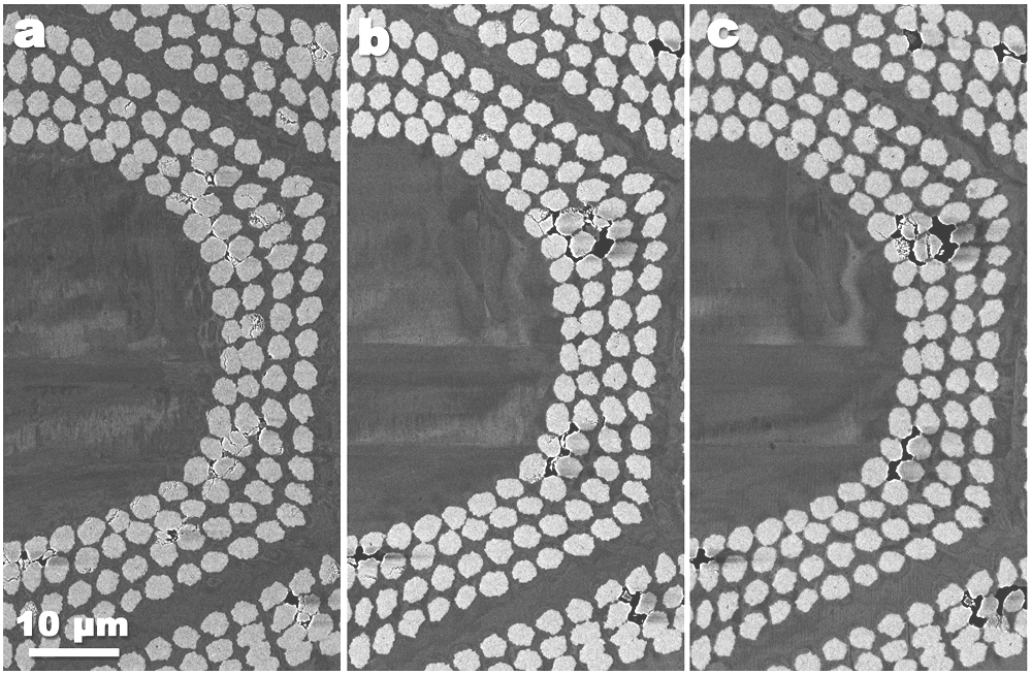

Figure 3.2. Progression of a transverse cross-section polished manually plus vibrational polishing for (a) 0 hr, (b) 3 hr, and (c) 7 hr. As indicated by the circled areas of interest, the vibrational technique tends to remove surface cracks and also reveal the interfilamentary void structure by removing debris and smeared Cu. In one instance in panel (c), two new cracks are seen that were not present previously. Because the vibrational polisher is such a gentle technique, it is likely that these were pre-existing cracks just under the surface of the original polished cross-section.

and also clears smeared Cu and polishing debris from the interfilamentary voids in the sample. A clean, well-polished transverse cross-section of a Nb_3Sn strand is shown in figure 3.3. Note, in this image, the clearly delineated interfilamentary Kirkendall voids (located at a characteristic radial position within the sub-bundle) that evolved during heat treatment. Typically, these voids are obscured after manual polishing. If these voids

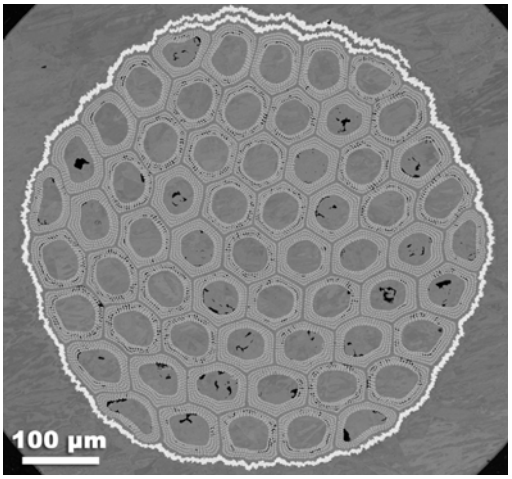

Figure 3.3. Cleanly polished transverse cross-section of a Nb_3Sn composite wire. Notice the large, clean voids in the sub-bundle cores, and the smaller interfilamentary voids that are also clearly visible.

are known to exist in the sample being prepared, they can serve as an excellent guide to the condition of the final polish.

3.2 Longitudinal sample preparation

Compared to the transverse cross-section, metallographic preparation of longitudinal cross-sections is significantly more challenging. Surprisingly, there is relatively little information in the metal-matrix composites (MMC) literature describing techniques for metallographic preparation of composites with brittle continuous fibers, although the thesis of Shahini [69] has several useful tips for Al-based composites. For most MMC applications, the material is tested to failure, so the fracture surface can be directly observed after complete composite failure. Since we are interested in the fracture behavior in the first 1% strain, a more sensitive longitudinal polishing technique is required. The primary challenges associated with this technique can be summarized as follows:

1. Because a long (1 – 2 cm) section of wire is being prepared, the tolerance for sample flatness and parallel top-and-bottom faces of the puck is significantly more strict. Based on the targeted polishing depth specified in point #2 below, less than 100 μm of sample height variation can be tolerated across the surface of the metallographic puck. On a puck of 1 inch (25.4 mm) diameter, this translates to an acceptable grade of less than 0.4%.
2. Because most Nb_3Sn strands are less than 1 mm in diameter, of which almost half is stabilization Cu, there is a strict tolerance on the grinding depth to be achieved during polishing. The samples used in this study are 0.8 mm in diameter, so a polishing depth of 400 μm ± 50 μm was targeted for each metallographic puck. The

importance of achieving a proper polishing depth is further amplified by the fact that since the wires are cylindrical in nature, the metallographic puck does a poor job of holding the sample once > 50% of the diameter has been polished. For the 0.8 mm diameter wires examined here, it was observed that polishing more than 50 μm beyond the half-way point of the wire introduced a significant possibility for sample pull-out in the puck.

3. Because the transverse cracks revealed in the longitudinal cross-section are the primary current-blocking feature being investigated, it is essential that polishing-induced cracking be minimized. In a transverse cross-section, where the primary analysis objectives are filament size, shape, distribution, and spacing, a distribution of polishing-related cracks can be tolerated without compromising the measurement. In a longitudinal cross-section, however, polishing-related cracks are a direct obfuscation of the variable under study, so some special care is required to verify that the fracture events seen in the polished sample are indeed from the mechanical test and not from the polishing.
4. The concern raised in point #3 above is exacerbated by the fact that, in longitudinal cross-section, the filaments are significantly more exposed to the abrasive polishing media than in transverse cross-section, and therefore more susceptible to damage. That is, a common polishing procedure will leave behind more polishing-related damage in a longitudinal cross-section than a transverse cross-section. One significant effort in this thesis, therefore, was to develop a longitudinal polishing

procedure that could reliably generate specimen surfaces free from polishing-related cracking.

To understand the requirements for longitudinal polishing, it is worthwhile to review briefly the principles behind metallographic grinding and polishing. The generic technique is to use a series of progressively finer abrasive particles to (1) flatten the sample and grind through any damage layer from sectioning or, in our case, the stabilization Cu around the filament bundle, and then (2) progressively remove the damage introduced at the previous step by means of finer abrasive particles. One rule of thumb used by metallographers to help estimate the damage induced by an abrasive is to multiply the abrasive particle size by two to arrive at the damage depth. So, 15 μm abrasive particles (approximately 600 grit) will produce a damage layer of ~30 μm in depth.

Relying solely on visual inspection (even with an optical microscope) between polishing steps can result in underestimating the removal of this damage layer, particularly in composite materials with a soft component like Cu, since the soft material can smear and obscure the damage from the previous steps. Hence, for an application like longitudinal polishing where proper material removal is essential, some direct method of specifying the amount of material removed is advisable. This can be as simple as measuring the puck thickness at 2 – 4 locations around the puck circumference with a micrometer after each step. A complementary method, which is particularly useful for achieving

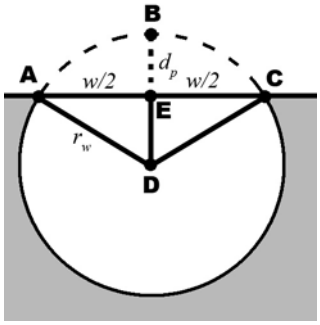

Figure 3.4. Schematic representation of the relationship between observed width (w) and polished depth (d_p). Note the gray area represents the metallographic puck in which the sample is encased.

the proper polishing depth in the sample, is to use the visible width of the sample (w) to calculate the polishing depth (d_p), based on the circular cross-section of the cylindrical wire. As sketched in figure 3.4, this can be accomplished with a simple trigonometric treatment, which yields:

$$d_p = r_w - \sqrt{r_w^2 - \frac{1}{4}w^2} \tag{3.2}$$

where r_w is the radius of the wire.

This approach does have one downside, which is that the visible width, w, becomes insensitive to changes in d_p near the full diameter. However, as shown in figure 3.5, the

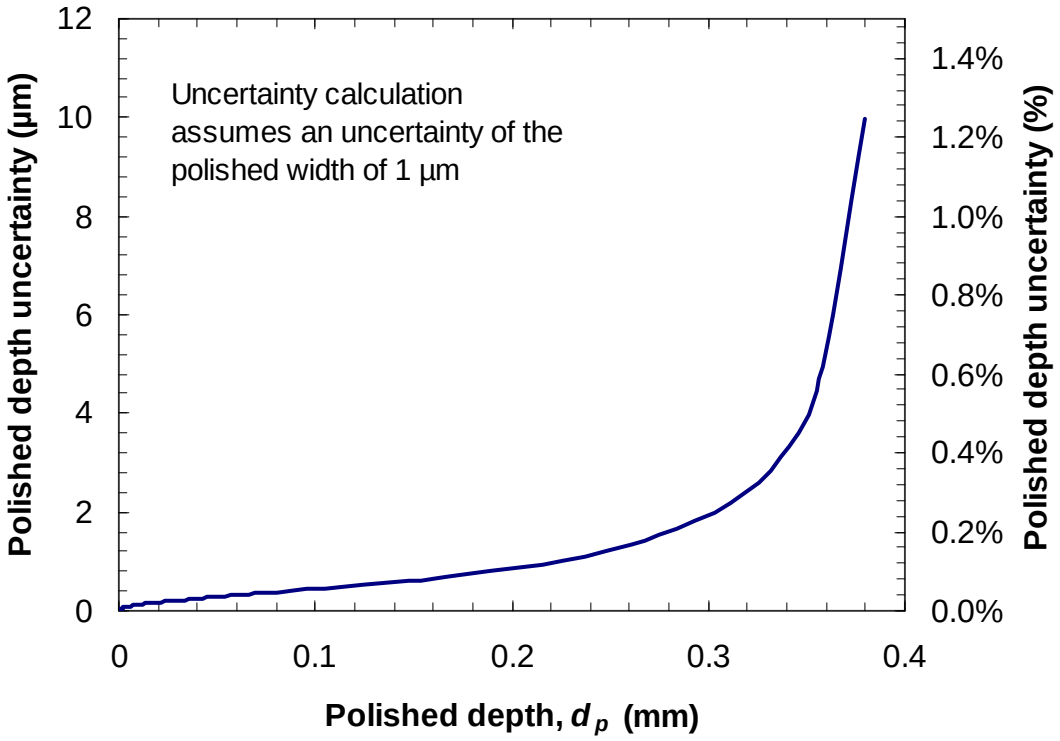

Figure 3.5. Uncertainty estimate for calculation of polished depth (dp) by measuring exposed polished width. This analysis assumes a wire of 0.8 mm diameter and a width measurement uncertainty of 1 µm. This technique of estimating polishing depth is superior to puck thickness measurements until the polished section approaches the center of the wire.

sensitivity is still better than direct micrometer measurement (for an uncertainty of 1 μm in an image acquired on a light microscope) for polishing depths up to ~0.35mm (for our 0.4 mm radius wires). This uncertainty is calculated by differentiating the half-circle function that describes the circumference of the wire, and multiplying the derivative by the uncertainty in the sample width measurement.

Achieving a high-quality polish on a longitudinal cross-section requires a careful optimization between polishing rate and polishing damage induced. An aggressive polish (higher pressures, higher wheel speeds, and larger grits) will more quickly remove the damage from the previous polishing step, but will introduce a larger damage layer of its own. A more gentle polish (lower pressures, lower wheel speeds, and finer grits) will introduce less damage, but will also remove the previous damage layer at a significantly reduced rate. Some general principles that should guide the design of a polishing procedure for composites with brittle filaments such as Nb_3Sn are provided here. While these guidelines were developed within the experimental context of this thesis, they are in good agreement with suggestions provided in metallography handbooks, such as that of Vander Voort [70].

1. Fixed abrasives should be used when possible. Rolling and semi-fixed abrasives have the tendency to introduce chips and cracks at interfaces between brittle and ductile components, which provide ideal nucleation sites for transverse filament cracks that are subsequently very difficult to distinguish from existing cracks.
2. Semi-automatic polishing is recommended for the first step only. As will be described below, some intermediate steps of the longitudinal polishing sequence require significant polishing times, making use of a semi-automatic polishing

machine seemingly attractive. However, in our experience, the automated polishing machines do not, in general, have the sensitivity to perform the very delicate polishing routines necessary for suitable longitudinal polishing. Thus, in this procedure, we restrict use of a semi-automatic polishing machine to the first (flattening) step only.

3. Nap-free cloths are recommended for the intermediate and final polishing steps. Cloths with a significant nap, while in general producing faster polishing times, are also sufficiently aggressive that there is an increased risk of the sample "catching" on the pad and damaging the exposed filament structure. This risk can be largely mitigated by using a nap-free cloth, since the flat surface is easier to lubricate in a controlled fashion. However, this can increase polishing time by decreasing material removal rate.

With these general principles in mind, then, an acceptable procedure for polishing longitudinal Nb_3Sn samples was implemented. First, the sample was ground on 600 grit SiC paper using a semi-automatic polisher. Although the semi-automatic polisher will introduce more damage than a similar manual technique, use of the automated polisher is recommended to ensure that the sample is polished flat (to a high tolerance) and to a desired depth. A wheel speed of 200 RPM is suggested, with new SiC paper added every two minutes until the desired depth is achieved.

The second polishing step is critical, since it bridges the high-removal, high-damage coarse grinding steps to the low-removal, low-damage fine polishing steps. At this step, the large (15 – 30 μm) damage layer from the semi-automatic polishing machine must be

removed with an abrasive aggressive enough to accomplish this within a reasonable time frame, but gentle enough to not introduce a large damage layer of its own. For this work, an 8 μm fixed-diamond pad (such as the Buehler Apex DGD pad) was used, with manual polishing and a 160 RPM wheel speed (water lubrication). This step typically requires 30 to 60 minutes of polishing time.

After polishing at 8 μm, the recommended polishing procedure differs based on whether manual polishing or vibrational polishing will be used for the final polish. Each is discussed below.

3.2.1 Manual final polishing

At grit sizes below 6 – 8 μm, high-removal rate polishing cloths (like the fixed diamond pad used at 8 μm) are typically not available. Thus, paste or slurry abrasives are required. While these abrasives are in general very gentle and introduce very little damage on the sample surface, they also remove material at a much slower rate than the fixed diamond abrasives. With that caveat in mind, the recommended manual final polishing procedure for longitudinal samples is as follows:

1. 60 – 120 minutes at 3 μm, using diamond paste on a napless cloth with water-based lubricant. A wheel speed of 50 RPM is suggested, with counter-rotation of the sample on the wheel and light pressure.
2. 60 – 120 minutes at 1 μm, using diamond paste on a napless cloth with water-based lubricant. A wheel speed of 50 RPM is suggested, with counter-rotation of the sample on the wheel and light pressure.

3. 60 – 120 minutes at 0.05 μm, using colloidal silica on a napless chemo-textile final polishing cloth. A wheel speed of 50 RPM is suggested, with counter-rotation of the sample on the wheel and light pressure.

This procedure, when applied with care, can produce repeatable polished surfaces that are free from polishing-induced cracks. Unfortunately, it is also extraordinarily time consuming, and not, in general, amenable to adaptation with semi-automatic polishers, due to the very fragile nature of the Nb_3Sn filaments. Even when low pressure is used on an automatic polisher, the initial contact force between the sample and the polishing wheel was observed to be too high, thereby introducing damage. This was true for the semi-automatic polisher available for this work (a Buehler Ecomet 3 base with an Automet 2 head), though further progress might be made with automatic polishers that specialize in low force procedures, such as the Allied MultiPrep system. However, the need for semi-automatic polishing at these final steps was largely mitigated by the introduction of vibrational polishing, discussed below.

3.2.2 Vibrational final polishing

Vibrational polishing was introduced in the 1950s by Krill [71] and Long and Gray [72], and an excellent review of the initial vibratory polisher designs is provided by Rothstein [73]. In a vibrational polisher, a low amplitude, high-frequency oscillation is applied to the polishing bowl, which contains a polishing cloth and an abrasive slurry. This oscillation causes the sample (mounted face-down in a sample holder) to revolve within the bowl in an azimuthal fashion, which in turn gently polishes the sample surface.

Early vibrational polisher designs incorporated an oscillation that contained both a horizontal and a vertical component, which was an effort to increase the polishing rate of the system. This had the effect, however, of polishing soft components much faster than hard components (creating relief), and easily introducing polishing artifacts such as swirls and striations. For these reasons, the technique never achieved wide adoption. A second generation of vibrational polishers has been developed, however, that carefully limits the vertical component of the vibration [74] and maximizes the horizontal component. While slowing the material removal rate, this has the effect of polishing even composite materials with a high degree of flatness, and very long polishing times (24 – 28 hrs) can be employed without introducing significant polishing artifacts. In addition to being a very gentle technique, vibrational polishing is also an automated technique, making it an ideal solution for the final polishing requirements of composite Nb_3Sn conductors.

The vibrational polisher used in this procedure is a Buehler Vibromet 2, which operates at a frequency of 7200 Hz, with a variable amplitude drive. The polishing bowl is 12 inches in diameter. Using a vibrational polisher significantly simplifies and automates the final polishing steps required to produce a clean, flat, artifact-free sample in a repeatable manner. A suggested procedure follows:

1. After the 8 μm step, a 3 μm step is recommended, using diamond paste on a napless cloth with water-based lubricant. A wheel speed of 50 RPM is suggested, with counter-rotation of the sample on the wheel and light pressure. 15 – 20 minutes is usually sufficient to remove a significant fraction of the damage from 8 μm and flatten the surface for efficient vibrational polishing.

2. Vibrational polishing is performed immediately after the 3 μm step. A low-nap final polishing cloth (such as a Buehler Mastertex cloth) is used along with 0.05 μm colloidal silica, at 50% - 60% of maximum vibrational amplitude. For a longitudinal cross-section, 36 – 48 hrs of vibrational polishing are required to completely remove the polishing damage.

With this procedure, clean, flat, damage-free longitudinal cross-sections of Nb_3Sn composite wires can be prepared, with a time investment of about two hours + automatic vibrational polishing. The progressive removal of filament damage can be seen in figure 3.6, which contrasts the damage present after the polishing steps indicated in the figure caption.

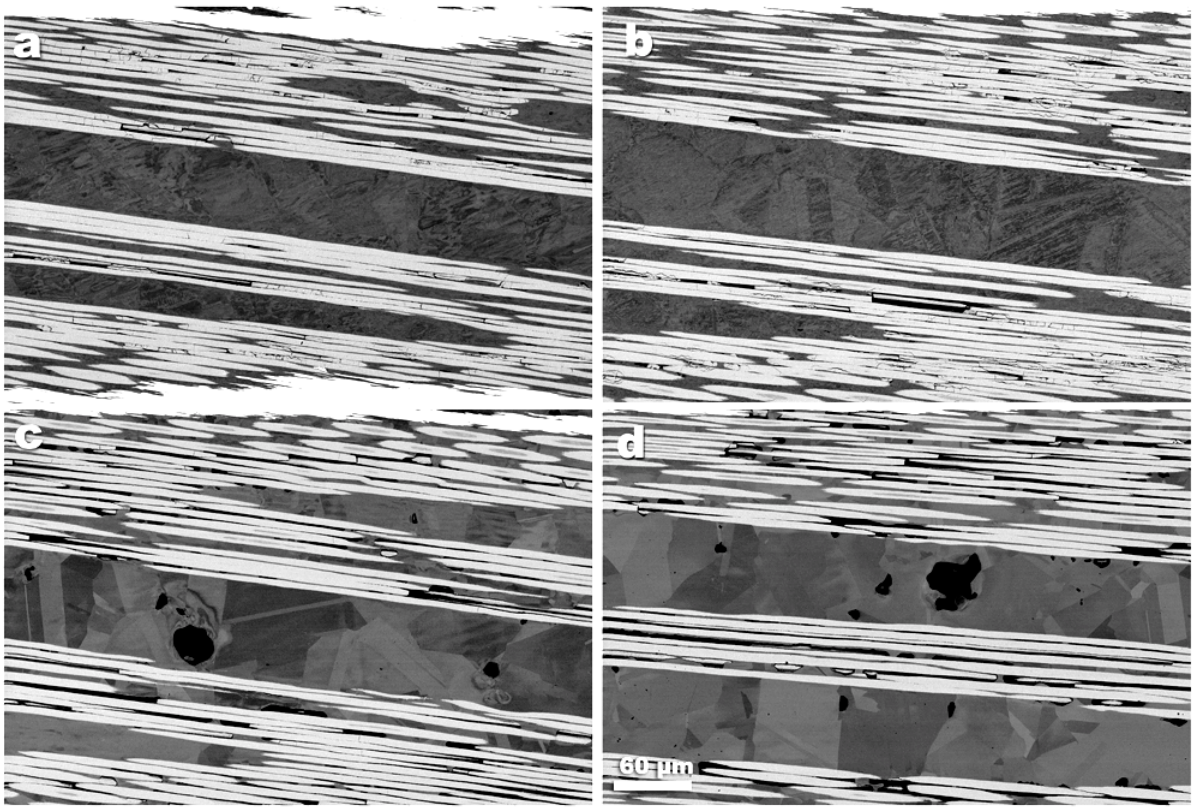

Figure 3.6. Longitudinal cross-section of Nb_3Sn strand after (a) 15 μm grit + 1 hr vibrational polish (to clean and flatten surface), (b) 8 μm grit + 4 hr vibrational polish, (c) 8 μm grit + 18 hr vibrational polish, and (d) 8 μm grit + 38 hr vibrational polish.

As seen in panel (a), the 15 μm grit leaves filaments significantly warped and fractured, with debris cluttering the voids. After 8 μm grit (panel b), there is less warping of the filament pack, but the crack density remains similar to that after 15 μm. After 18 hr of vibrational polishing (panel c), the Kirkendall voids are clear and free from polishing debris. However, it is only after 38 hr (panel d) that the filament pack is free from cracks.

3.2.3 Identification of polishing damage

Even with a highly repeatable vibrational polishing technique, it is important to evaluate the condition of each sample prior to imaging. This was accomplished in three ways. First, witness samples (Nb_3Sn strands that had not undergone mechanical testing) were polished along with the test samples in each puck. A clean, unbroken filament pack in the witness sample is strong evidence of a suitable polishing sequence. Second, certain samples have highly localized fracture fields (like the bend samples discussed in chapter 5 or the TARSIS samples discussed in chapter 6). In these samples, the quality of the filament pack far away from the region of expected fracture localization is an indicator of polish quality. Third, certain characteristic damage patterns can be observed that are clear indicators of polishing damage. Figure 3.7 shows two such examples. In panel (a), two rogue scratches are identified in a bronze-route Nb_3Sn strand by the line of clearly correlated cracks left in their wake. In panel (b), a damaged internal tin conductor is shown. This strand exhibits several classic signs of polishing damage, including (1) Nb_3Sn debris in the post-heat treatment Kirkendall voids, (2) longitudinal fracture events in the Nb_3Sn bulk, and (3) localization of those longitudinal cracks near sub-bundle Kirkendall voids. Internal tin wires with agglomerated filament packs are ideal witness strands, since the agglomerated filaments

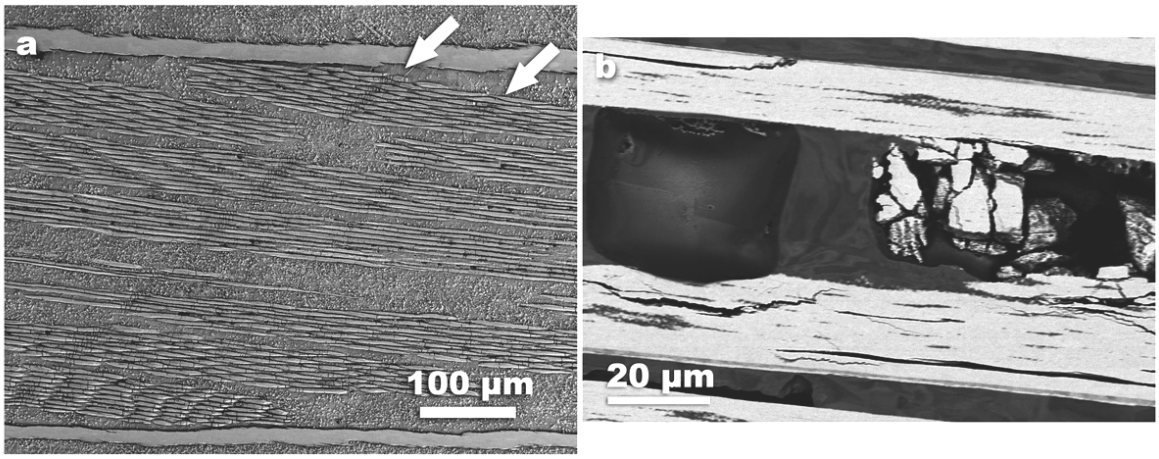

Figure 3.7. Scanning electron microscope images of two Nb_3Sn strands in longitudinal cross-section, with a characteristic polishing damage pattern in each. In panel (a) a rogue scratch, presumably due to the introduction of contamination on the polishing wheel at an earlier polishing step, has left behind two parallel lines of filament cracks, as indicated by the arrows. In panel (b), a sub-bundle from an internal tin strand is shown. Here, the polishing damage is evidenced by both the large amount of filament debris remaining in the Kirkendall voids, and the longitudinal fracture events the cluster near the voids.

allow for the deepest penetration of cracks nucleated during polishing. Thus, if the filament pack in this variety of strand is clean and undamaged, the remaining strands in the metallographic puck can be safely assumed to be free from polishing damage, also.

3.3 Deep etching of Cu matrix

One significant limitation of any mount-and-polish metallographic technique is that the surface imaged is two-dimensional. Thanks to the twisted, multifilamentary geometry of the strand, understanding how observed features interact with the rest of the wire volume can be a serious challenge. To better understand the three dimensional nature of the fracture, we have developed a matrix etching technique that dissolves the interfilamentary and stabilization Cu, exposing the filament pack.

To perform this etch, a flat, polished metallographic puck containing Nb_3Sn strand mounted in transverse cross-section was immersed in a 50 vol.% solution of HNO_3 in water.

After 20 minutes, the sample was extracted, rinsed gently but thoroughly with deionized water and ethanol, and then re-introduced to the acid solution for an additional 20 minutes, with the same cleaning procedure repeated afterwards. After these two 20 minutes treatments, approximately 300 μm of Cu had been etched, and the sample appears as shown in figure 3.8. The broken filaments are the result of a previous mechanical deformation (see chapter 6 for additional details), and by removing the Cu the mechanical support of the broken filaments is removed, causing them to crumble at the location of the pre-existing cracks. This technique is primarily useful for examining the three-dimensional fracture field, but it is also useful for comparing the fracture behavior to the longitudinal cross-sections. With a deep etching technique, several hundred microns of depth can be sampled, well away from the polished surface where concerns about preparation damage may remain. Thus, a qualitative comparison of the fracture morphology in the etched sample can be made to the fracture morphology in the longitudinal cross-section to determine if the morphology of the polished sample is representative of the bulk fracture distribution. This discussion is expanded upon in chapter 6.

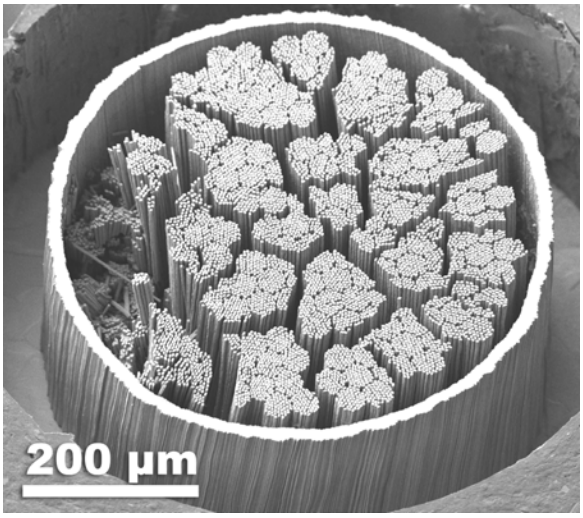

Figure 3.8. Scanning electron microscope image of a bronze-route Nb_3Sn strand after deep etching for 40 minutes total in 50% HNO_3. The filament pack bundle is now unsupported, allowing those filaments that were previously fractured by mechanical testing (left side of this image) to crumble.

3.4 Notes on sample sectioning

In general, Nb_3Sn wire samples mounted for metallographic examination have been sectioned from a larger piece of strand. This naturally brings into question the effect of the sectioning method on the internal fracture morphology of the filament bundle. Figures 3.9 and 3.10 show the effect of sectioning with a small pair of diagonal cutting pliers on a virgin bronze and internal tin strand, respectively. The bronze strand exhibits cutting-related fracture to a depth of about 100 μm, while the internal tin strand exhibits cutting-related damage to a depth of about 200 μm. Both of these damage zones are acceptable for samples which typically are 5 – 10 mm in length. Figure 3.11 shows the greatly reduced damage zone achievable by sectioning the strand with a low speed precision diamond saw. While this technique significantly reduces both the number and spatial extent of cutting-related cracks, it is also significantly more time-consuming and is recommended only when preservation of maximum sample volume is absolutely critical.

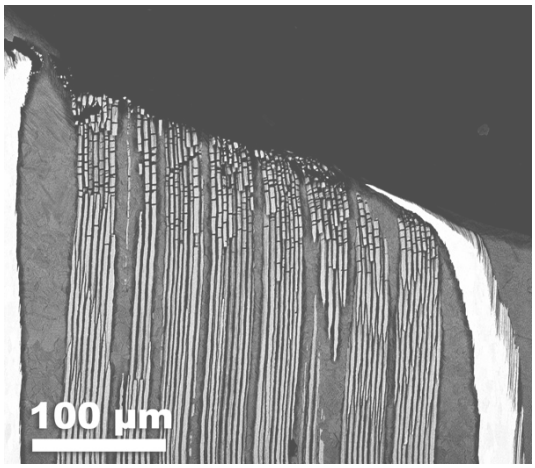

Figure 3.9 Bronze-process Nb_3Sn strand after sectioning with diagonal cutting pliers. The damaged area is limited to about 100 μm.

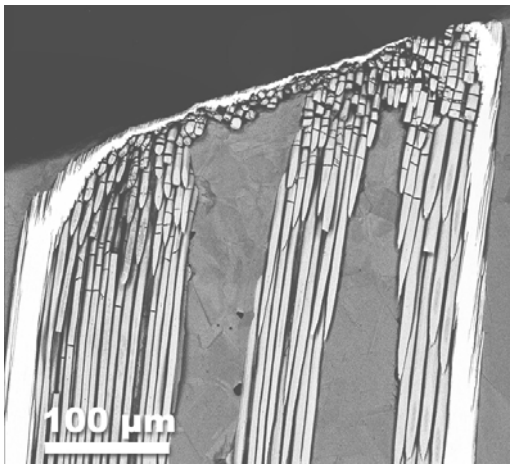

Figure 3.10 Internal tin Nb_3Sn strand after sectioning with diagonal cutting pliers. The damaged area is limited to about 200 μm.

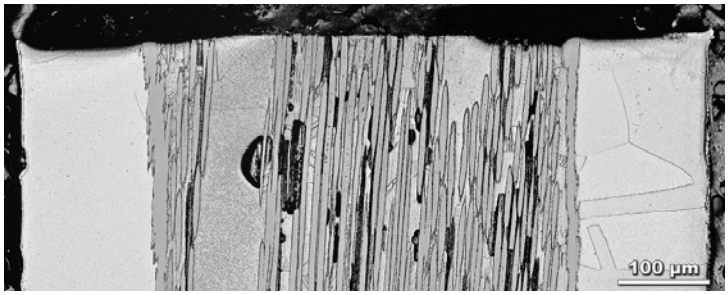

Figure 3.11. An internal tin Nb_3Sn strand after sectioning with a slow-speed diamond saw. Note the very low density of fracture events thanks to the low-force cutting technique. Image courtesy Peter J. Lee.

3.5 Imaging by Field Emission Scanning Electron Microscopy (FESEM)

Field emission scanning electron microscopy (FESEM) was used as the primary technique for sample imaging. The primary advantages of this technique over conventional light microscopy are high resolution (due to the short wavelength of the 10 kV electrons) and large depth of field (due to the narrow objective aperture). When a backscattered electron detector is used, atomic number contrast is also observable.

For this work, a Zeiss 1540 EsB or XB microscope was used for image acquisition. Except where explicitly noted, backscatter electrons (BSE) were used to image the sample. While secondary electrons are more sensitive to surface topology (and therefore might seem to be the more likely acquisition choice for an investigation involving cracks) and are capable of higher-resolution imaging, backscattered electrons can produce atomic number contrast (Z-number contrast), which is helpful for differentiating Nb_3Sn from unreacted Nb that might be present in the cores of the filaments. Since the image contrast is chemical rather than topological in nature, it also aids significantly in image processing, which relies on separating features (such as Nb_3Sn filaments from interfilamentary Cu) based on image contrast.

In the backscatter technique, a high voltage (usually 10 kV in this work) beam of electrons is impinged on a sample. Some of these electrons will interact with the nuclei of the atoms in the sample, and be ejected back out to the surface of the sample. This process is the loose electromagnetic analogue to the gravitational interaction of a comet (or other object with a highly elliptical orbit) as it approaches a star, orbits it tightly, and is ejected from the vicinity along much the same trajectory as it approached. For electrons, large nuclei (high Z-number) will attract and eject more electrons from the sample than small nuclei, which in turn produces positional contrast on the detector proportional to the Z-number. For a system with known constituents (Cu, Nb, Ta, Nb_3Sn, and bronze in our case), this allows for rapid identification of each material.

3.6 Imaging by Scanning Laser Confocal Microscopy (SLCM)

To complement the FESEM, some images were acquired on an Olympus OLS-3100 Scanning Laser Confocal Microscope (SLCM). The SLCM combines reflected light from a 408 nm violet laser with a confocal (pinhole) detector to produce an image. The short-wavelength laser improves the spatial resolution over conventional light microscopy by a factor of two to four, and the confocal detection scheme restricts the field of view to less than 50 nm, making the system extraordinarily sensitive to height variation on the sample. While this may seem a disadvantage rather than an advantage, it can be combined with a motorized stage that steps the position of the sample (in height) in increments as small as 10 nm. The system acquires an image at each height step, and then combines the images to produce a single image that is in focus at every position, regardless of height. The quantitative height information is also stored, allowing for full three-dimensional reconstruction of the sample

surface. In addition, the system contains an LED white light source, which can provide a color image that, when combined with the laser data, can create a composite image with the resolution of the laser but the color information of traditional light microscopy. This capability, which is shown in figure 3.12, has real analytical usefulness in Nb_3Sn strands, where the level of residual Sn in the Cu after heat treatment often needs to be specified.

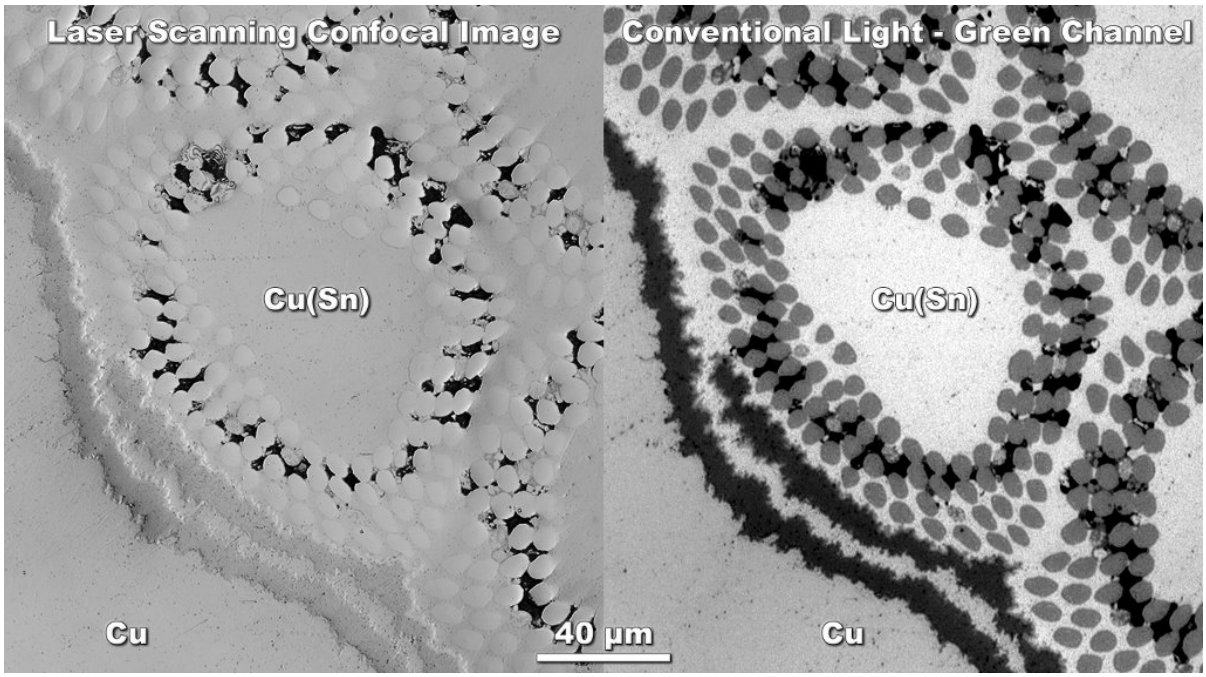

Figure 3.12. Comparison of imaging contrast produced by laser from scanning confocal microscope (left) and by LED white light source (green channel selected) of scanning confocal microscope (right). While the laser has superior spatial resolution and local sample height identification, the white light much more clearly identifies the residual Sn in the sub-bundle core, as contrasted with the much purer stabilization Cu outside the diffusion barrier.

3.7 Imaging techniques not employed

In addition to metallography, there are a number of destructive and non-destructive techniques that might be employed to specify crack density in the Nb_3Sn composite strand. Each is discussed briefly here, including significant advantages and disadvantages.

1. Acoustic emission. This technique takes advantage of the fact that the acoustic impedance in a solid is different at the interface between two materials than it is in the bulk. As a result, an ultrasonic wave propagating through a sample will partially reflect at an interface and return a signal to a waiting transducer. By proper signal analysis, the size and location of the defect causing the reflection can be analyzed. The spatial resolution of this technique has been improved significantly in recent years, and can image defects as small as 10 nm [75]. However, the thousands of filaments in a composite Nb_3Sn wire present too complicated of a structure for reasonable analysis.
2. X-ray tomography. This technique, also known as synchrotron microtomography, utilizes the x-ray absorption properties of different materials within a composite to construct a three-dimensional image of the internal structure [76]. This technique has been used recently to image the evolution of Kirkendall voids in internal tin Nb_3Sn conductors [77] and large cracks in PIT Nb_3Sn conductors subject to transverse load [78]. The latter is shown in figure 3.13 (next page). Note the radial cracks that form after deformation. This technique is ideal for assessing the extent to which these cracks remain parallel to the filament axis as they propagate longitudinally along the filament. This is significant because any development of a transverse component will

be a location of local critical current suppression. Unfortunately, this technique can at the present time only image the largest cracks (in these 50 μm diameter PIT filaments) and does not have sufficient spatial resolution to image cracks in 3 – 5 μm bronze or internal tin filaments.

3. Complete strand etching. Etching is a gentle technique that, while destructive, is highly unlikely to introduce extraneous filament damage during sample preparation. Imaging cracks by this method has been done by the Russian Nb_3Sn manufacturer Bochvar [79], although in our estimation the loss of relative position information amongst the composite components makes this a less attractive option than metallographic preparation.

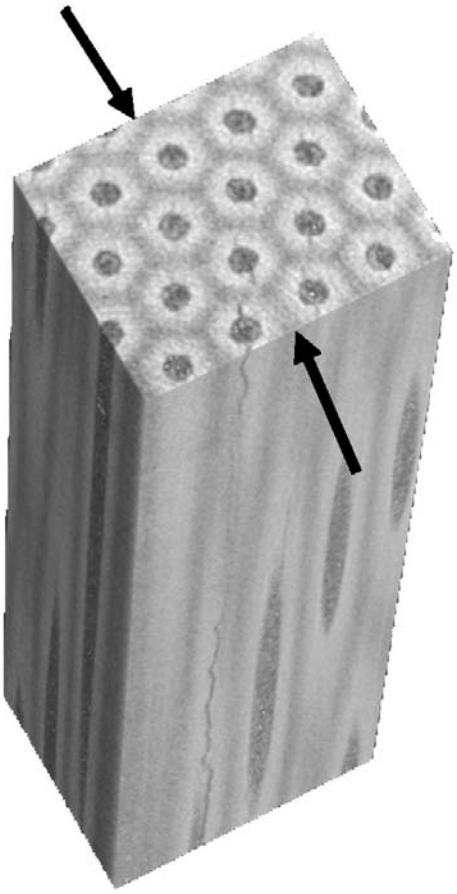

Figure 3.13. Absorption synchrotron microtomograph of a PIT Nb_3Sn strand, after transverse compression testing to approximately 1 kN. Note the longitudinal cracks clearly revealed by this technique. Image courtesy C. Scheuerlein and M. DiMichiel.

CHAPTER 4 – QUANTITATIVE METALLOGRAPHY

Understanding the relationship between fracture and strand architecture requires quantitatively specifying the architecture of the strands under investigation. Here, we consider seven Nb_3Sn commercial strands. Four are ITER-style strands, which are characterized by J_c values in the range of 600 – 1200 A/mm^2 at 12 T, 4.2 K, and low (< 600 mJ/cm^3) hysteresis losses as measured with a ±3 T hysteresis loop [80]. Structurally, the individual filaments in ITER-style wires tend to be separated or only partially agglomerated, with a single diffusion barrier around the filament bundle and fabricated with a bronze or internal tin architecture. Three strands under investigation are high energy physics (HEP) strands, which are characterized by much higher J_c values (1700 – 3000 A/mm^2 at 12 T, 4.2 K) and a high degree of filament agglomeration within the sub-bundles. Internal tin or PIT fabrication approaches tend to be employed for these strands, with distributed diffusion barriers (see figure 2.6) to control Sn leakage into the stabilizing Cu. It is important to understand the different magnet requirements for these two categories of strand. ITER-style strands are more likely to be used in a cable-in-conduit configuration, where local strain values may extend into the tensile regime, and fast ramping or pulsed magnet operation requires low hysteretic losses. HEP strands are most likely to be used in a potted accelerator dipole or quadrupole magnet, where thermal contraction differences between the structural

materials and the magnet conductor introduce a very large compressive pre-strain that effectively prevents the wire from ever experiencing tensile strains, even at maximum Lorentz forces. It should be noted that ITER-style strands in a CIC configuration also experience a large pre-strain from the cable jacket [81], but because of the complicated, multi-stage twist pattern and void space in the cable, this pre-strain does not have the effect of maintaining compressive forces everywhere [25].

Given the very different strain and loading environments of ITER and HEP strands, it might seem reasonable to apply different strand-level strain tests to best simulate the loading conditions experienced in real magnet operation. In this thesis, however, we will attempt to apply similar strain tests to all conductors, in order to ascertain the extent to which strand architecture affects the fracture properties of the material. Our goal is both to influence long-term strand design, and also to address the new issues posed by some recent higher current density magnets (the EFDA dipole and NHMFL series connected hybrid, both discussed in chapter 1), which have crossed over and are using HEP-style strand in a CIC conductor. This makes it all the more important to have a clear sense of how strand design choices affect the fracture properties of the wire.

To determine the effect of strand architecture on fracture propensity, then, the strand architecture must first be quantified. Transverse cross-sections of the ITER-style strands under consideration are shown in figure 4.1, and similar images of the HEP strands under investigation are shown in figure 4.2. Some simple strand identifying information, including acronyms that will be used throughout this thesis to identify the strands, are shown in table 4.1.

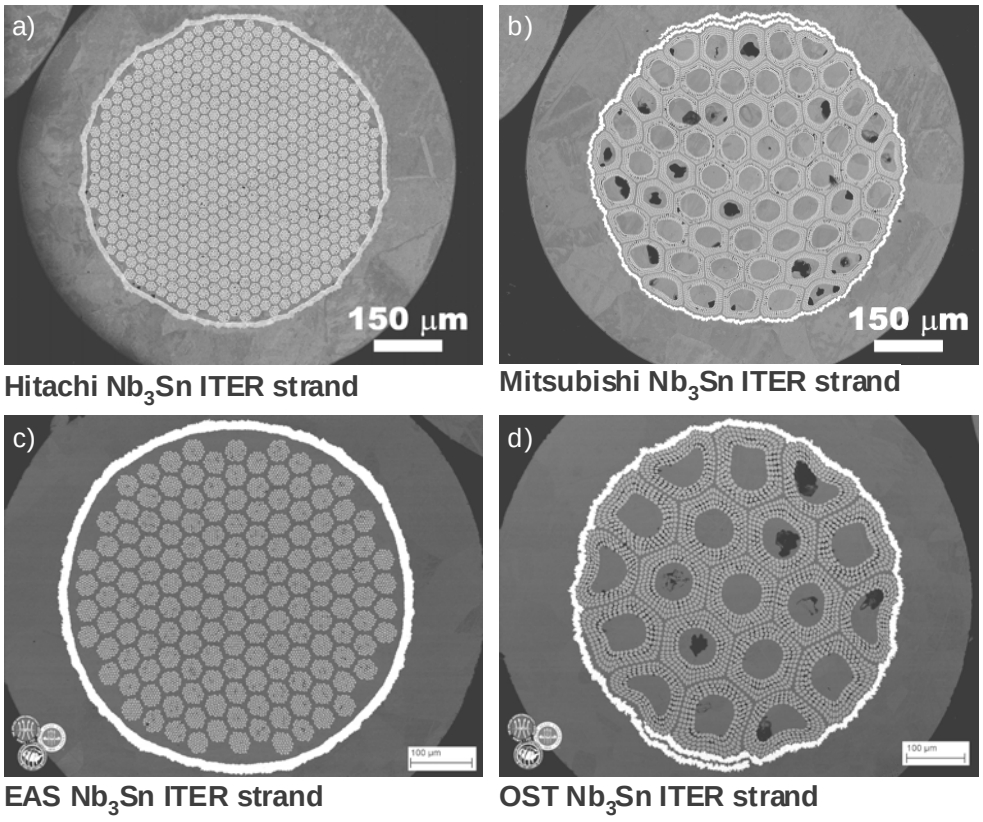

Figure 4.1. Polished transverse cross-sections of four ITER-style Nb_3Sn strands examined in this study.

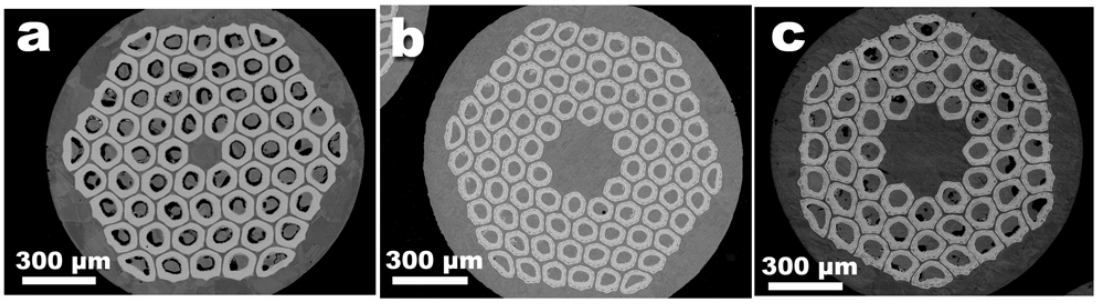

Figure 4.2. Polished transverse cross-sections of three HEP-style Nb_3Sn strands examined in this study. Each of these strands is manufactured by Oxford Instruments – Superconducting Technology (OST) using the Rod Restack Process (RRP). The critical current densities (12 T, 4.2 K) are (a) 3000 A/mm^2, (b) 2400 A/mm^2, and (c) 1700 A/mm^2.

Table 4.1. Nb_3Sn strands investigated in this study

Manufacturer	Acronym	Strand Type
European Advanced Superconductors	EAS	Bronze Process
Hitachi	HIT	Bronze Process
Mitsubishi	MIT	Internal Sn – ITER
Oxford Instruments – Superconducting Technology	OST-ITER	Internal Sn – ITER
Oxford Instruments – Superconducting Technology	OST-3000*	Internal Sn – HEP
Oxford Instruments – Superconducting Technology	OST-2400*	Internal Sn – HEP
Oxford Instruments – Superconducting Technology	OST-1700*	Internal Sn – HEP

*For the Internal Sn – HEP strands, the value XXXX in OST-XXXX is the J_c at 12 T, 4.2 K.

Each of these strands will be investigated using image analysis techniques that allow for the specification of filament number, size, and spacing within the bundle. Generically, this is done by using the contrast produced in the backscatter electron image to threshold the image for various components (filaments, interfilamentary Cu, diffusion barrier, etc.) Certain aspects of this technique have been developed specifically for this work, such as the development of a Microsoft Excel macro that is able to group image pixels into filaments and find the nearest neighbor in the perimeter of an adjacent filament to a pixel in the perimeter of the filament of interest. However, two very complete descriptions of the general image analysis approach are provided in the theses of Naus [32] and Fischer [82]. A very thorough yet readable treatment of image processing techniques is provided by Ross [83].

4.1 Heat treatment

The heat treatment (HT) schedule recommended by manufacturers is often encumbered with intellectual property restrictions, since the development of a procedure to

maximize A15 layer growth without unnecessarily enlarging the A15 grain size is a non-trivial task and can confer significant advantages in critical current density. For example, a PIT strand being investigated for the Next European Dipole [84] experiment was recently shown to exhibit a 7% increase in J_c at 12 T, 4.2 K [51] by manipulating the heat treatment (lower temperature, longer time) to retard grain growth and allow for better Sn homogenization.

Without revealing heat treatment specifics, however, a few general observations can be made about the heat treatments typically employed. Bronze strands, with their simple reaction sequence of Cu(Sn) + Nb → Nb_3Sn + Cu(Sn), usually require a single heat treatment step between 600°C – 700°C, with a duration of 100 h – 200 h. Internal tin strands, on the other hand, have a much more complicated heat treatment schedule, since the pure Sn in the core must first mix with the surrounding Cu before reacting with the Nb filaments. Depending on the heat treatment temperature and duration, the reaction can form binary Cu-Sn phases [85] (including the liquid Cu-Sn phase), and even ternary Cu-Nb-Sn phases [86], which can have the deleterious effect of solutioning some Nb out of the filament pack, thereby reducing the amount of Nb available for reaction to Nb_3Sn. To best control this process, internal tin manufacturers have developed strand-specific, often proprietary intermediate Cu-Sn annealing steps to form the desired intermediate phases that will be most conducive to Nb_3Sn formation. For this purpose, the tie lines in the Cu-Sn phase diagram [87] are often used as a guide to setting the reaction temperatures of interest. It is not, however, clear that the tie lines are sufficiently well known (particularly in the ternary Cu-Nb-Sn system) to predict all heat treatment outcomes.

One significance of the heat treatment to fracture is that the conversion of Nb to Nb_3Sn causes the filaments to swell (the theoretical volume increase of Nb converted Nb_3Sn, based on lattice parameter differences, is 36.5%). This affects the size, spacing, and extent of agglomeration of the filaments, which may in turn affect the fracture propensity of the filament pack.

The strand architecture of the four ITER-style strands will be investigated in sections 4.2 – 4.6, and that of the three HEP-style strands will be investigated in sections 4.7 – 4.8.

4.2 Properties of ITER-style strands

Post-heat treatment, transverse cross-sections of the ITER strands under investigation were shown in figure 4.1, with strand design parameters shown in Table 4.2 (below). The Hitachi and EAS strands are traditional bronze-route conductors, utilizing a high-Sn bronze (15 wt.% [44]) doped with a small amount of Ti to react and alloy the Nb filaments [88]. These manufacturers both design the strand with around 10,000 filaments, with the significant difference being that the Hitachi strand divides those filaments into 583 sub-bundles, while the EAS strand consolidates the filaments into 151 bundles. The Mitsubishi

Table 4.2. Filament architecture of selected ITER strands

Strand design	**HIT**	**MIT**	**EAS**	**OST-ITER**
Type	bronze	IT	bronze	IT
Filaments/bundle	19	224	55	163
Bundles/strand	583	61	151	19
Total filaments	11077	13664	8305	3097
% breakage				
One filament	0.009%	0.007%	0.012%	0.032%
One sub-bundle	0.2%	1.6%	0.7%	5.3%

and Oxford strands are both internal-Sn, with Ti added to the unreacted Sn core to provide alloying. Oxford has also developed an iteration of this strand design in which Ti alloying is provided by Nb-46wt.%Ti rods that have been inserted into the filament pack [89]. This iteration is not evaluated here.

The immediate fracture-related implications of the strand design choice are shown in Table 4.2. In a strand with thousands of filaments, it is unreasonable to expect zero cracking under the loading conditions of a large magnet system such as the ITER TF coil. The goal, rather, is to minimize the frequency of the fracture events, and prevent existing cracks from propagating to neighboring filaments. In a strand like Hitachi, cracking one filament removes less than 1 part in 10^4 of current-carrying cross-section, and even fracturing an entire sub-bundle removes only 0.2% of the current-carrying cross-section. By contrast, the Oxford internal tin strand carries fully five percent of the current density in each sub-bundle, making a fracture event that destroys the entire sub-element potentially catastrophic.

4.3 Heat treatment effect on filament reaction

The microstructure of the filament pack for each conductor as a function of heat treatment is shown in figures 4.3 – 4.6. For each heat treatment, the manufacturer recommended (or cable test recommended) heat treatment was used, with samples pulled out at strategic intervals for microstructural investigation via quantitative image analysis and crack testing. The specific pull-out intervals are listed in the caption of each figure. Although an effort was made to pull out samples at roughly equal intervals in the A15 formation process, this was necessarily complicated by the unique HT conditions used by each manufacturer. Here is the general sample set desired from the pull-out matrix:

- Unreacted sample
- Sample after each intermediate Cu-Sn mixing step (not always shown here)
- Sample after a "candy-coating" of Nb_3Sn (1/3 of the total A15 HT)
- Sample after approximately 2/3 of the total A15 HT
- Full reaction
- Small (20 hr) over-reaction to minimize the presence of unreacted cores. This step had, in general, little microstructural impact and so is not analyzed extensively.

Note: the 1/3 and 2/3 reaction times were not determined on a linear scale, but rather on the following logarithmic scale:

$$x = (kt)^n \tag{4.1}$$

where x is the diffusion distance, k is the diffusion constant (arbitrary in this evaluation), n is the diffusion exponent (set to 0.3 in this evaluation), and t is the reaction time. The microstructure of each ITER strand, as a function of heat treatment, will be briefly described in the following sections.

4.3.1 EAS strand heat treatment

The microstructural development during heat treatment of the EAS strand is illustrated in the SEM images of figure 4.3. These filaments are well-spaced in both the unreacted and the reacted conditions, and there is no filament agglomeration at any point in the heat treatment process. Additionally, the final reaction produces filaments that are almost entirely reacted, with very little Nb left in the filament cores.

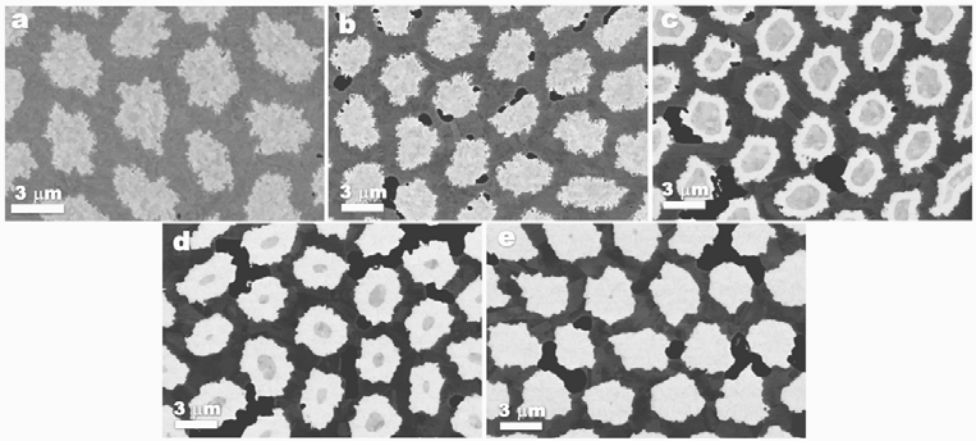

Figure 4.3. Scanning electron microscope images (backscattered electrons) of the EAS strand microstructure at successive stages of the manufacturer recommended heat treatment. Shown are images after (a) no reaction, (b) intermediate anneal, (c) short A15 HT, (d) intermediate A15 HT, and (e) full A15 HT.

4.3.2 Hitachi strand heat treatment

The Hitachi strand is shown in Figure 4.. Like the EAS strand, this bronze-processed architecture begins with a uniform distribution of Nb filaments and maintains that distribution through the heat treatment without any evidence of filament agglomeration.

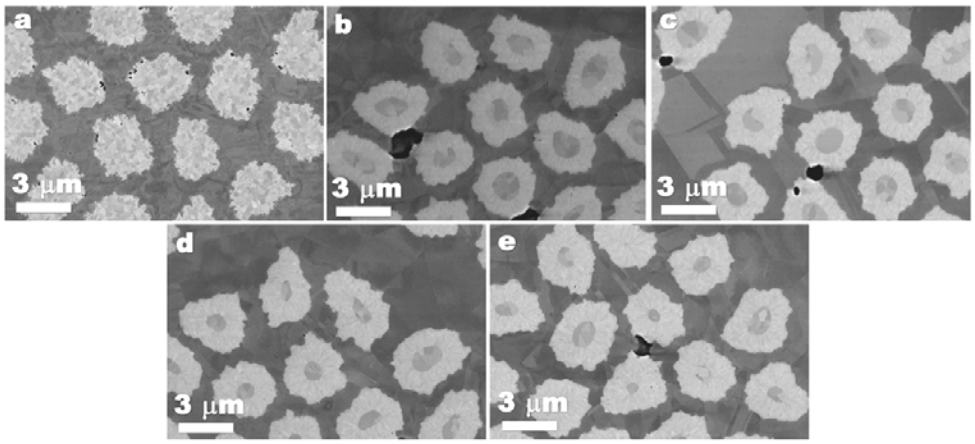

Figure 4.4. Scanning electron microscope images (backscattered electrons) of the Hitachi strand microstructure after variable heat treatment. Shown are images at successive stages of the manufacturer recommended heat treatment (a) no reaction, (b) short A15 HT, (c) intermediate A15 HT, (d) full A15 HT, and (e) extended A15 HT.

However, unlike the EAS strand, the Hitachi heat treatment does not produce a fully reacted cross-section. In fact, after the initial reaction sequence (figure 4.4b), the microstructure appears to be substantially reacted. It is clear from the quantitative analysis of the filament sizes as a function of heat treatment (section 4.4, below) that some growth of the A15 continues, but clearly the system is not tending towards fully-reacted filaments even though both the EAS strand and the Hitachi strand spent similar times at the A15 reaction temperatures. These otherwise similar strands represent contrasting design philosophies regarding the desirable degree of filament reaction.

4.3.3 Mitsubishi strand heat treatment

The Mitsubishi strand is shown in figure 4.5. The initial reaction sequence produced

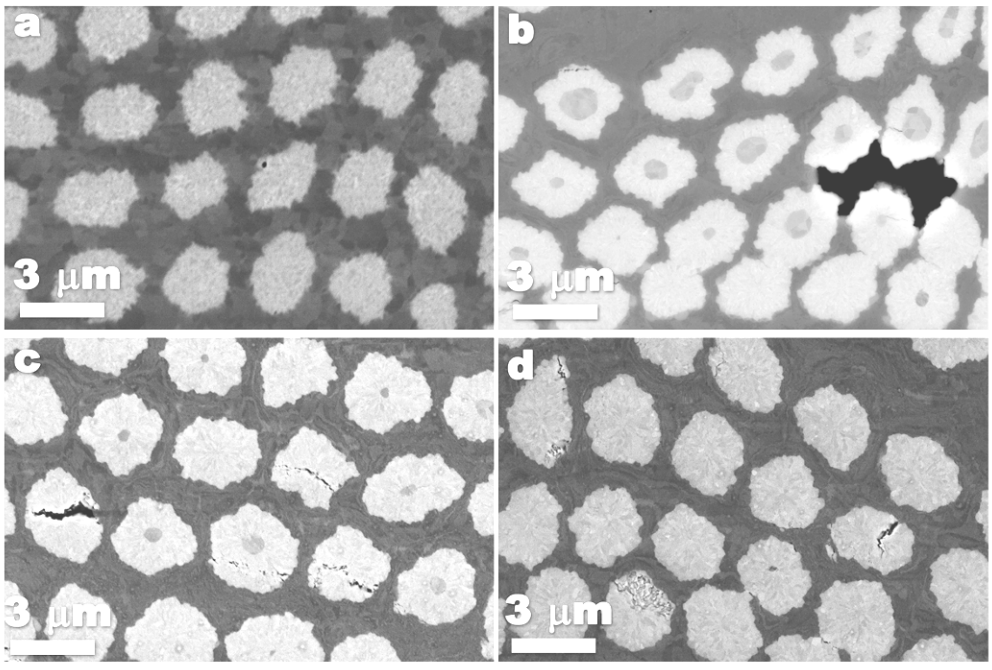

Figure 4.5. Scanning electron microscope images (backscattered electrons) of the Mitsubishi strand microstructure at successive stages of the manufacturer recommended heat treatment. Shown are images after (a) no reaction, (b) initial A15 HT, (c) intermediate A15 HT and (d) full A15 HT.

most of the Nb_3Sn layer, fully reacting the inner row of filaments in many cases. Some filament agglomeration is evident after this step, and indeed after every step in the A15 heat treatment. However, this agglomeration varies from bundle to bundle, so, for example, the bundle imaged in figure 4.5d shows less agglomeration than the bundle in figure 4.5b. The final heat treatment produces fully-reacted filaments. In general, the agglomeration is limited to the first two filament rows of the sub-bundle.

4.3.4 Oxford strand heat treatment

The Oxford strand is shown in figure 4.6. This strand is unique for three primary reasons. First, the filaments are much larger (about three times the area) than the other strand architectures, causing the electric current to be carried in approximately 3,000 filaments (as opposed to ~10,000 for the other ITER-style strands). Second, there is more agglomeration

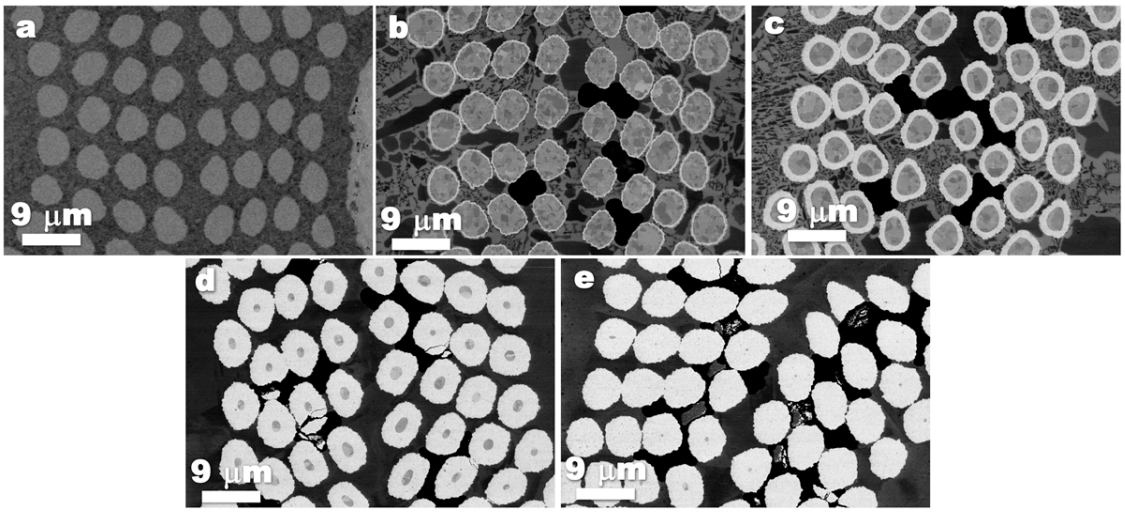

Figure 4.6. Scanning electron microscope images (backscattered electrons) of the Oxford strand microstructure at successive stages of the manufacturer recommended heat treatment. Shown are images after (a) no reaction, (b) intermediate anneal (c) short A15 HT, (d) intermediate A15 HT, (e) full A15 HT.

of the inner-row filaments after reaction than in the other strand designs, even very early in the heat treatment process. Third, there is a significant amount of filament movement that occurs very early in the heat treatment process, as can be seen by carefully comparing figures 4.6a and 4.6b. In figure 4.6b, almost all the filament agglomeration present at the end of the heat treatment has already occurred. This observation will be further explored in section 4.4.2, below.

4.4 Quantitative analysis of filament growth

The mean area of filaments from a central sub-bundle is shown in table 4.3, and the growth of those filaments relative to the unreacted filament size is shown in figure 4.7. The mean filament area is calculated by averaging the sizes of all filaments in a sub-bundle, which ranges from 38 (two sub-bundles, HIT) to 224 (MIT). The coefficient of variation (the ratio of the standard deviation to the mean) of the filament areas is presented in table 4.4. A few significant results, from both the imaging and the quantitative analysis, are summarized below.

Table 4.3
Filament area (μm^2)

HT step	HIT	MIT	EAS	OST
Unreacted	7.72	4.47	7.80	22.90
Candy-coat	8.78	5.92	7.92	24.92
2/3 reaction	9.04	6.08	8.49	27.65
Full reaction	9.09	6.15	9.04	31.13
20 hr over-reaction	9.31	6.25	9.43	30.69

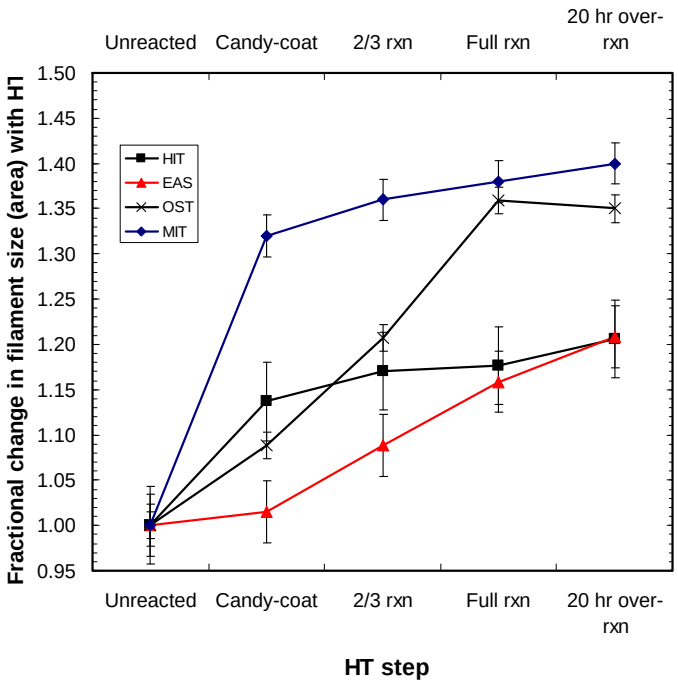

Figure 4.7. The fractional growth of filament area as a function of heat treatment progression. Note that the bronze strands behave almost identically, expanding about 20% during the reaction. The internal-tin strands expand significantly more with the smaller Mitsubishi filaments expanding more than the OST filaments. The error bars represent a 95% statistical confidence interval for the mean value of the filaments sampled.

4.4.1 Bronze strands

The two bronze strands (Hitachi and EAS) have remarkably similar architectures. The initial (unreacted) and final filament sizes are within 2% of each other, and the filaments maintain a uniform size and spacing throughout the heat treatment. Both samples experience filament growth of around 21% over the course of the heat treatment. The coefficient of variation of filament sizes remains quite constant, around 11% ± 1% (see table 4.4) for both strands throughout the heat treatment, indicating that the filaments grow at a predictable rate and to a predictable degree. This remarkable similarity demonstrates the extent to which the bronze process is a stable Nb_3Sn manufacturing process in the superconducting fabrication industry.

Table 4.4. Filament area coefficient of variation (−)

HT step	HIT	MIT	EAS	OST
Unreacted	0.104	0.143	0.115	0.084
Candy-coat	0.117	N/A	0.123	0.080
2/3 rxn	0.114	0.126	0.101	0.091
Full rxn	0.106	0.127	0.116	0.078
20 hr over-rxn	0.107	0.130	0.118	0.080

4.4.2 Internal tin strands

The two internal tin strands (Oxford and Mitsubishi) utilize very different strand architectures and heat treatments. The Oxford filaments are five times larger than the Mitsubishi filaments both before and after reaction, yet react to substantial completion after a relatively short heat treatment. Although the Mitsubishi filaments experience a larger percentage of area growth during heat treatment, the initial small starting filament size of this strand helps ensure that only the inner two rows of the filament pack agglomerate, and even then not in every sub-bundle (see figure 4.5b – 4.5d). The larger Oxford filaments, by contrast, tend to bridge in the first three (out of four) rows of the filament pack (see figure 4.5b – 4.5e). With the smallest starting filament size, the Mitsubishi strand also has the largest coefficient of variation of any strand.

A detailed view of the quenched microstructure after 1 hr of the A15 reaction step in the Oxford strand HT is shown in Figure 4.8. At this early stage of the heat treatment schedule, there is both an inhomogeneous distribution of filaments that has begun to produce agglomeration as well as an inhomogeneous Cu-Sn matrix that appears to have contained a significant liquid component at A15 reaction temperature that is wetting the surface of the filaments. The contrast with the Mitsubishi strand suggests that filament bridging in this

composite might be significantly mitigated by a further optimization of the heat treatment that minimizes the impact of the liquid Cu-Sn phase that forms as part of the initial stages of the IT reaction. However, such a heat treatment schedule will increase heat treatment time and its associated costs.

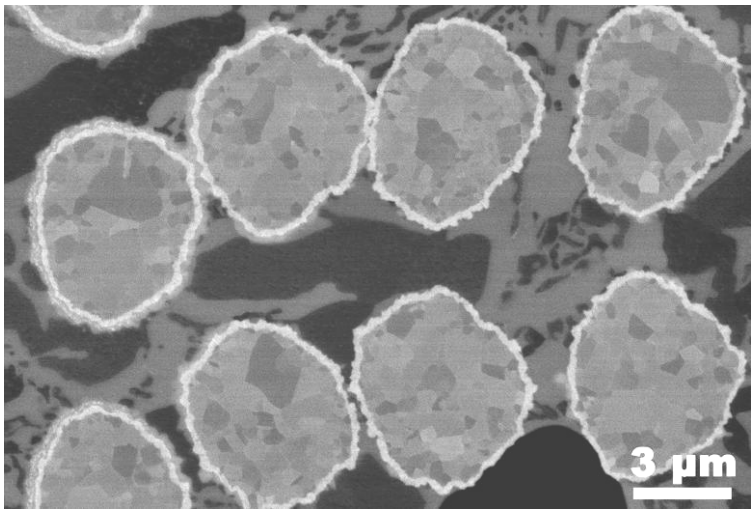

Figure 4.8. Detailed view of the extent of the Nb (darker core) to Nb_3Sn (light ring) conversion as it is occurring after 1 hr of the A15 HT step in the Oxford strand. Notice that after this very short period of time, the filaments are already significantly shifted from their unreacted positions and becoming agglomerated.

Figure 4.8 also demonstrates one of the subtleties of internal tin heat treatment that is not fully understood. Note that the inner row of filaments (left-hand side of this image) nearest the original Sn core have a thin ring of two-phase material surrounding the light Nb_3Sn ring. This is presumably evidence of filament dissolution and detrimental to J_c.

4.5 Strand expansion due to internal mechanical pressure

As the Nb filaments grow during conversion to Nb_3Sn, the wire expands slightly in the radial direction. This expansion is quantified in Table 4.5 in terms of the increase of area evident within the diffusion barrier before and after heat treatment. By comparing this to the change in area of the filament pack before and after heat treatment, we can assess the extent to which the filament growth is manifested by a change in non-stabilizer area.

There are several conclusions to draw from this analysis. First, note that for each strand, there is a non-trivial change in the area within the diffusion barrier. This suggests that the interfilamentary Cu is not behaving like a soft, annealing, high-temperature metal, but is retaining some strength and able to transfer forces to the diffusion barrier. This is a significant point for the strand modeling community as they consider the appropriate initial conditions of the strand at the end of the heat treatment.

Table 4.5
Relative expansion of filaments and area within the diffusion barrier.

Strand	Change in area within diffusion barrier after HT		Change in total filament area after HT		Increase in non-Cu area relative to increase in filament area
	μm^2	%	μm^2	%	%
EAS	3316	1.4%	13537	21%	24%
Hitachi	4700	1.9%	17612	21%	27%
Mitsubishi	9058	3.6%	25415	40%	36%
Oxford	11371	5.1%	25488	35%	45%

Second, note that the internal tin strands expand significantly more than the bronze strands, likely a result of the additional internal pressure from the liquid Cu-Sn phase that forms during heat treatment. Note also that this expansion does not come at the expense of the large void structure in the

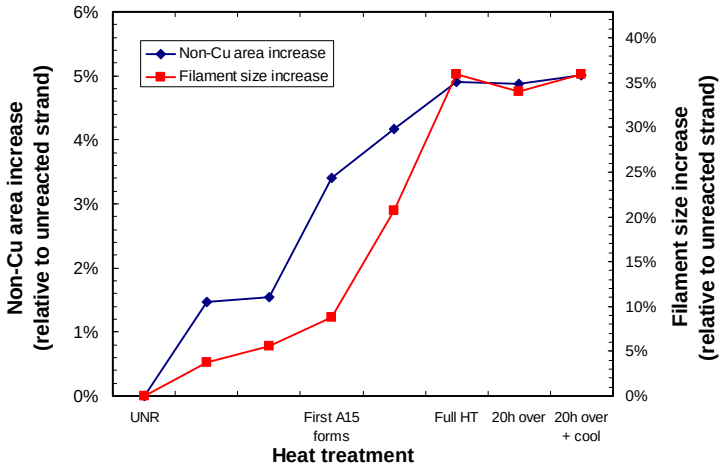

Figure 4.9. Expansion of the area within the diffusion barrier (the "non-Cu" area) and the filament size as a function of heat treatment. Note that the filament size increase significantly lags the non-Cu area increase.

sub-bundle cores (see figures 4.1b, 4.1d). This further reinforces the point that the interfilamentary Cu is maintaining some mechanical strength even at A15 reaction temperatures and not merely flowing to fill in the voids.

This effect is further demonstrated in figure 4.9, which tracks the expansion of the area within the diffusion barrier and the expansion of the filament pack for the Oxford internal tin strand. Note that the filament area increase lags the increase in the overall wire expansion, and that the most significant increase in strand area occurs just prior to the 1 h A15 heat treatment step. This indicates that the Cu-Sn intermetallics formed (including, possibly, a liquid phase) experience a significant volume expansion upon mixing and contribute to the expansion of the area within the diffusion barrier.

4.6 Summary of quantitative metallography of ITER-style strands

We have quantified the architectural properties and growth of the Nb_3Sn filament pack as a function of heat treatment for four ITER candidate strands. The filaments in the bronze strands were shown to expand in area about 20% during heat treatment, and maintain their relative separation throughout the heat treatment process. The filaments in the internal Sn strands, by contrast, showed significant physical movement and some agglomeration during heat treatment. An appropriate heat treatment modification might ameliorate this effect somewhat. For example, the Mitsubishi strand has significantly fewer agglomerated filaments than the Oxford strand, despite the fact that the Mitsubishi filaments expand more aggressively (40%) than do the Oxford filaments (35%).

Conversely, it is less clear that the final heat treatment step can be manipulated to significantly increase the interfilamentary Cu thickness between filaments without drastically

reducing J_c. As shown in figure 4.7, most of the filament area change occurs in the early stages of reaction, before the A15 layer is thick enough to sustain a useful J_c.

The significant variety in step choices and duration of the heat treatment schedules from manufacturer to manufacturer demonstrates that no common design choices have been established, and leads to some concern that the manufacturers require these highly optimized heat treatments to obtain the J_c and hysteretic loss values required by ITER. Strand testing with a common (ITER-specified) heat treatment is recommended as early in the procurement process as possible.

4.7 HEP strand metallography

The HEP strands under investigation are less amenable to filament-level quantitative metallography, since the filament pack tends to agglomerate quickly and therefore blurs the distinction between individual filaments. An analysis of the filament and sub-bundle arrangement is provided in table 4.6. Unlike the ITER strands examined earlier, which contain ~10,000 filaments, these strands utilize 20,000 – 40,000 extremely fine filaments assembled using the patented Rod Restack Process [90]. This makes the J_c degradation impact of a single filament negligible, although in practice (and as will be demonstrated in sections 4.7.1 – 4.7.3) the filament bundles tend to agglomerate significantly. The effect of losing an entire sub-bundle to fracture is significant, as the table demonstrates.

Table 4.6 Filament architecture of selected HEP strands

Strand design Type	**OST-3000 IT-HEP**	**OST-2400 IT-HEP**	**OST-1700 IT-HEP**
Filaments/bundle	684	342	342
Bundles/strand	60	84	54
Dummy Cu filaments in wire core	1	7	7
Total filaments	41040	28728	18468
% breakage			
One filament	0.002%	0.003%	0.005%
One sub-bundle	1.7%	1.2%	1.9%

Images of partial sub-bundles of these three HEP strands are shown in figures 4.10 – 4.12, with a brief analysis of the reaction progression.

4.7.1 OST-3000 A/mm^2 strand heat treatment

The Oxford 3000 A/mm^2 conductor is shown in figure 4.10. This is the highest J_c conductor investigated, and consequently has the lowest amount of interfilamentary Cu, in an effort to maximize the areal fraction of Nb_3Sn. This design is the current record holder for non-stabilizing Cu J_c ($J_{c,\ non\text{-}Cu}$) of any Nb_3Sn strand at 12 T, 4.2 K [90]. Because of the close spacing of the filaments, agglomeration begins to occur very quickly after the initial candy-coat of Nb_3Sn is formed. By the end of the heat treatment, the sub-bundle has reacted to a solid mass of mechanically-connected Nb_3Sn, and the distributed Nb diffusion barrier has largely reacted to Nb_3Sn as well. This contributes additional J_c to the bundle, but also creates a continuous mechanical (and electrically connected) ring of brittle Nb_3Sn around the perimeter of the sub-bundle. Also interesting to note is the dramatic effect that the aggressive heat treatment and high Sn fraction have on the inner row of filaments, which clearly suffer partial dissolution during the heat treatment.

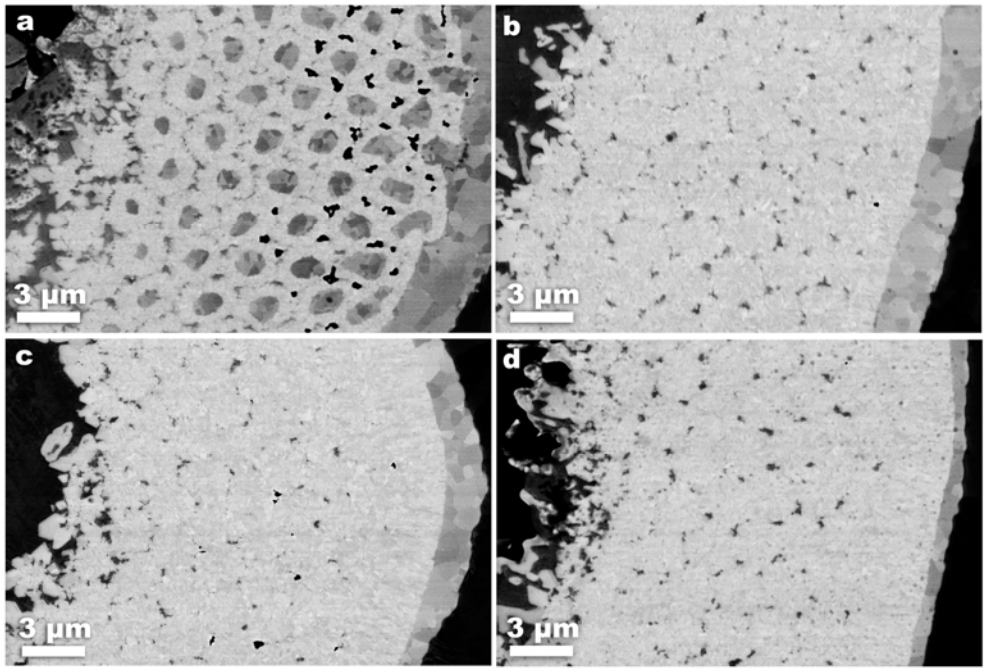

Figure 4.10. Heat treatment progression of an OST-3000 Nb_3Sn strand, after (a) short A15 HT, (b) intermediate A15 HT, (c) full A15 HT, and (d) extended A15 HT. Note the immediate agglomeration of the filament pack and the partial reaction of the Nb diffusion barrier. In each image, the location of the sub-bundle core (the Sn source for the reaction) is to the left. Notice how the aggressive heat treatment has caused partial dissolution of the inner row of Nb filaments.

4.7.2 OST-2400 A/mm^2 strand heat treatment

The Oxford 2400 A/mm^2 conductor (also called the "EFDA-dipole" conductor, since it was selected for that magnet system) is shown in figure 4.11. Much like the 3000 A/mm^2

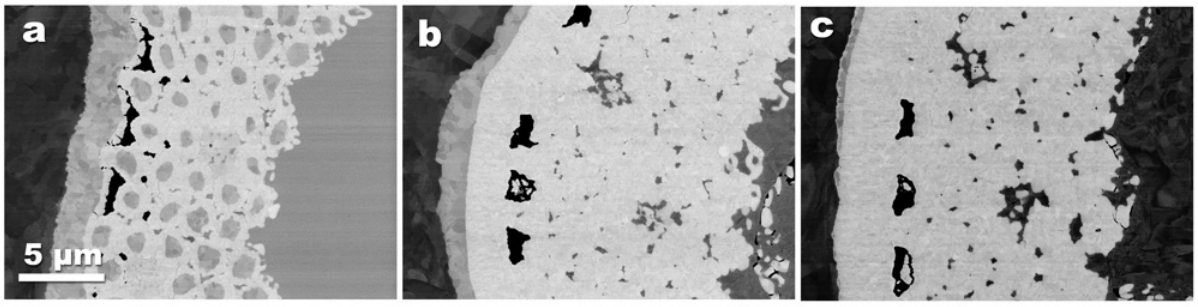

Figure 4.11. . Heat treatment progression of an OST-2400 Nb_3Sn strand, after (a) short A15 HT, (b) intermediate A15 HT, and (c) full A15 HT. Note the immediate agglomeration of the filament pack and the partial reaction of the Nb diffusion barrier. In each image, the location of the sub-bundle core (the Sn source for the reaction) is to the right.

conductor described above, the filaments here are sufficiently closely packed that they agglomerate early in the heat treatment schedule and bond to the diffusion barrier. However, unlike the 3000 A/mm^2 conductor, there is sufficient additional Cu in between the filaments to promote good back-diffusion of Cu into the sub-bundle core, leaving a noticeable void pattern next to the diffusion barrier. Also, the dissolution of Nb at the core-filament interface is significantly reduced relative to the higher-J_c strands.

4.7.3 OST-1700 A/mm^2 strand heat treatment

The Oxford 1700 A/mm^2 Nb_3Sn strand is shown in figure 4.12. In this strand, the lower J_c requirement allows for more volume fraction to be devoted to interfilamentary Cu, which has the effect of better separating the filaments both before and after reaction. In fact, significant agglomeration does not occur until late in the heat treatment process, and even then there is more Cu visible between the filaments and between the filaments and the diffusion barrier than in the higher-J_c strands. Note also the very interesting effect in figure 4.12b, where the intermediate heat treatment has reacted the filaments near the diffusion barrier (far from the Sn source) completely, but has left some remaining unreacted Nb cores

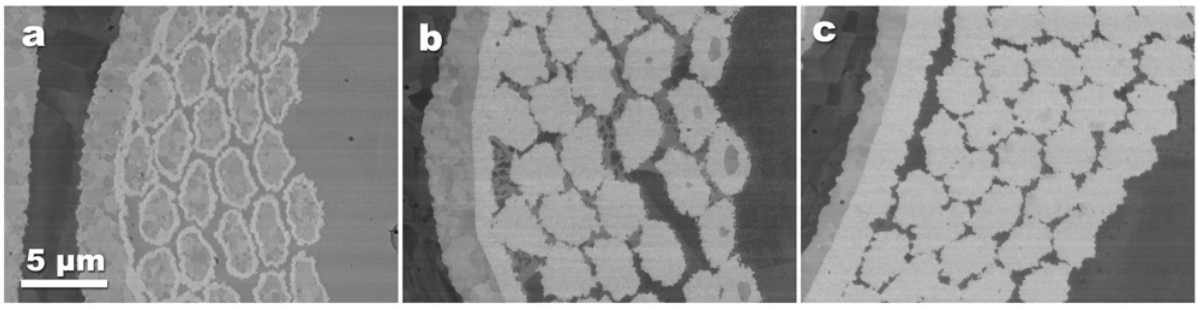

Figure 4.12. Heat treatment progression of an OST-1700 Nb_3Sn strand, after (a) short A15 HT, (b) intermediate A15 HT, and (c) full A15 HT. Note the immediate agglomeration of the filament pack and the partial reaction of the Nb diffusion barrier. In each image, the location of the sub-bundle core (the Sn source for the reaction) is to the right.

in the inner row filaments nearest the Sn source. This does not, with one or two exceptions, seem to be relatable to the filament size (i.e. the inner row of filaments is not significantly larger than those further from the core). This suggests that the very high Sn activity near the core produces some unwanted blocking phases that prevent further Sn reaction with the filament. This is an obvious focus for further heat treatment optimization.

4.8 Summary of HEP strands

The HEP strands demonstrate nicely the architectural complement to the ITER strand design. While ITER strands require a balance between J_c and hysteresis losses, and therefore a balance between filament size and spacing, the traditional slow ramped, non-pulsed applications relevant to HEP has resulted in strand designs that have a much higher density of Nb filaments and subsequent increased filament agglomeration. Additionally, the desire to maximize Sn delivery to unreacted Nb has moved HEP designs to a distributed barrier, which is usually Nb and is allowed to react partially to increase the volume of A15 in the cross section, albeit at a considerable increase in hysteretic loss due to the large area current loops produced by this reaction.

The seven strands investigated here demonstrate a wide range of architectural choices, which reflect both final performance objectives and also practical concerns such as heat treatment schedules and fabricability. What has received very little attention, however, is the extent to which the strand architecture affects the propensity of these composite materials to fail (crack filaments) under loading. In chapters 5 – 7, we will discuss the results of uniaxial, bending, electromagnetic, and micro-indentation investigations aimed at elucidating the

relative mechanical toughness of the filament bundle in each strand, and the mechanisms that give rise to this toughness.

CHAPTER 5 – FRACTURE PROPENSITY UNDER BENDING AND UNDER UNIAXIAL STRAIN

Assessing the performance of specific strands in a real magnet is a time-consuming and expensive endeavor, and the interpretation of the results is less than straightforward. One of the most significant complications associated with interpreting J_c degradation results from cable tests is the complication introduced by the variable strand and cable stiffness values of different strand designs and cable layouts, which makes understanding the interaction between stress and strain at the strand level very complex, which in turn makes predicting the fracture propensity of different strand designs in the final cable difficult to accomplish. Therefore, fracture propensity evaluation at the strand level is useful for specifying the fundamental mechanical toughness of various strand designs, without being obscured by the addition of cable variables. To provide a standardized comparison the propensity of A15 filaments to crack under bending strain, we have developed a simple, pure bending test that deforms different strand designs to a desired bend strain in a uniform, repeatable manner. By subsequent polishing (using the techniques described

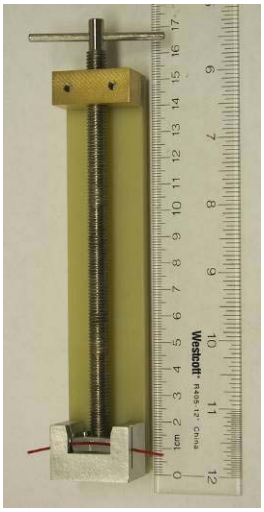

Figure 5.1. 77 K bend clamp apparatus

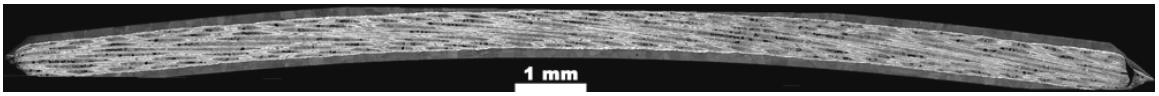

Figure 5.2. Longitudinal cross-section of Mitsubishi Nb_3Sn strand after bend testing to 1.5% peak outer wire strain at 77K and metallographic preparation.

in chapter 3) and image analysis, the fracture morphology of disparate strands can be compared in a fair, side-by-side manner. A picture of the bend clamp rig is shown in figure 5.1, and a polished overview of a strand after bend testing and metallography is shown in figure 5.2. Note that even though the clamp has been removed (this sample was bent to 1.5%), some residual strain is present due to plastic deformation in the Cu. For example, in the Hitachi strand bent to 1.5%, this residual bend strain was measured (by image analysis on the central 5 mm of the bent sample) to be 1.0%. The residual bend is experimentally advantageous, as it allows us to easily identify the tensile and compressive bend axes. As shown in figure 5.2, > 1 cm of sample length was typically imaged.

In this experiment, the strand was loosely inserted into an aluminum clamp that had been machined to a desired bend radius. A groove in the clamp (machined to the diameter of the wire) ensured that the wire did not experience transverse compressive stresses during the clamping procedure. The assembly was then inserted into a liquid nitrogen bath and allowed to cool to 77 K, as a reasonable approximation of

Table 5.1. Mechanical properties of selected components of the Nb_3Sn composite wire system

	Cu			Nb		
Temp (K)	E [GPa]	σ_y [MPa]	ΔL /L (%)	E [GPa]	σ_y [MPa]	ΔL /L (%)
293	128	48.5	0	105	50.5	0
77	136	75.4	-0.285	108	96	-0.127
4.2	137	86.2	-0.334	110	194	-0.148
Deviation from 4.2K value at 77K	1%	13%	15%	2%	51%	14%
	Ta			Nb_3Sn		
Temp (K)	E [GPa]	σ_y [MPa]	ΔL /L (%)	E [GPa]	σ_y [MPa]	ΔL /L (%)
293	180	265.9	0	135	---	0
77	186	457	-0.123	123	---	-0.143
4.2	188	874.3	-0.152	100	---	-0.185
Deviation from 4.2K value at 77K	1%	48%	19%	23%	---	23%

the mechanical properties of the composite at 4.2 K, without requiring an expensive, dedicated cryostat for 4 K testing. Several important mechanical properties of the components of the system are shown at 293 K, 77 K, and 4.2 K in table 5.1. In general, the elastic modulus (E) and thermal contraction of all component materials are within 25% of their 4.2 K value at 77 K. The only significant parameter that falls outside this margin is the yield stress (σ_y) for Nb and Ta, the two BCC metals in this system. However, we do not expect this to influence the testing significantly, since these components only appear in the diffusion barrier and, in the case of Nb, as an unreacted filament core in some strands.

Note that when designing the bend clamp, the thermal contraction of both the strand and the clamp, from room temperature to 77 K, is considered when specifying bend radius and groove depth of the clamp. For example, the Al-6061 bend clamp contracts 0.389% from room temperature to 77 K, so for a wire of 0.81 mm diameter (0.405 mm radius) and a target of 1.0% bend strain, the correct 77 K radius is 40.39 mm, a contraction of 0.16 mm from the room temperature value. This also takes into account the 0.28% decrease in the radius of the wire, as estimated by Ekin [91]. After deformation, the clamp is removed from the cryogenic bath, allowed to warm, and the sample is removed from the clamp. Using the residual bend strain to define the plane of interest, the sample is mounted in longitudinal cross-section and prepared metallographically using the technique described in chapter 3. For the ITER strands, an etch of 13 vol.% HF, 37 vol.% HNO_3, and 50 vol.% H_2O was applied (by immersion) for ~5 seconds prior to imaging. This rather aggressive etch removes any Cu that may have smeared on the surface, and also opens up any existing cracks, making

them more visible during microscopy. This etch was usually not applied to the HEP strands, since, with their agglomerated filament packs, they tend to have fewer and wider cracks.

All four ITER candidate strands (EAS, Hitachi, Mitsubishi, Oxford) and all three HEP strands were tested at 0.5%, 1.0%, and 1.5% bend strain, as measured relative to the overall radius of the wire (0.405 mm). At 1.5% bend strain, samples exposed to both a full heat treatment and a shortened heat treatment were tested.

To analyze the fracture distribution, the position of each crack is specified with respect to the geometric central axis of the wire. The crack location (the distance of the crack from the neutral axis) can then be transformed into a local nominal bend strain, which is then plotted, for example, as the independent variable in figure 5.3. Note that the shift in the neutral strain axis, due to the interaction of bending strain with pre-existing thermal strain, was not calculated for this experiment, although it is expected to be small, and appropriate treatments for Nb_3Sn are available in the literature [92].

5.1 Bend strain results

5.1.1 Bending at 1.5% strain in ITER strands – full heat treatment

The distribution of fracture events as a function of local bend strain is plotted for each of the four ITER candidate strands in figure 5.3. Note that 1.5% is the maximum bend strain imposed at the outer radius of each wire, so the A15 filaments all experience some fraction of this value, depending on the location of the diffusion barrier and the amount of stabilization Cu on the wire. For all strands, the location of the diffusion barrier means that the maximum filament bend strain is between 1.0% and 1.2%.

All strands show dominant fracture behavior near the tensile axis, as expected from a bend test. While no sample is entirely crack free on the compressive side of the axis, the background "noise" of fracture events is minimal and does not affect the interpretation of the results. The bronze strands (EAS and Hitachi) have narrower distributions of fracture events, while the internal tin strands (Mitsubishi and Oxford) have somewhat broader transitions, likely the result of more collective cracking due to filament agglomeration.

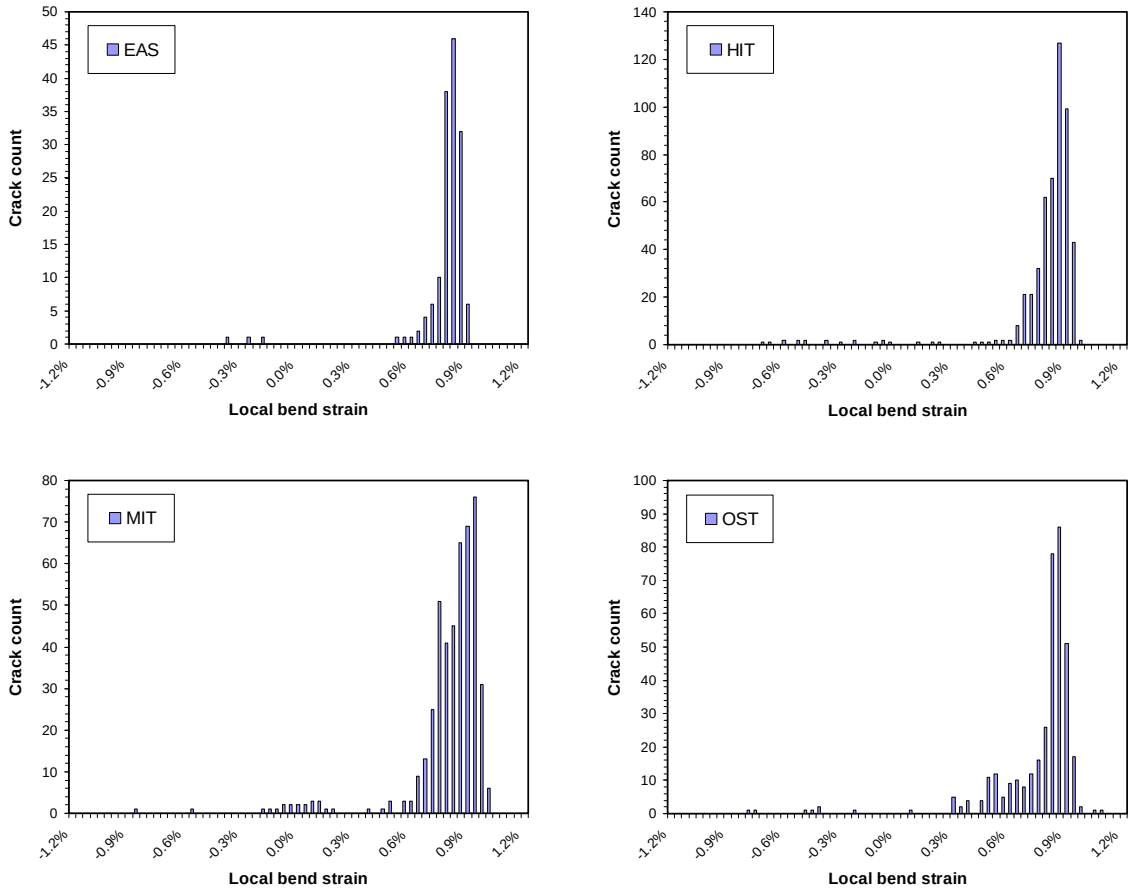

Figure 5.3. Distribution of fracture events as a function of bend strain in (a) EAS, (b) Hitachi, (c) Mitsubishi, and (d) Oxford ITER Nb_3Sn strands. All strands have an onset of fracture near 0.7% bend strain, with the exception of Oxford, which begins to fracture near 0.4%.

EAS, Hitachi, and Mitsubishi all begin to fracture at approximately the same bend strain value (about 0.7%). The Oxford strand, however, begins to fracture at a significantly lower value, around 0.4% - 0.5%. This is likely due to the larger size of the Oxford filaments (at least three times larger in area than the other strands). The absolute number of fracture events in each wire varies significantly, as will be discussed in table 5.2 at the end of this section.

A montage of fracture events in these fully-reacted 1.5% bend strain samples is shown in figure 5.4. Note that each of these images provides a detailed view of the tensile side of the wire, in order to highlight the area of significant fracture. The internal tin (Oxford and Mitsubishi) samples exhibit more collective cracking (two to four filaments clearly cracking together), while the bronze samples fracture more individually. In one location, it even appears that a crack in the Oxford sample has propagated azimuthally around the core of the sub-bundle and has fractured filaments on the opposite side of the core. This long-range fracture propagation may help explain the broader fracture distributions seen in the frequency plots, as the propagating cracks sample more local strain values than do individual cracks. The contrasting individual/collective cracking behavior is consistent with the filament agglomeration behavior already described in chapter 4. Examining figure 5.4 carefully, the Oxford collective cracks tend to span the inner three rows of the filament pack in the sub-bundle, but not the fourth (outer) row of filaments, which is consistent with the agglomeration of the inner three rows of filaments seen in figure 4.6. The Mitsubishi cracks, by contrast, tend to span the inner two rows of filaments (though exceptions can be found), consistent with the agglomeration of those two rows in figure 4.5. The individual cracking

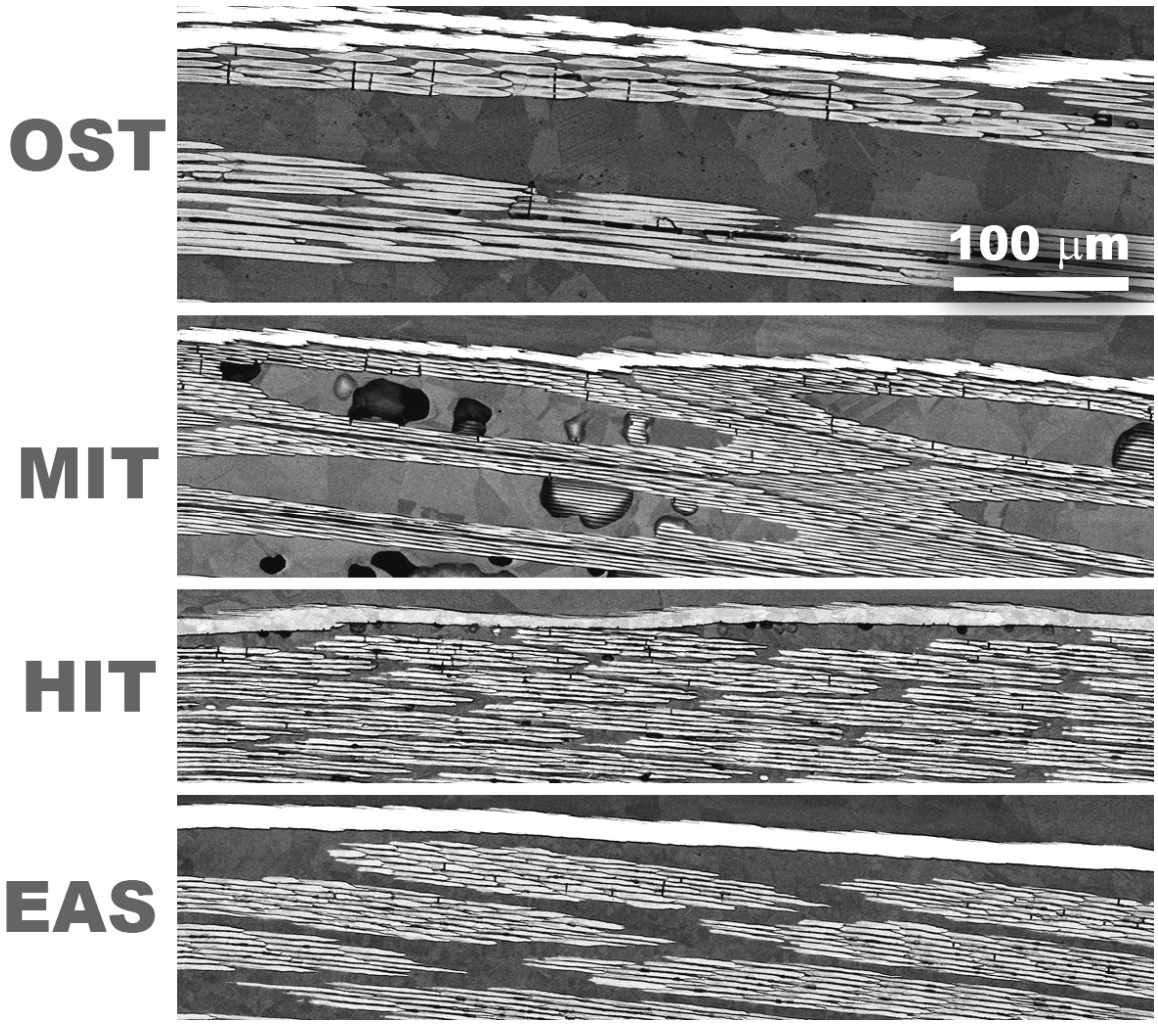

Figure 5.4. Fracture near the tensile axis in four ITER candidate strands. The internal tin strands (OST and MIT) exhibit more collective cracking, while the bronze strands (HIT and EAS) exhibit more individual crack events. Note also that the sample has been etched with an HF-based solution to allow for easier crack identification.

behavior of the EAS and Hitachi strands is also consistent with the well-separated filaments shown in figures 4.3 – 4.4. Although it is difficult to see at this magnification, the fracture events in these two bronze conductors tend to be arrested by the interfilamentary Cu and do not produce evident cracking in the ductile Cu-Sn matrix that exists between the filaments.

5.1.2 Bending at 1.5% strain in HEP strands – full heat treatment

While intuitive, the comparative tests presented here represent the first experimental confirmation of the effect of filament agglomeration on the fracture propensity of the

filaments in the strand. While the differences are somewhat subtle amongst the various ITER strands, they are absolutely clear in the HEP strands. Figures 5.5 – 5.7 show the effect of 1.5% bend strain (relative to the full wire diameter) on the OST-3000, OST-2400, and OST-1700 strands, respectively. In each strand, cracks are observed to nucleate near the tensile axis (the top of each image) and propagate through the agglomerated filament packs to near the neutral axis. There is a distinct periodicity to the spatial arrangement of these dominant cracks, which repeat themselves every 300 – 600 μm. This fracture pattern is capable of producing catastrophic damage to J_c, since, in a twisted strand, each sub-bundle will rotate to the tensile axis over the course of a twist pitch. In each of these three images, the full wire cross-section is shown.

Perhaps the most intriguing conclusion to draw from this experiment is that, from a strand selection point of view, all strands with agglomerated filament packs behave about the same with respect to fracture propensity. That is, once an agglomerated filament design is accepted, the J_c can be increased by almost a factor of two (1700 A/mm^2 to 3000 A/mm^2) without qualitatively changing the fracture behavior. Conversely, attempting to lower the J_c for the purpose of improving the fracture resistance will be ineffective unless agglomeration in the filament pack is eliminated (or at least reduced to the level of ITER-style internal tin wires).

A closer examination of sub-bundle fracture reveals additional items of interest, as shown in figure 5.8. This image, which examines a single sub-bundle of OST-3000 that was cracked by bending to 1.5% at 77 K, shows a series of fracture events across the superconducting layer. The interfilamentary Cu (the dark streaks in the Nb_3Sn layer) are

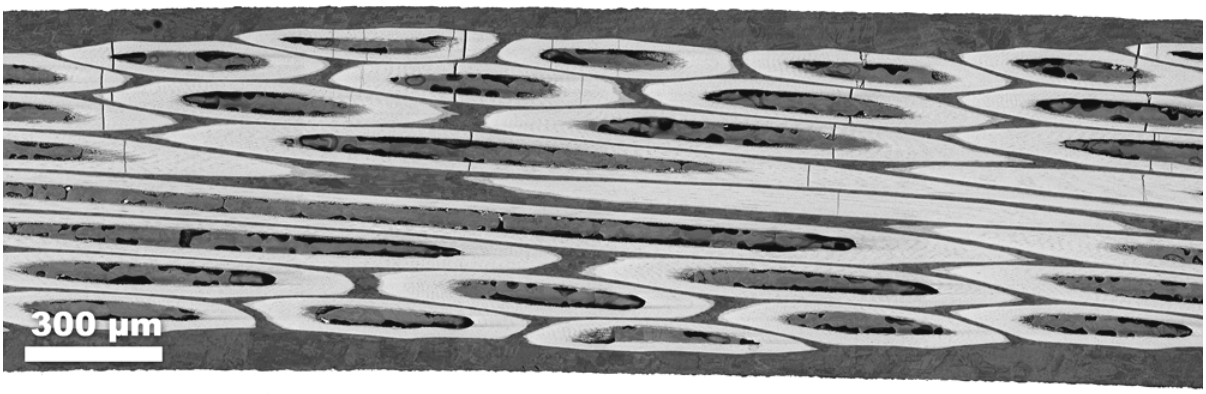

Figure 5.5. OST-3000 strand bent to 1.5% strain at 77 K. The fracture morphology consists of long, discrete chains of cracks that propagate across sub-bundles, from the tensile axis to the neutral axis. Significantly, no fracture of any kind is observed on the compressive side of the strand.

Figure 5.6. OST-2400 strand bent to 1.5% strain at 77 K. The fracture morphology is very similar to the OST-3000 strand, though the dominant cracks are spaced closer by about 50%. Here again, no fracture events are observed on the compressive side of the strand.

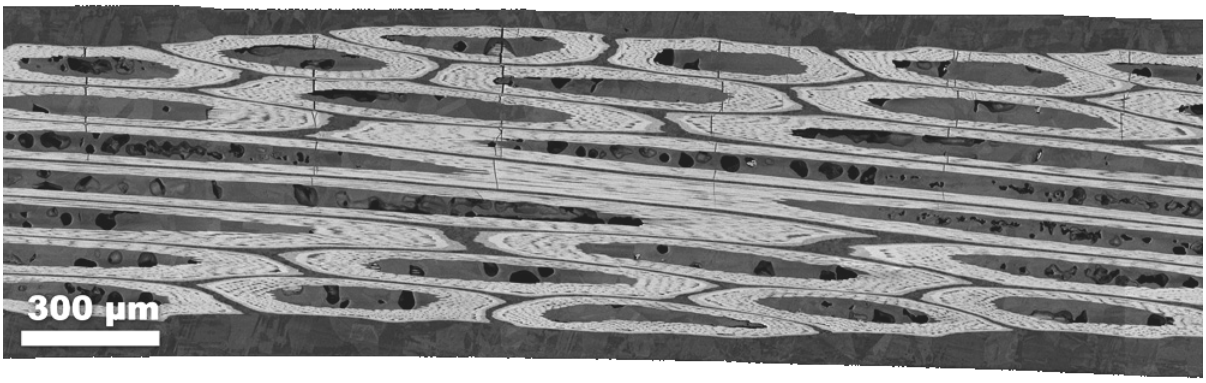

Figure 5.7. OST-1700 strand bent to 1.5% strain at 77 K. The fracture morphology is very similar to that observed in the OST-2400 strand.

generally ineffective at stopping crack growth, although there are a few hairline cracks that seem to be blunted by this ductile phase. The Nb barrier (recalling that in the HEP strand each sub-bundle is individually wrapped with a diffusion barrier) is shown to be the nucleation site for nearly every crack, but it is also shown to effectively arrest crack growth. Despite this, however, the crack apparently creates a stress concentration significant enough to introduce fracture in the adjacent sub-bundle, so the net result is a highly collective crack pattern. This behavior stands in stark contrast to that observed in the ITER-style strands, where the small (3 – 6 μm diameter) filaments tend to crack individually unless directly mechanically coupled to neighboring filaments.

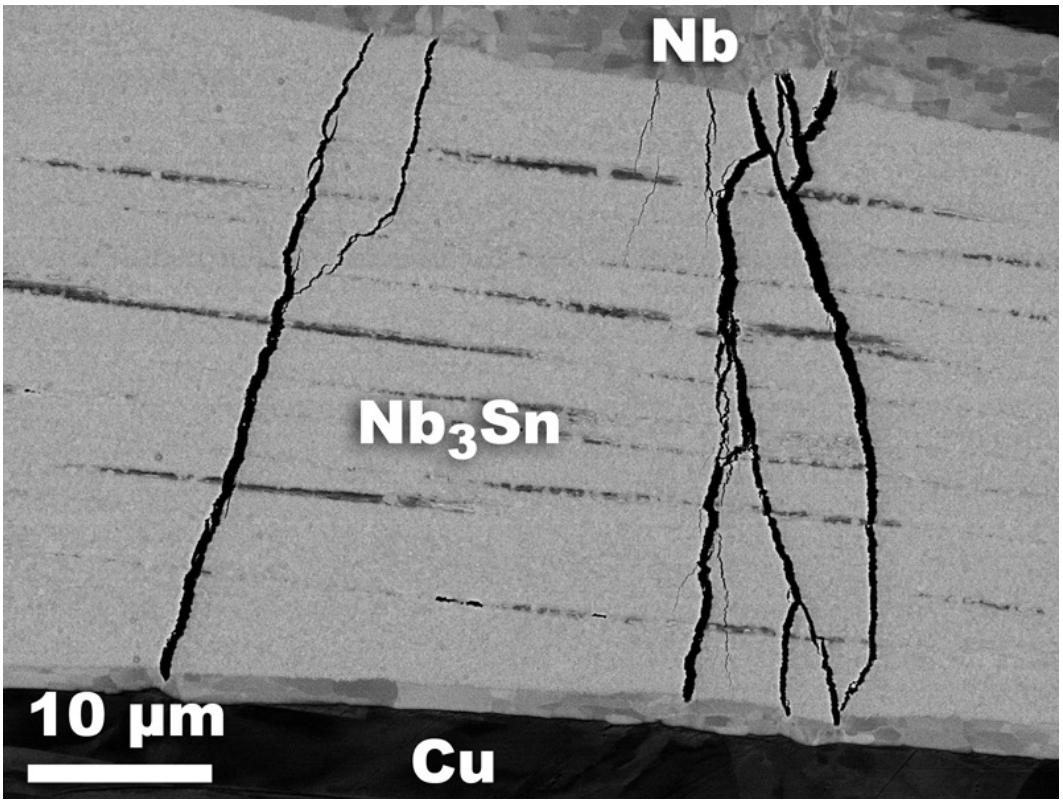

Figure 5.8. Single sub-bundle view of fracture events in OST-3000 strand. Cracks nucleate from the Nb-Nb_3Sn interface and propagate across the brittle Nb_3Sn layer, but are subsequently arrested by the more ductile barrier Nb. However, this arresting of cracks does not prevent the crack from altering the stress state in the neighboring sub-bundle enough to continue propagating.

5.1.3 Bend strain at 1.0% and 0.5%

At 0.5% nominal bend strain, all samples were essentially crack-free. At 1.0%, there was some nominal cracking in the ITER strands, but not enough to generate useful statistics in most cases (see a complete tabulation in table 5.2, below). This is not surprising in light of the 1.5% bend strain results, which indicated that the onset of cracking for most samples is near 0.7%, which is the maximum value obtained in filaments near the diffusion barrier in wires bent to 1.0% overall bend strain. The Hitachi results from 1.0% bend strain are presented in figure 5.9, and while the number of data points available is low, there is a statistically significant (95% confidence interval) increase in crack density above 0.5% bend strain, which is very similar to the

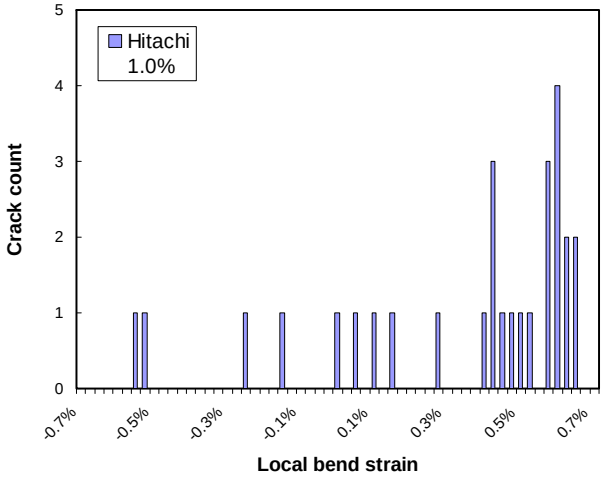

Figure 5.9. Fracture distribution of Hitachi strand at 1.0% nominal bend strain. Although there are far fewer cracks in this sample than in the 1.5% sample, the onset of statistically-significant cracking seems to occur at a similar strain value (around 0.6%).

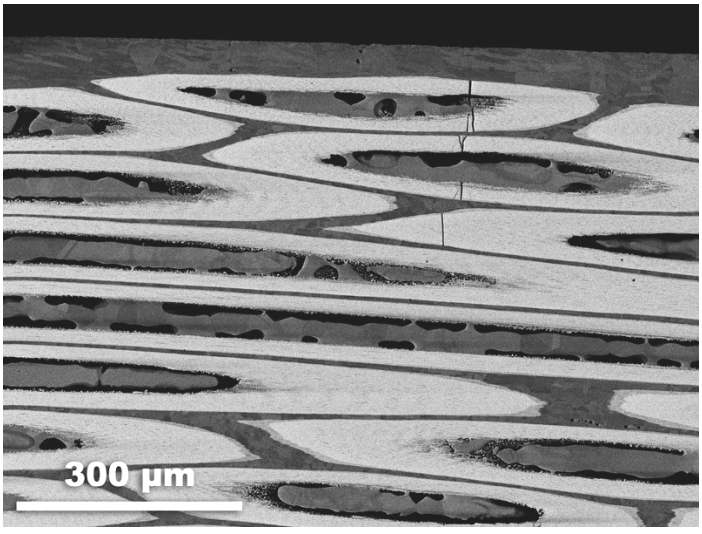

Figure 5.10. Fracture in OST-3000 after bending to 1.0% strain at 77 K. The fracture events are not a dense, but they still propagate to near the neutral axis.

behavior observed in the 1.5% bend strain samples.

In the HEP strands, some cracking can still be seen at 1.0% bend strain (figure 5.10). This is presumably due to the fact that the much larger agglomerated sub-bundles allow larger stress concentrations or initial flaws to generate cracks, and also because the sub-bundles are located nearer the wire circumference (and therefore see larger peak bending strain) than the sub-bundles in the ITER strand.

5.2 Heat treatment effect on cracking – ITER and HEP strands

The effect of heat treatment on bend strain fracture was also examined in the four ITER candidate wires at 1.5% and one (OST-2400) HEP strand at 1.0% bend strain. The fracture distribution histograms are shown in figure 5.11. Mitsubishi and Hitachi were tested with mildly reduced Nb_3Sn layer thicknesses, while EAS and Oxford were tested with a more aggressive reduction in the heat treatment. The photomicrograph inset on each plot shows this reduction in heat treatment (the Nb_3Sn is the bright ring around the darker gray Nb core). For a comparison with the full heat treatment microstructure, refer to figures 4.3 – 4.6.

In all cases, the shortened heat treatment reduced the frequency of cracking. The EAS strand, in fact, had exactly one crack in the entire polished cross-section in this under-reacted condition. To properly understand the significance of this effect, however, the data need to be normalized to the volume fraction of Nb_3Sn available at each heat treatment condition. This is done in table 5.2, below, and the implications are noted in the subsequent discussion.

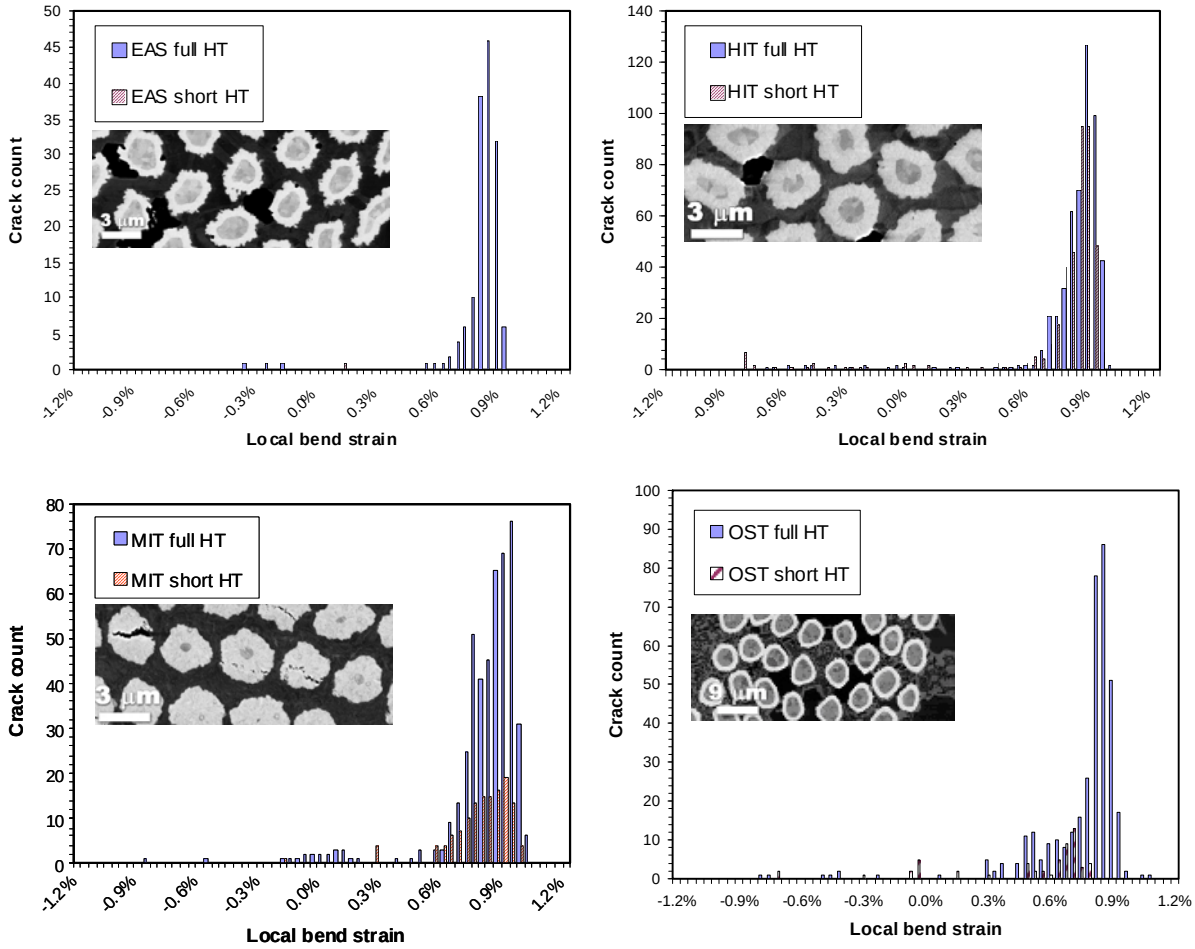

Figure 5.11. Distribution of fracture events as a function of bend strain for both full and short heat treatments.

For both Mitsubishi and Hitachi in the mild heat treatment conditions, the shape and onset of the fracture distribution curves track well with those of the full heat treatment curves. However, for the Mitsubishi strand the frequency of cracking is greatly reduced (table 5.2) despite only sacrificing a small filament A15 volume to enhanced volume of unreacted Nb cores.

For Oxford in the more aggressive heat treatment state, the crack density curve is shifted to lower strain values.

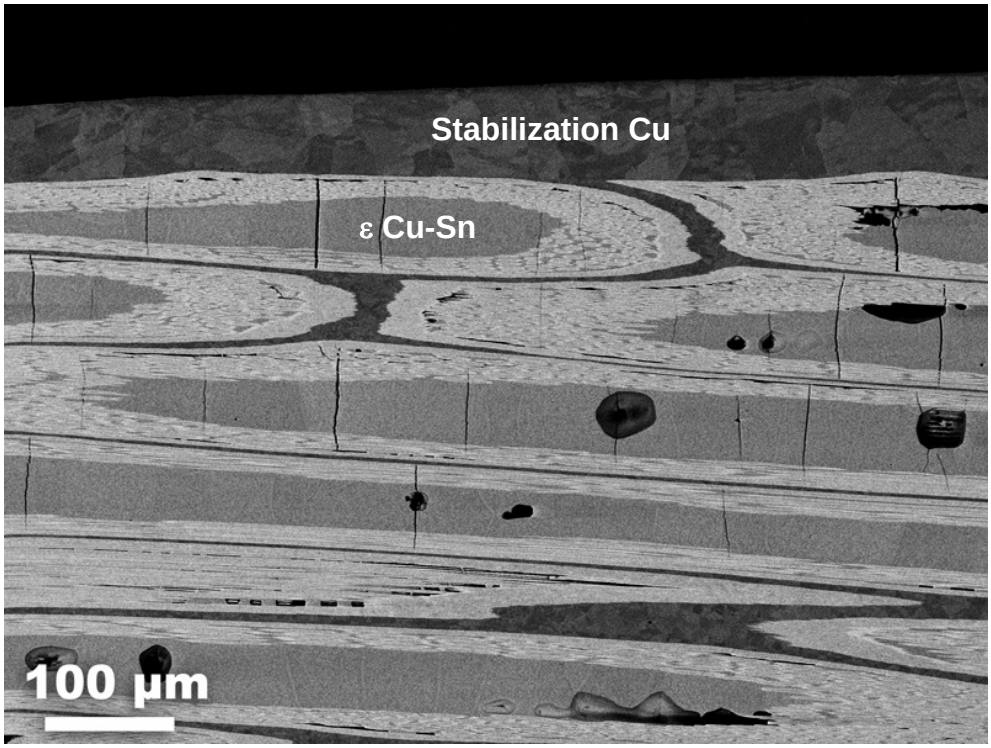

Figure 5.12. Longitudinal cross-section of OST-1700 strand after bend testing to 1.0% strain at 77 K with a reduced heat treatment. Here, the reaction is sufficiently short that the sub-bundle cores have significant residual Sn and ε Cu-Sn phase, which is brittle. As a result, the cracks propagate through the sub-bundle core rather than go around it. This is likely to enhance the overall crack density.

Under-reaction in the HEP strands produces a dramatically different and undesired result. As shown in figure 5.12, the reduced heat treatment leaves behind some brittle Cu(Sn) ε phase material, which cracks along with the Nb_3Sn filament. Thus, instead of arresting crack growth, the sub-bundle core now participates in the fracture. When compared to figure 5.10 (the OST-3000 strand at 1.0% bend strain) the increase in Nb_3Sn fracture density is clear. The implication, then, is that under-reaction in the HEP strands does not reduce the fracture propensity of the conductor. The filament pack agglomerates very early in the heat treatment process (see figures 4.10 – 4.12), so any under-reaction only serves to

store additional Sn in the matrix in the form of brittle ε-phase Cu(Sn) (and possibly other brittle Cu-Sn intermetallics), which in turn worsens the fracture propensity.

The effect of under-reaction on the ITER-style strands is less obvious, and requires some careful geometric normalization. This will be discussed in the following section (5.3).

5.3 Summary of bend testing results

Table 5.2 (next page) presents all the crack data accumulated from the 1.0% and 1.5% ITER bend strain samples. "Sampled area inside diffusion barrier" is the area that was revealed by polishing and imaged for crack location analysis. "Fraction of Nb_3Sn inside diffusion barrier" is the fraction of the total non-Cu area (excluding the diffusion barrier itself) consumed by Nb_3Sn for the specified reaction condition.

Three normalizations resulting in two outputs are performed to account for interpretive difficulties arising from the fact that (1) different areas are imaged in each strand, due to small differences in the length of the sample and the polished depth (2) different strands and heat treatments produce a different amount of Nb_3Sn, leading to an inherent difference in the probability of fracture, and (3) different strands have different filament counts, meaning that the relative importance of a crack is different in each strand.

5.3.1 Cracks/mm^2 of Nb_3Sn

This data column (second from the right in table 5.2) measures the crack density in the polished cross-section, normalized to the amount of Nb_3Sn available to participate in fracture. The result is computed by normalizing the raw crack count to (1) the area imaged and (2) the fraction of Nb_3Sn in the cross-section. This is necessary because we expect an

under-reacted sample to have fewer cracks solely on the basis that there is less Nb_3Sn in the system. The more interesting question is whether there is a cumulative effect – does a shorter heat treatment increase or decrease the probability of fracture, relative to the amount of Nb_3Sn in the cross-section? As shown in this column of table 5.2, three of the four strands bent to 1.5% (EAS, Mitsubishi, and Oxford) have behavior that unequivocally suggest that reducing the heat treatment does significantly reduce the probability of fracture. The Oxford strand, for example, demonstrates a reduction in crack density from 152 cracks/mm^2 to

Table 5.2. Complete fracture results for 1.0% and 1.5% bend strain

Bend radius (%)	Strand	HT	Crack count	Sampled area (mm^2) inside diffusion barrier	Fraction of Nb_3Sn inside diffusion barrier	Cracks/mm^2 of Nb_3Sn	Cracks/filament
1.0	EAS	Full	4	8.36	0.319	1.5	0.0%
1.0	Hitachi	Full	28	8.16	0.369	9.3	0.3%
1.0	Mitsubishi	Full	7	7.48	0.325	2.9	0.1%
1.0	Oxford	Full	10	7.96	0.401	3.1	0.3%
1.5	EAS	Short	1	5.31	0.198	0.9	0.0%
1.5	EAS	Full	150	6.83	0.319	68.9	1.8%
1.5	Hitachi	Short	410	5.39	0.309	246.0	3.7%
1.5	Hitachi	Full	514	6.85	0.369	203.3	4.6%
1.5	Mitsubishi	Short	131	7.62	0.307	56.0	1.0%
1.5	Mitsubishi	Full	463	7.24	0.325	196.8	3.4%
1.5	Oxford	Short	56	4.70	0.201	59.4	1.8%
1.5	Oxford	Full	374	6.14	0.401	151.8	12.1%

59 cracks/mm^2 with reduced heat treatment. That is, even when the reduced area of A15 is taken into consideration, a representative volume element is less likely to fracture by a factor of ~3 (Oxford) or ~4 (Mitsubishi). One strand (Hitachi) actually suggests the opposite – that after the normalization for reduced A15 area, the probability of finding a crack actually increases slightly for reduced heat treatment. While there is no experimentally obvious explanation for this behavior, it should be noted that the Hitachi strand is the only strand with a significant unreacted filament core in the "full heat treatment" condition. Assuming these cores help to toughen the filament (as the results from the other three strands suggest), then the Hitachi strand already experiences this benefit at full heat treatment, so further fracture reduction is unlikely with reduced heat treatment.

5.3.2 Cracks/filament

The method of crack density normalization described above has one serious shortcoming in that it does not account for the variable number of filaments. A low crack density (relative the wire cross-section) is not beneficial if there are very few filaments to carry the electric current. The last column in table 5.2, entitled "cracks/filament", normalizes the number of cracks observed to the number of filaments in the wire. Or, expressed differently, the value reported here is the percentage of filaments cracked, if we assume that each filament in the polished cross-section only cracks once. This is not unreasonable since the twisted filament stack ensures that no single filament is in the area of observation for more than a few tens of microns, and the observed length of strand (about 10 mm) is not longer than the twist pitch of the strand (10 – 20 mm).

This analysis shows very dramatically the effect of fewer, larger filaments on the strain sensitivity of the strand. The Oxford stand, at 1.5% bend strain and full heat treatment, has fractured over 12% of the filament pack, almost three times the next-closest strand. This observation has an important design implication that relates to strand fabricability and cost. Fewer filaments in the strand allow for simpler billet assembly and possibly easier wire drawing, but this choice carries the implication that each filament must carry a higher percentage of the electric current during magnet operation. Thus, each crack that forms is more detrimental to the electrical performance of the strand.

5.3.3 Summary remarks

The bend testing method we have developed provides a simple, consistent method for comparing the relative fracture propensity of strands with disparate designs. In our metallographic investigation, filament size and filament agglomeration are clearly demonstrated as important variables for fracture propensity. The three strands with similar filament size (EAS, Hitachi, and Mitsubishi) all display an onset of fracture around 0.7% bend strain, while the Oxford strand (larger filaments) displays an onset of fracture near 0.4%. The internal tin ITER strands (which have more filament agglomeration than the well-separated bronze strands) exhibit more collective cracking than the bronze strands, and this collective nature can be directly correlated to the number of agglomerated filament rows in the sub-bundle. The HEP strands, which have entirely agglomerated sub-bundles, show highly collective (and highly catastrophic) fracture patterns. The Cu fraction in the interfilamentary region (which is proportional to the J_c of the strand) does not significantly affect this fracture behavior, even when the J_c is varied from 1700 A/mm^2 to 3000 A/mm^2.

Additionally, the very large cracks produced by the agglomerated filament sub-bundles are shown to produce a significant stress concentration which causes the filament pack in neighboring sub-bundles to fracture. This occurs on the entire tensile side of the strand.

A reduction in the heat treatment does decrease significantly the probability of fracture for ITER strands, even when normalized to the reduced A15 volume. To ascertain the utility of this approach for wire toughening, critical current tests should be carried out on the strands with reduced heat treatment, to determine the amount of critical current reduction that accompanies this lower crack density. As ITER progresses towards a common heat treatment for all strand vendors, the impact of this change on the fracture propensity needs to be understood.

The effect of a strand design with fewer filaments is shown to be detrimental on a normalized basis. Even though this design (Oxford) does not have the maximum number of cracks observed, the percentage of filaments cracked is higher by a factor of 3 or 4 than for any other strand design.

5.4 Fracture propensity under uniaxial strain

Metallographic examinations from tests such as pure bending are useful because they simulate the deformation conditions of a CIC conductor. However, they also introduce very complex strain states that make determination of the onset of cracking difficult. To study fracture in a more controlled setting, a set of samples from EAS and Oxford were pulled in uniaxial tension at 4.2K at the University of Twente and then evaluated metallographically.

5.4.1 EAS uniaxial samples

EAS Nb_3Sn wires were strained uniaxially in 0.1% increments from 0.0% to 0.7% strain at 4.2 K. Upon metallographic examination, no strand at any strain value showed any fracture behavior whatsoever. Two representative photomicrographs from 0.0% and 0.7% strain, respectively, are shown in figure 5.13. Aside from being a general endorsement of the EAS strand architecture, this result (coupled with the Oxford results in section 5.4.2 below) demonstrates an important point. So far, we have been examining strand architecture largely in terms of fracture *propagation* – the effect of filament size and spacing on the ability of a crack to jump from one filament to the next. However, this shows that filament architecture also plays a role in fracture *initiation*. That is, these smaller, better-distributed filaments are fundamentally more resistant to the formation of cracks, not just the propagation of cracks across the interfilamentary Cu. This concept will be further developed in chapter 8.

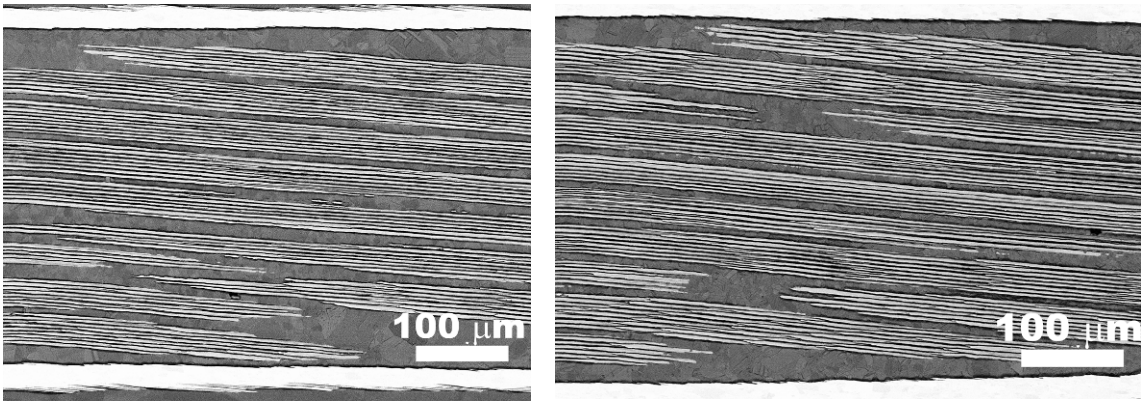

Figure 5.13. Longitudinal cross-section of EAS Nb_3Sn strand after 0.0% bend strain (left) and 0.7% bend strain (right) at 4.2 K. The sample was essentially crack-free at all bend strains measured (up to 0.7%).

5.4.2 Oxford tensile samples

Oxford Nb_3Sn wires were strained in 0.1% increments from 0.0% to 0.7% strain at 4.2 K. Representative photomicrographs are shown in figure 5.14 for strain values of 0.0%, 0.3%, 0.5%, and 0.7%. A background crack density of <1 crack/mm of sample length was observed in the 0.0% - 0.4% samples. Beginning with the 0.5% sample, a non-trivial density of fracture events was observed, and the crack density with tensile strain is plotted in figure 5.15. Please note that this is only the fracture density as normalized to the length of sample observed.

Two significant improvements, however, can be made to this normalization. First, the

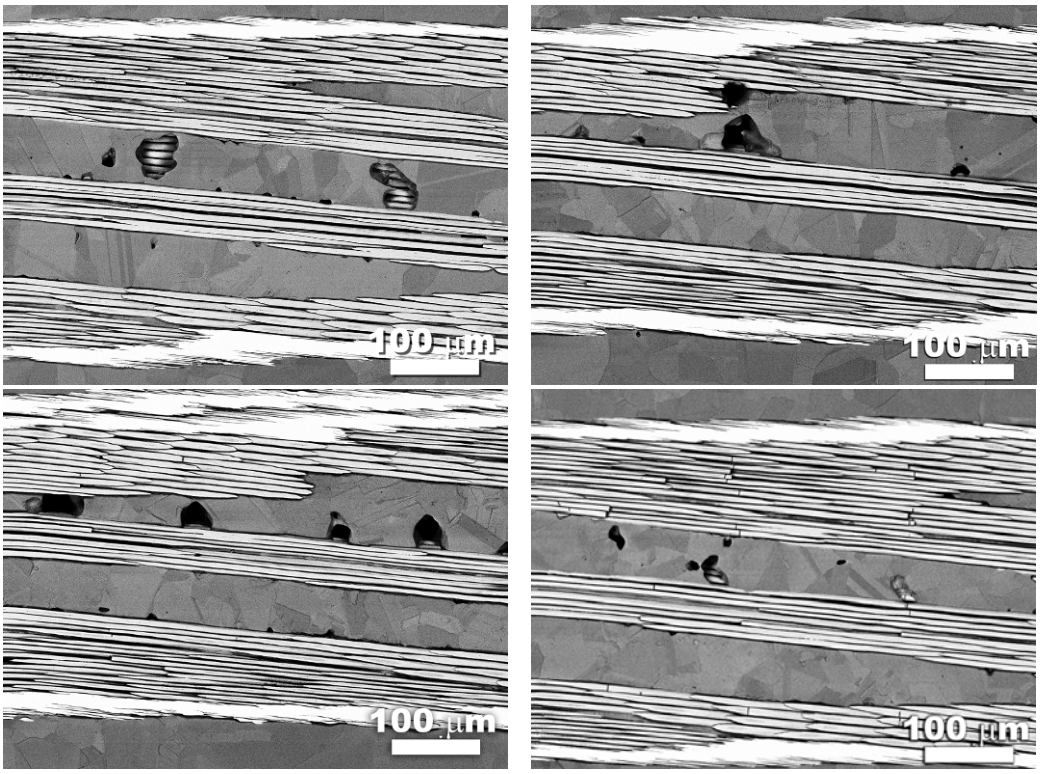

Figure 5.14. Scanning electron microscopy (backscatter) photomicrograph of Oxford strand after uniaxial tension testing at (a) 0.0%, (b) 0.3%, (c) 0.5%, and (d) 0.7% strain. The onset of fracture occurs between 0.4% and 0.5%.

observed area can be normalized to the volume of the wire within the diffusion barrier, allowing for an estimate of the true distribution of cracks within the volume. Second, there appears to be a statistically significant number of "broken ends" in the 0.7% sample (see figures 5.16 and 5.17). These are filaments that truncate sharply as they twist out of the imaging plane, and thus could be evidence of uncounted cracks. The number of broken ends as a function of bend strain remains fairly constant through 0.6% strain (see figure 5.16), but ticks up sharply at 0.7%. These additional broken ends can reasonably be assumed to be due to real fracture events, thereby leading to an undercounting of cracks. With these two adjustments, the distribution is substantially exponential in nature as expected if a Weibull-type distribution exists.

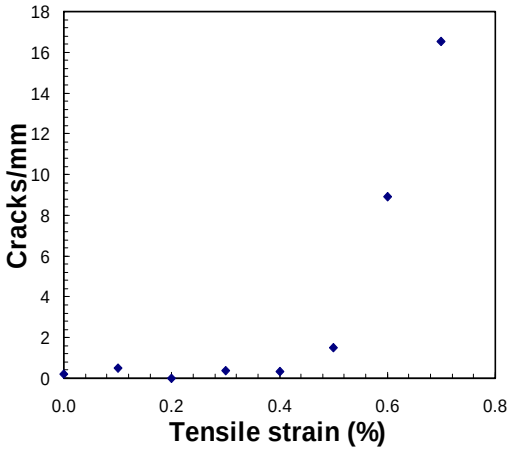

Figure 5.15. Crack density in Oxford uniaxial tension samples after normalization to wire length imaged.

Additionally, we can compare the onset of fracture as measured by metallography

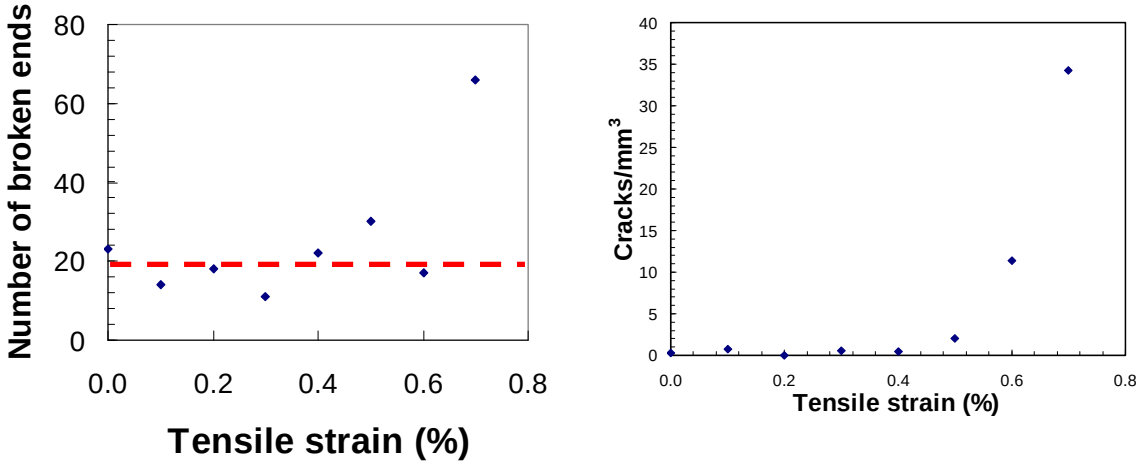

Figure 5.16. Broken ends (left) and renormalization of the crack density (right) for Oxford uniaxial tension samples. The normalization takes into account both the extra broken ends at 0.7% strain and an extrapolation of the observed cracks to the entire sample volume.

with that measured electromagnetically. Using the recent NIST Walters spring I_c data available for this Oxford strand (figure 5.18), we see an electromagnetic onset of irreversibility around 0.47% strain. After correcting for the fact that the NIST data was acquired on a strand that was soldered to a Cu-Be alloy substrate (the Walters spring), while our data was acquired free-standing, we can estimate that the I_c data predicts an onset of irreversibility around 0.35% to 0.40% in the free-standing tensile samples. This is in reasonable agreement with our measured data.

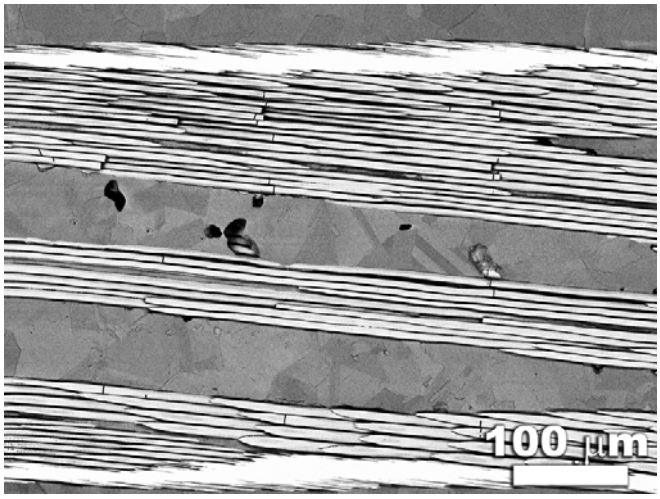

Figure 5.17. Magnified view of the Oxford 0.7% uniaxial tension sample. Note the semi-correlated nature of the fracture events and the presence of cleanly broken filaments.

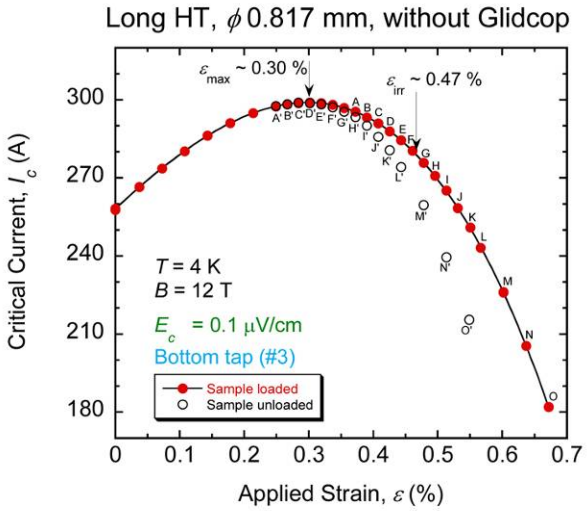

Figure 5.18. Irreversible strain (via I_c) measurements on a CuBe Walters spring [94]. The irreversible strain value of 0.47% is in reasonable agreement with our metallographic technique, though more sensitive by about 0.1% strain. Image courtesy Najib Cheggour, NIST.

5.5 Summary of uniaxial test results

The EAS samples deformed in uniaxial tension are almost crack-free at strain values ranging from 0.0% to 0.7%. This both validates the polishing technique and demonstrates the inherent mechanical toughness advantage of small, well-separated filaments. The Oxford samples deformed in uniaxial tension, by contrast, begin to fracture between 0.4% and 0.5% strain. This agrees reasonably (to within 0.1%) of the irreversible strain limit observed by I_c measurement on the same strand using a Walters spring. The earlier onset of fracture in the Oxford samples is also consistent with the fracture morphology observed in the bend test samples.

Because the uniaxial test produces a much simpler stress field than does bend testing, we can with greater confidence normalize the observed cracks to the entire wire volume, thus estimating the true density of cracks in the strand for a given strain state. This is highly useful for comparing to I_c data, as it provides the first empirical link between observed mechanical degradation and observed electrical degradation.

CHAPTER 6 – FRACTURE AND CRITICAL CURRENT DENSITY

With a combination of quantitative metallography, bend testing, and uniaxial testing, we have specified the effect of architectural parameters such as filament size and spacing on crack nucleation and propagation in Nb_3Sn strands. Because the ultimate goal is to understand the role of filament fracture in critical current degradation in real magnet conductors, the next logical step is to relate filament fracture to I_c reduction. To do this, we collaborated with the University of Twente, where electromagnetic characterization as a function of bend strain is possible on the TARSIS apparatus.

6.1 TARSIS overview and procedure

The TARSIS strain rig is a unique device invented at the University of Twente (Netherlands) that allows for the simultaneous mechanical deformation and critical current testing of Nb_3Sn superconducting strands. In this test, a wire is wound around the circumference of a barrel, heat-treated in place, and then loaded mechanically in a direction perpendicular to the plane of the circular wire path around the barrel. TARSIS can be equipped with two styles of rigs – the periodic bending probe (figure 6.1a) or the crossing-strands (x-strands) probe (figure 6.1b). The periodic bending probe uses a series of protruding bulges, arranged in a periodic fashion around the circumference of a barrel, to apply a combination of tension and periodic bending to the superconducting sample. The

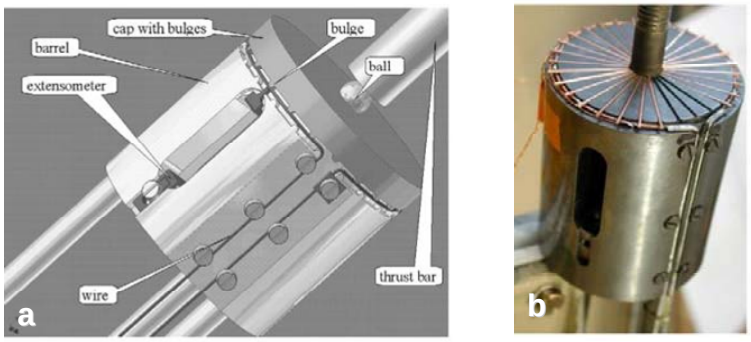

Figure 6.1. The TARSIS bending (left) and crossing strands (right) probes, adapted from [93]. The bending probe provides a periodic distribution of tensile and compressive bending coupled with uniaxial tension, and the crossing strands probe provides periodic compression (pinching). Both rigs allow for full electromagnetic characterization of superconducting samples at temperatures down to 4.2 K and magnetic fields up to 12 T

crossing-strands probe uses straight sections of strand to provide periodic compressive strain to the sample. In the sample set investigated here, the bending probe had a wavelength of 5 mm, and the crossing-strands probe had a wavelength of 4.7 mm. A more complete description of the technique and some representative results may be found here [93].

Electromagnetically, the samples subjected to bending and tension in the bending probe demonstrated much more significant degradation than those in the x-strands probe, and so the bending probe will be the focus of our examination here.

Each sample was extracted from the probe after full electromagnetic characterization, and mounted in the plane perpendicular to the loading direction. This allows for purely tensile (at the full wavelength position) and purely compressive (at the half wavelength position) regions to be imaged for damage characterization. This provides a useful check on the metallographic polishing procedure, since the damage should occur periodically with the bending wavelength.

6.2 TARSIS I_c data

The normalized I_c data from the TARSIS 5 mm bend rig is shown in figure 6.2 as a function of peak bending strain. Because the original intent of the experiment was to assess the strain sensitivity of different strands, each sample was not necessarily tested to the same peak bending strain or I_c degradation value. Table 6.1 summarizes the final bending strain and $I_c/I_{c,0}$ experienced by each sample prior to metallographic preparation. The interpretation of these data is presented with the metallographic analysis that appears in section 6.3.

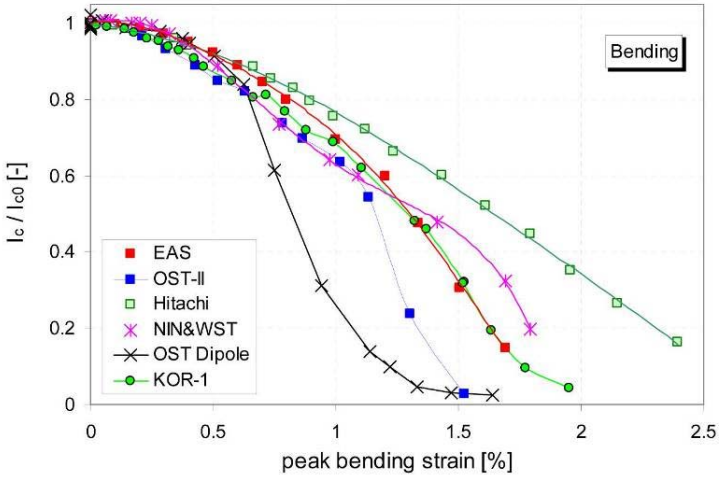

Figure 6.2. The degradation of critical current as a function of peak bending strain measured in the TARSIS experiment. The peak bending strain is relative to the entire wire radius. Data is courtesy of Arend Nijhuis, University of Twente.

6.3 TARSIS metallography

Figures 6.3 – 6.8 show representative microstructures (FESEM-BEI) of the filament damage that occurs at the tensile peak bending position for each of the six wires imaged. Three of these six strands are ITER candidate strands

Table 6.1. Experimental condition of TARSIS samples for metallographic examination.

Sample	Max peak bending strain (%)	Final $I_c/I_{c,0}$
EAS	1.7	0.15
Hitachi	2.4	0.17
Oxford	1.5	0.03
NiN & WST	1.8	0.20
KOR	2.0	0.04
Oxford dipole	1.6	0.03

characterized in the remainder of this report (EAS, Hitachi, and Oxford), two are ITER candidate strands not characterized in this report (NiN & WST, KOR), and one is a high-J_c high energy physics strand (OST-2400) that is provided for comparison purposes. A description of the fracture field is provided in the figure caption of each figure, and a summary is provided following the image set.

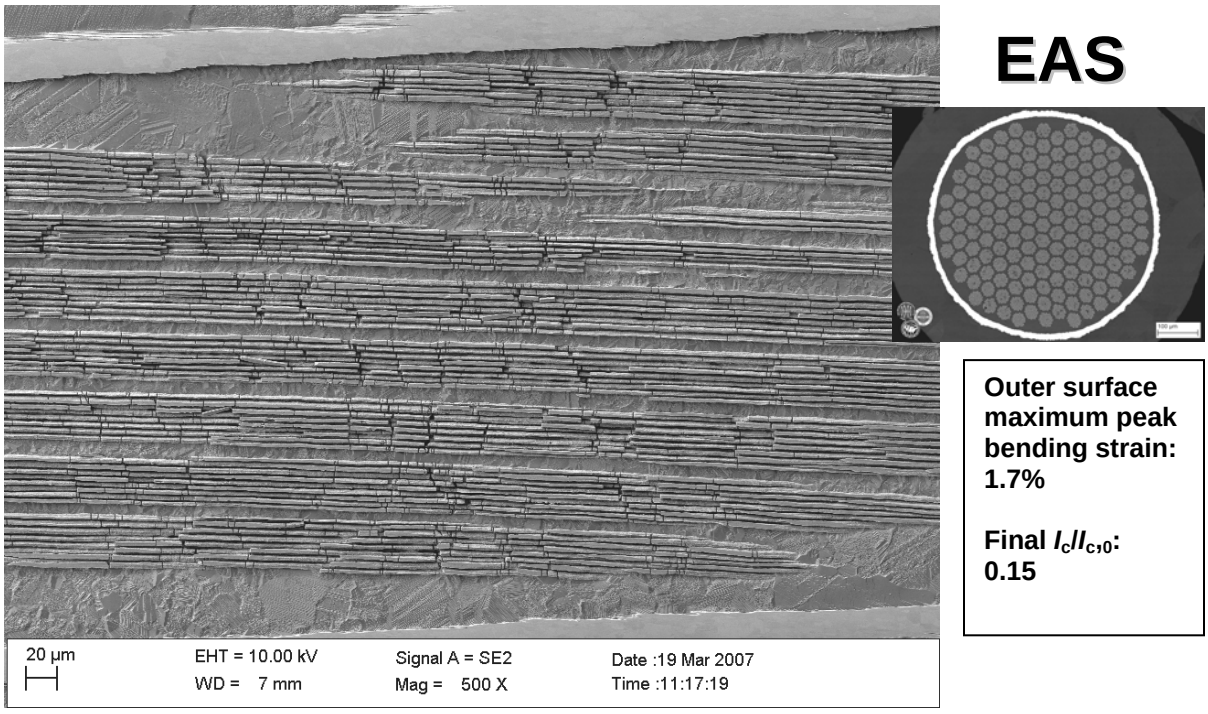

Figure 6.3. EAS 5 mm bend fracture field after TARSIS testing. The spatial extent of the fracture field is ~200 µm. The image shows a mixture of correlated and non-correlated fracture events.

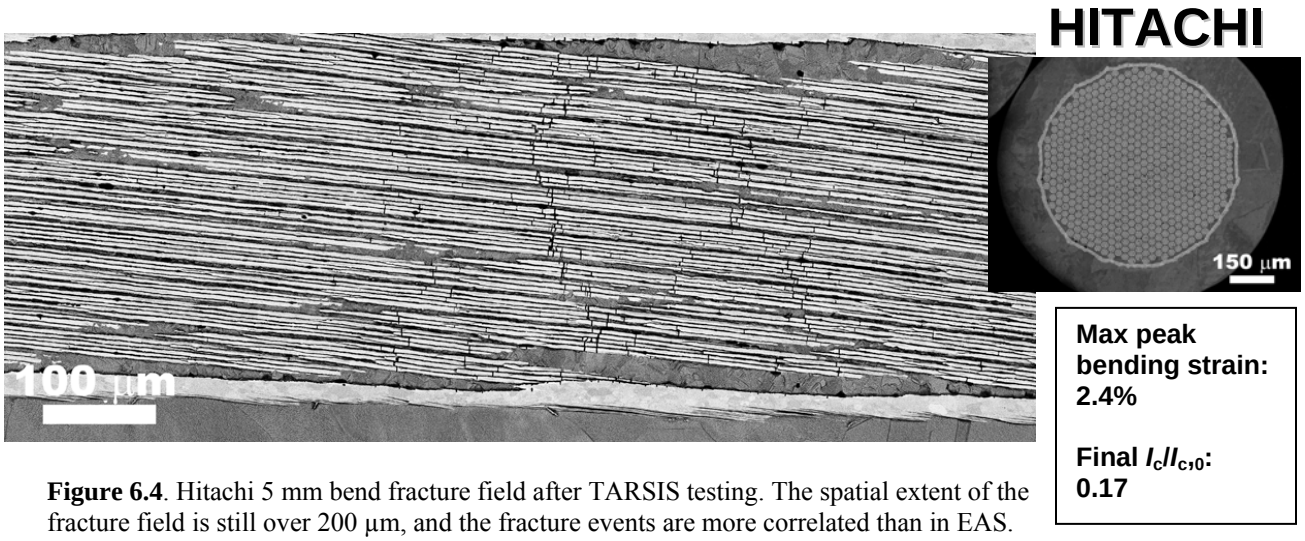

Figure 6.4. Hitachi 5 mm bend fracture field after TARSIS testing. The spatial extent of the fracture field is still over 200 μm, and the fracture events are more correlated than in EAS.

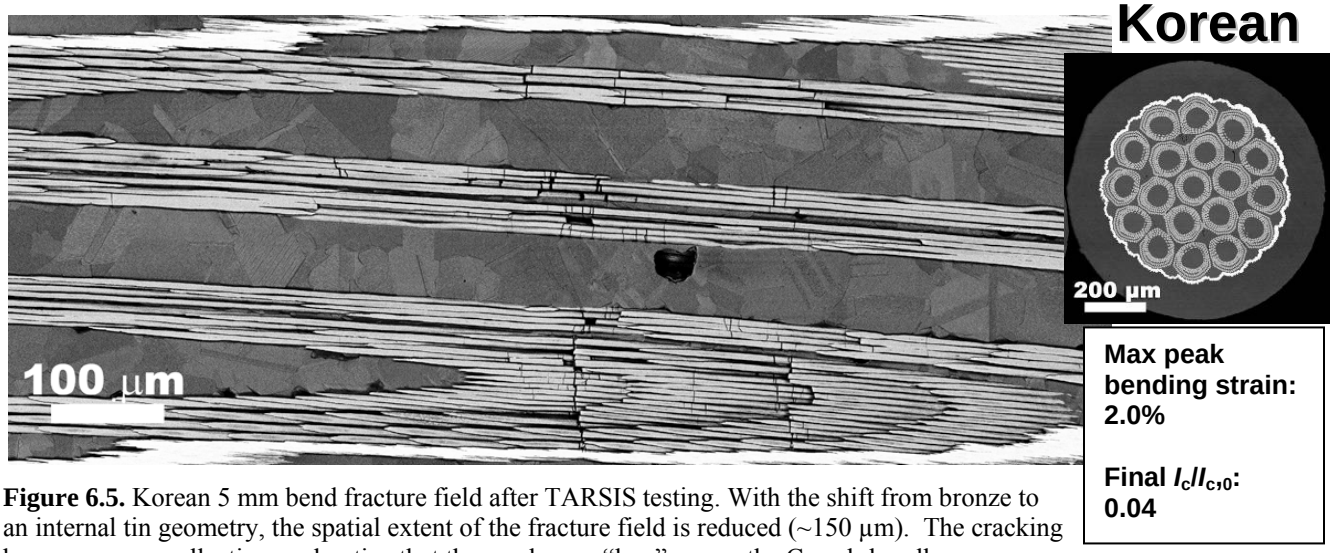

Figure 6.5. Korean 5 mm bend fracture field after TARSIS testing. With the shift from bronze to an internal tin geometry, the spatial extent of the fracture field is reduced (~150 μm). The cracking becomes more collective, and notice that the cracks can "hop" across the Cu sub-bundle cores, indicating that fracture is occurring around the Nb_3Sn annulus of the sub-bundle.

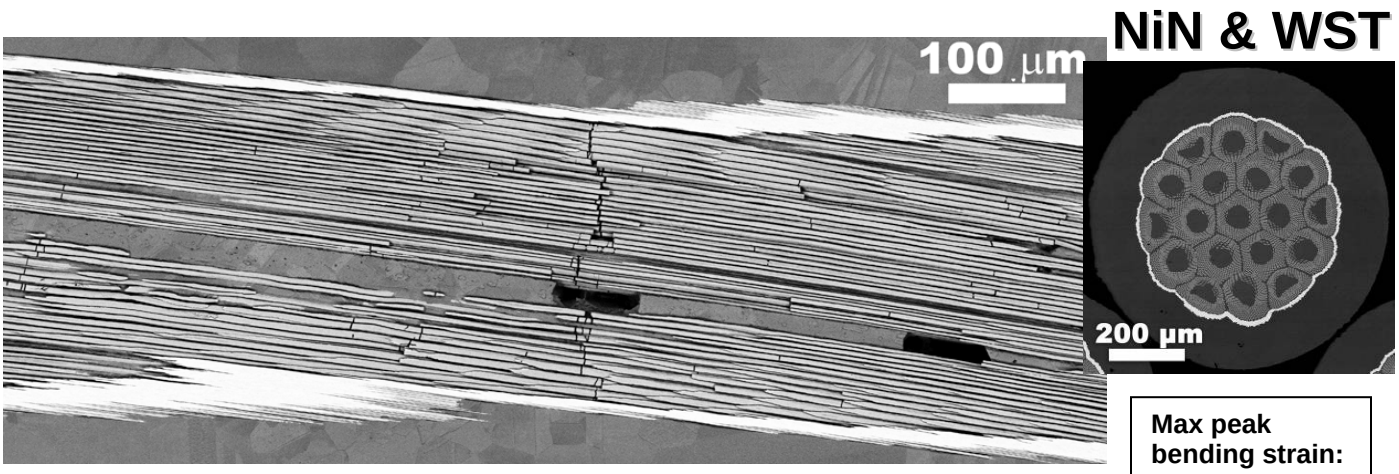

Figure 6.6. NiN & WST 5 mm bend fracture field after TARSIS testing. The damage region is heavily concentrated in one central crack feature, although some additional damage is visible up to 300 μm from the dominant crack.

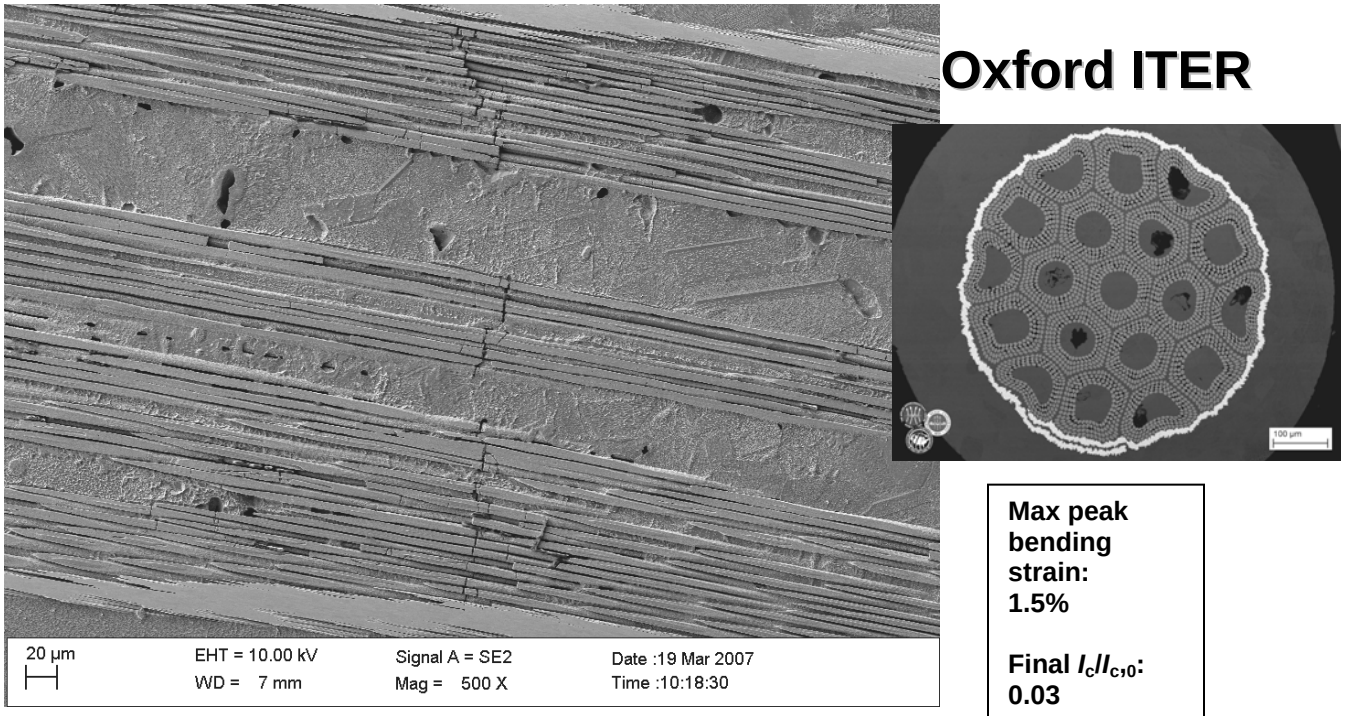

Figure 6.7. Oxford ITER 5 mm bend fracture field after TARSIS testing. Here, the fracture is clearly centered around a central crack, with almost no secondary damage whatsoever.

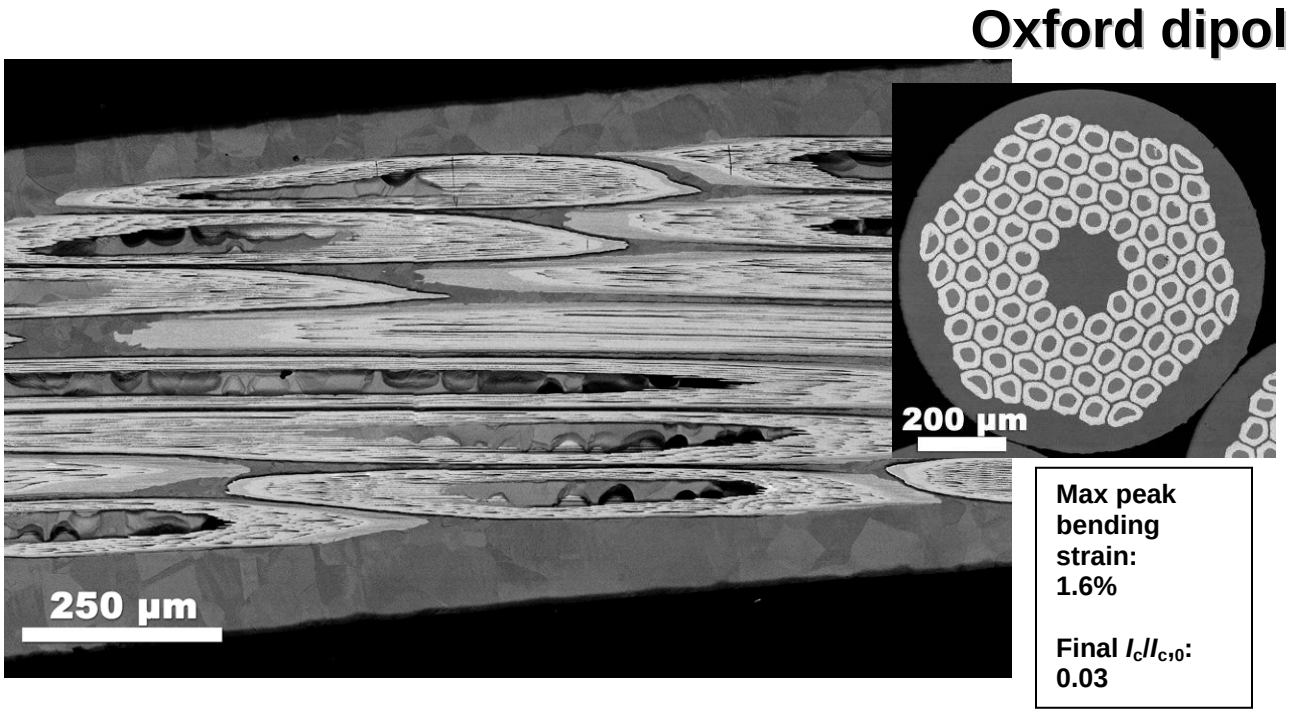

Figure 6.8. Oxford dipole 5 mm bend fracture field after TARSIS testing. The fracture events propagate immediately across each sub-bundle, but then are arrested by the sub-bundle Nb diffusion barrier.

The metallographic examination of TARSIS strands has three significant drawbacks that should be acknowledged before drawing conclusions about the fracture state of these conductors:

1. The conductors were each deformed to different maximum peak bending strains, making direct, quantitative comparison amongst different strands difficult.
2. Since the polishing procedure reveals planes perpendicular to the deformation direction, a different true peak bending strain can be imaged at different polishing depths. This is not necessarily problematic (indeed it can allow for precise selection

of the desired polishing depth), but it can make comparison difficult if different strands are imaged at different polishing depths.

3. The highly localized nature of the fracture in the TARSIS experiment makes the accumulation of useful statistics difficult.

Despite these challenges, imaging of TARSIS strands is highly useful because TARSIS more closely simulates the deformation conditions that occur at strand crossover in a CIC conductor than any other single-strand $I_c(\varepsilon)$ test available. As such, TARSIS gives a clear picture of the dominant fracture mechanism present in each candidate strand, and these mechanisms can be compared qualitatively from strand to strand.

Examining figures 6.3 – 6.8, the clearest trend is the progression from a distributed fracture mode (EAS, with small and well-separated filaments) to a highly collective fracture mode (Oxford ITER and OST-2400, with larger and more agglomerated filaments). This correlates reasonably with the strain sensitivity shown in figure 6.2 previously, e.g. the strands with more collective fracture events tend to degrade faster than those with more distributed, individual fracture events. This collective/individual fracture behavior also correlates reasonably with the extent of filament agglomeration, although we did not have access to the unreacted strand for several samples (NiN & WST, KOR), which would have permitted a proper analysis of this variable. Nevertheless, the trend is clear: by 1.5% bend strain, for example, the OST-ITER and OST-2400 strands (which have the highest degree of filament agglomeration) have both degraded below 5% of their initial I_c value, while no other strand is below 30% I_c at that strain value.

The Hitachi strand demonstrates the least strain sensitivity of any sample, despite the fact that its fracture behavior is more collective than the EAS sample. While we can not provide a definitive explanation for this behavior, it is interesting to note that the Hitachi strand is the only one with a significant amount of unreacted Nb left in the filament cores after reaction. One possible mechanism for maintaining good strain sensitivity, then, is that the very good bonding between the unreacted Nb and the Nb_3Sn helps to prevent cracks from widening after forming, which could in turn mitigate the effect on I_c.

The OST-2400 strand represents an extreme case of strain sensitivity in I_c testing, and indeed demonstrates very highly collective fracture behavior, with a single crack propagating across an entire sub-bundle in every case. However, despite this strongly brittle behavior, it is interesting to note that the presence of a distributed Nb barrier seems to be effective in arresting the crack growth.

6.4 Deep etching of TARSIS samples

As part of our TARSIS investigation, we developed a deep etching technique to reveal the three-dimensional nature of the fracture behavior. This technique involves immersing the sample in a 50 vol.% solution of HNO_3 in H_2O for 40 minutes, with one intermediate water rinse at 20 minutes. The following is a summary of the key results, with representative results shown in figures 6.9 and 6.10.

For bronze strands, which have well-separated filaments, the etch is effective at removing the interfilamentary Cu and thereby mechanically isolating the filaments from each other. This means that filaments with cracks are now mechanically unsupported, and so they

fall away, revealing the distribution of the fracture events through the wire. This is shown in figure 17a and 17b for the EAS and Hitachi strand, respectively.

For internal Sn strands, the deep etch is not an effective tool for revealing crack location, since the filament agglomeration allows filaments to mutually support each other mechanically, even after the interfilamentary Cu is removed. This is shown in figure 6.9c and 6.9d for Oxford ITER and OST-2400 strand, respectively.

The removal of the Cu also allowed a very interesting collective filament redistribution. As shown in figure 6.9a, the sub-bundles tend to organize into groups of 3 – 10 after Cu removal. This effect was not seen in virgin (heat treated but not mechanically

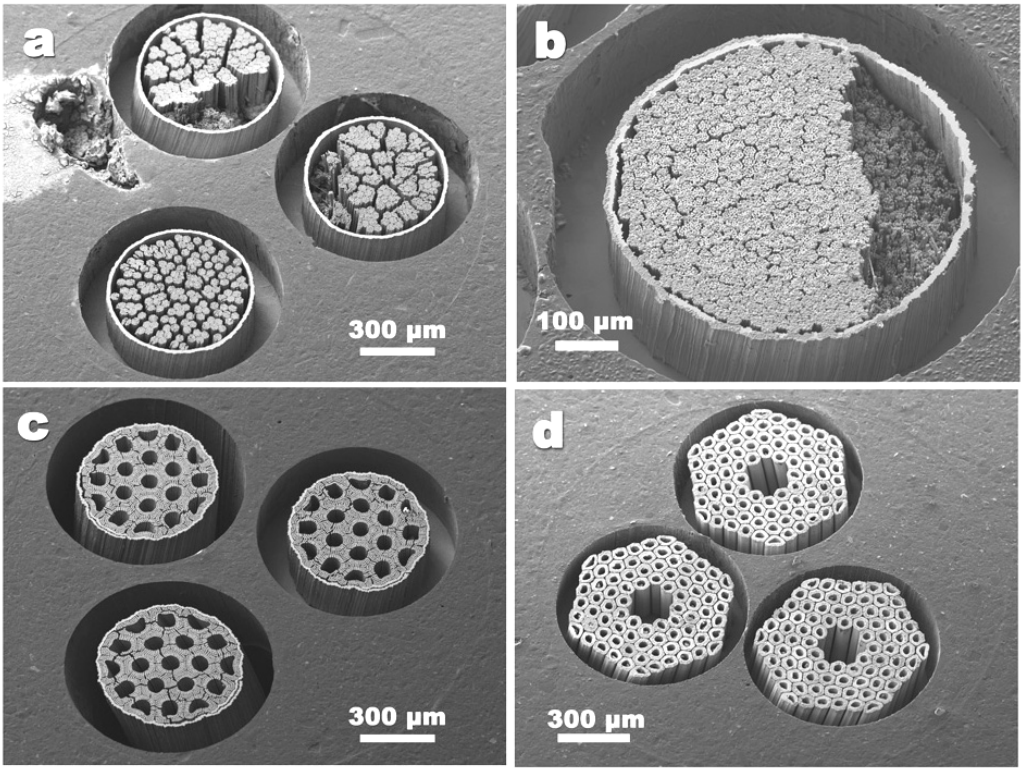

Figure 6.9. Examples of deep Cu etching performed on (a) EAS, (b) Hitachi, (c) Oxford ITER, and (d) Oxford OST-2400 strand, all after TARSIS testing. Note the technique is effective at revealing fracture events in the bronze-processed strand, but less effective at doing the same in internal-tin strands.

tested) samples that were subjected to a deep etch. Although more subtle, this effect is also noticeable in the Oxford strand (figure 6.9c), manifesting itself as "splits" in the sub-bundle packs. This result was also not observed in virgin strands.

The deep etch technique can also help reveal the extent to which fracture is collective or individual. For example, the EAS strand (figure 6.10a, 6.10c) tended to fracture in groups of 10 – 40 filaments, while the Hitachi strand (figure 6.9b) tended to fracture more uniformly, consistent with the longitudinal metallographic images shown previously (figures 6.3 and 6.4).

Finally, the deep etch technique can provide information about filament variability due to fabrication or heat treatment issues. For example, the Korean strand (figure 6.10b)

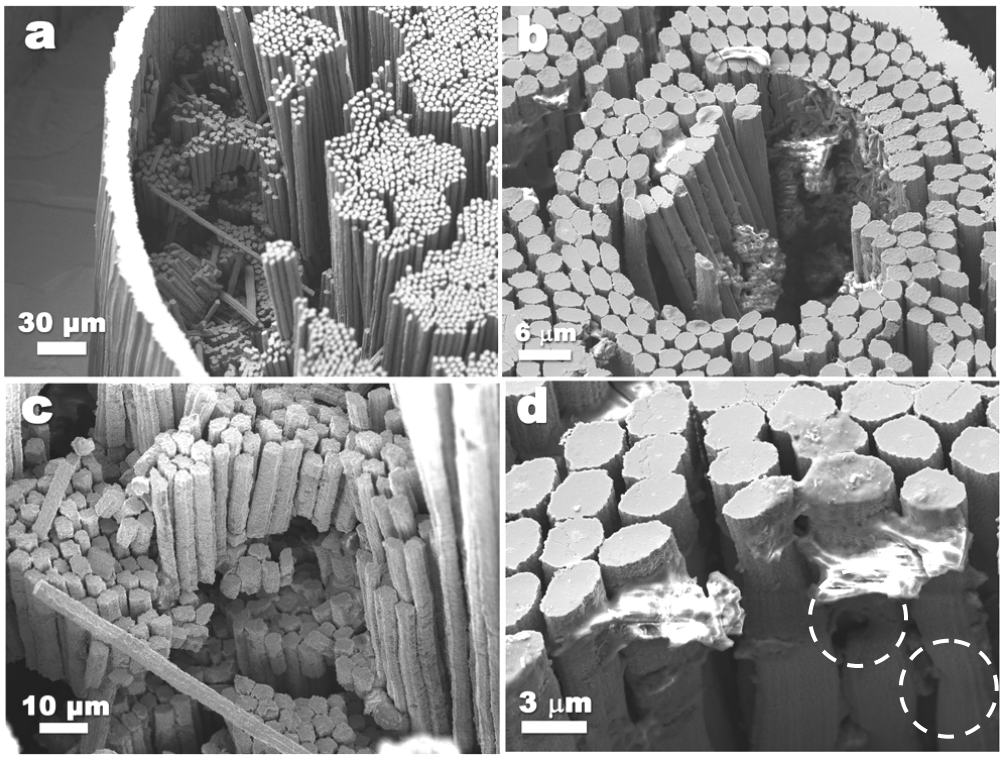

Figure 6.10. Detailed views of TARSIS samples after deep etching. Sub-figures (a) and (c) are EAS strand, and sub-figures (b) and (d) are Korean strand. The white circles in figure 18d show the location of filament sausaging in this strand.

demonstrates some mild filament sausaging (figure 6.10d). This may be from strand fabrication, but it is more likely due to filament dissolution during the heat treatment as a result of extended contact between the filaments and the corrosive Cu-Sn liquid.

6.5 Radial (longitudinal) cracks in TARSIS samples

In the course of our TARSIS investigation, we noticed a pattern of radial cracks in the transversely-polished cross-section that seemed to correlate with the presence of unreacted Nb cores. An example is shown in figure 6.11, and the effect is quantified in table 6.2, which is a summary of an analysis performed on seven central sub-bundles from an EAS strand and one central sub-bundle from an Oxford strand. Further analysis indicated that not only are the cracks associated with unreacted cores, but they are also most strongly associated with small unreacted cores (see figure 6.12) and, further, most cracks seem to propagate from the perimeter of the filament to the center.

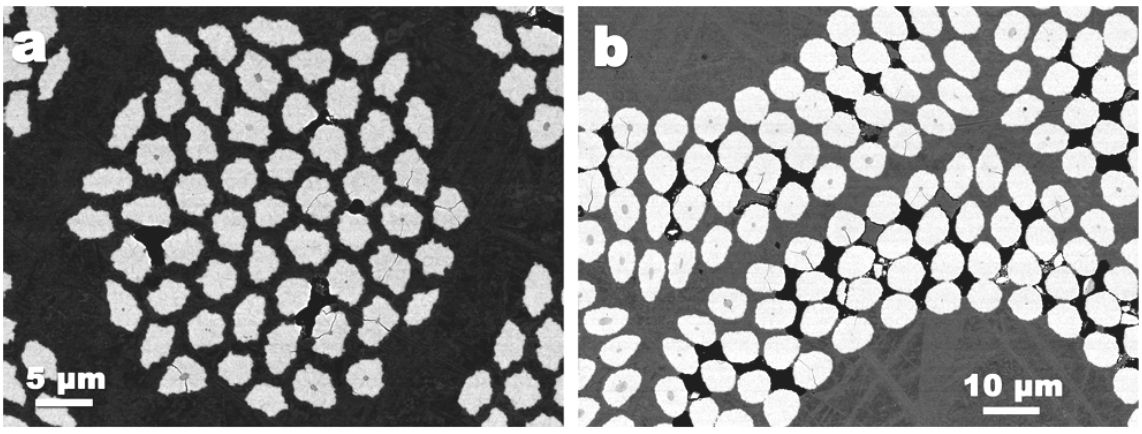

Figure 6.11. Radial (longitudinal) cracks in (a) EAS and (b) Oxford strand after TARSIS testing. Note the clear relation ship between the presence of cracks and unreacted Nb cores.

Table 6.2. Radial crack correlation with unreacted Nb cores

	EAS			OST		
	With Nb core	**Without Nb core**	**Total**	**With Nb core**	**Without Nb core**	**Total**
Number of filaments	67	318	385	257	181	438
Filaments with cracks	28	1	29	54	1	55
Total cracks	55	1	56	110	1	111
% cracked filaments	41.8%	0.3%	7.5%	21.0%	0.6%	12.6%
% of filaments represented by this column	17.4%	82.6%	100.0%	58.7%	41.3%	100.0%

While this observation is of some theoretical interest, the most relevant question for magnet performance is whether the cracks impede electric current flow and therefore reduce J_c. From a metallographic point of view, we can assess this in two ways. First, do these longitudinal cracks develop a transverse component as they propagate down the filament, thereby posing a clear impediment to current flow? Second, do these longitudinal cracks mechanically destabilize the filament, allowing for easier further damage? From our limited sample set, we answer both questions in the negative. By deep etching, we are able to track the

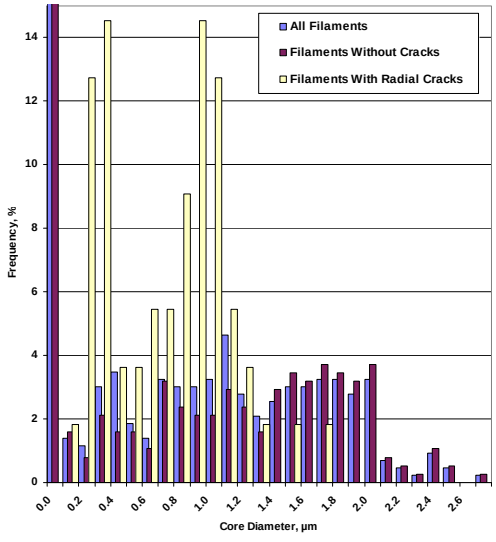

Figure 6.12. Distribution of filaments with respect to unreacted core diameter. Note that those filaments with cracks are clearly grouped in the "small" core region. Analysis courtesy Peter J. Lee.

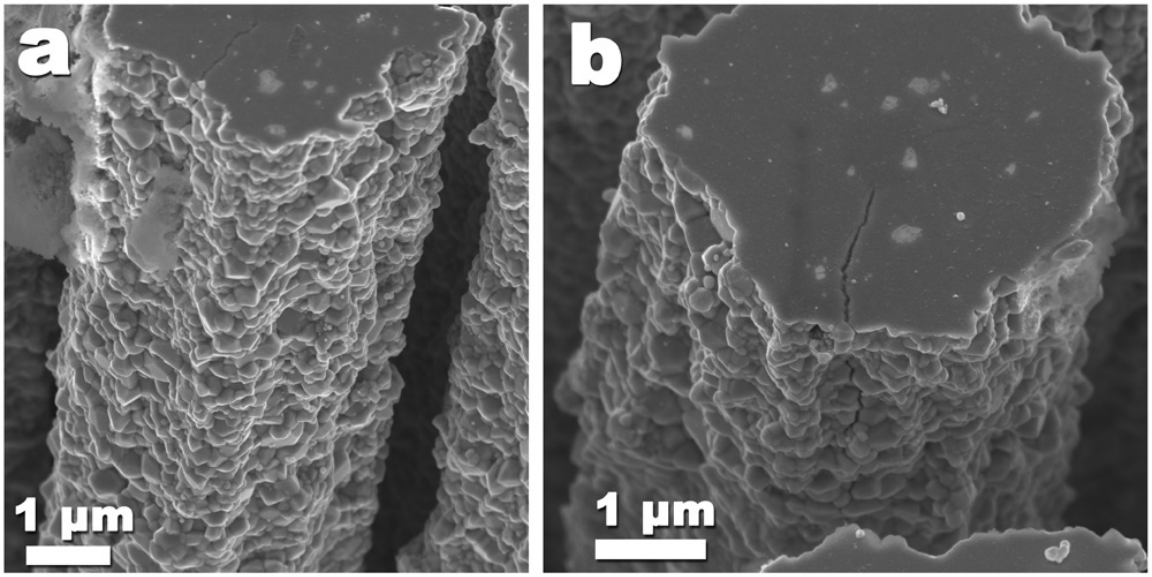

Figure 6.13. Longitudinal cracks in two etched EAS Nb_3Sn filaments. Both cracks, while propagating intergranularly, remain longitudinal and do not develop a transverse component.

progression of the cracks along the filament, and in every case (about six such filaments observed), the crack remains longitudinal, does not develop a transverse component, and does not extend spatially beyond a few microns. An example appears in figure 6.13. By deep etching, we are also able to look for examples where such radial/longitudinal cracks have caused a wedge-shaped slice of the filament to fall away after the supporting interfilamentary Cu is removed. We found no such morphology in any strand we examined (see figure 6.14). Thus, while some recent experimental I_c data from NIST [94] indicates that the irreversible strain limit improves slightly with longer heat treatment (and therefore, presumably,

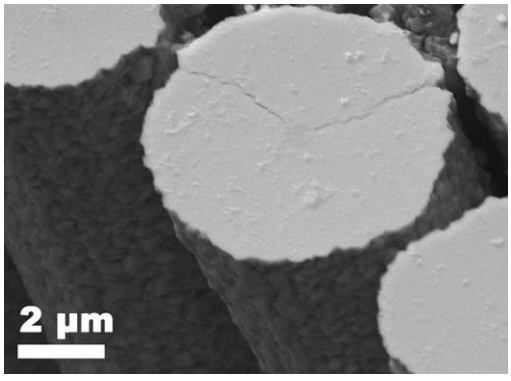

Figure 6.14. A representative radial crack in an Oxford etched filament. Note that despite the lack of supporting interfilamentary Cu, the filament does not fall apart as a result of the wedge-shaped crack.

smaller unreacted cores), we believe there is insufficient metallographic evidence to correlate these two variables at present.

6.6 Summary of TARSIS results

The TARSIS experiment is an important strand-level qualification tool for Nb_3Sn strands. Although the metallographic examination performed subsequent to this test is not amenable to quantitative analysis, a qualitative comparison of the fracture fields at the peak bending position is still possible.

Strands with more sensitive I_c degradation display more collective cracking morphologies. These are also the strands with the most agglomerated filament structures. The damage in all strands is highly localized to the peak bending strain position, even at bend strains exceeding 2%. This demonstrates very clearly the importance of maintaining compression on the filaments whenever possible. Polishing near the peak *compressive* bend strain position never reveals a damaged filament structure.

A deep etching technique developed for this experiment is a useful tool for imaging the three-dimensional nature of the fracture damage in bronze conductors. In our study, EAS strand tended to fracture in groups of 10 – 40 filaments, while Hitachi strands tended to fracture more homogeneously. Radial (longitudinal) cracks are produced during testing by the presence of unreacted Nb cores. However, our limited metallographic analysis suggests that these cracks do not contribute significantly to I_c degradation.

CHAPTER 7 – STRAND AND BULK FRACTURE TOUGHNESS

The fracture behavior observed in bending, uniaxial, and electromechanical testing has demonstrated some common features. Here, we extend that technique to evaluate the fracture propensity under indentation of the four candidate strands being investigated. Microhardness indentation [95] is a common technique for evaluating the strength and toughness of metals, ceramics, and composites. In this technique, a small, sharp, diamond indenter is pressed with a user-specified load onto the flat, polished surface of a metallographic sample. There are a variety of scales that may be used to assess material hardness; here we use the Vickers microhardness test, which uses a square-based pyramidal indenter with an angle of 136° between opposite faces of the indenter. The hardness value (H_V) is related to the size of the indent by the following expression:

$$H_V = \frac{F}{A} = \frac{2F * SIN(\frac{136°}{2})}{d^2} \tag{7.1}$$

where F is the force of the indent (in kg), d is the average length of the two diagonals formed by the square pyramidal indent, and A is the projected cross-sectional area of the indent on the sample surface.

7.1 Indentation of ITER-style strands

For this project, however, we are not as concerned about the absolute hardness of the composite Nb_3Sn strand as we are about the fracture morphology of the different strands subjected to a common indentation test. Longitudinal samples for two heat treatment conditions were prepared metallographically, indented with a Vickers microhardness indenter with a 100g load, and imaged using a scanning laser confocal microscope. The results are shown in figure 7.1. The reference sample here is the OST-2400 conductor. Note that the reference sample was not tested in two heat treatment conditions. Rather, both images here are at full reaction, but indented in a Cu-rich vs. a Nb_3Sn-rich area of the strand.

The most significant result from the indentation test is that the progression in fracture severity follows the same trend seen in other deformation conditions. Larger, more agglomerated filament structures (Oxford ITER and reference strand, notably) have a more catastrophic fracture pattern associated with their indent, while strands with well-separated filaments (Hitachi, EAS, Mitsubishi) have much more localized fracture patterns. In those latter three strands, the fracture field does not extend more than 5 μm in any direction from the ~25 μm indent, and the filaments appear to fracture independently. In the Oxford ITER and reference samples, the fracture field extends 10 – 20 μm beyond the indent, and the cracking from filament to filament is decidedly collective.

The reduced heat treatment was shown to significantly toughen the strand, reducing both the number and spatial extent of cracks formed by the indent. Unfortunately, the reduction in heat treatment required to produce this effect is likely to reduce J_c too much to be a practical solution for toughening strand intended for CIC magnet conductor.

The difference between the Oxford ITER fracture field and the other ITER-style conductors might suggest the indentation technique as a quality-control test for measuring strand homogeneity and consistency during procurement. However, we would argue against this position, for the following reasons.

First, although agglomerated structures produce a unique fracture pattern under indentation testing, the test is not sufficiently sensitive to this variable. For example, the Mitsubishi sample shows some agglomeration of filaments in the inner sub-bundle row, but the indentation image is not qualitatively different from the EAS

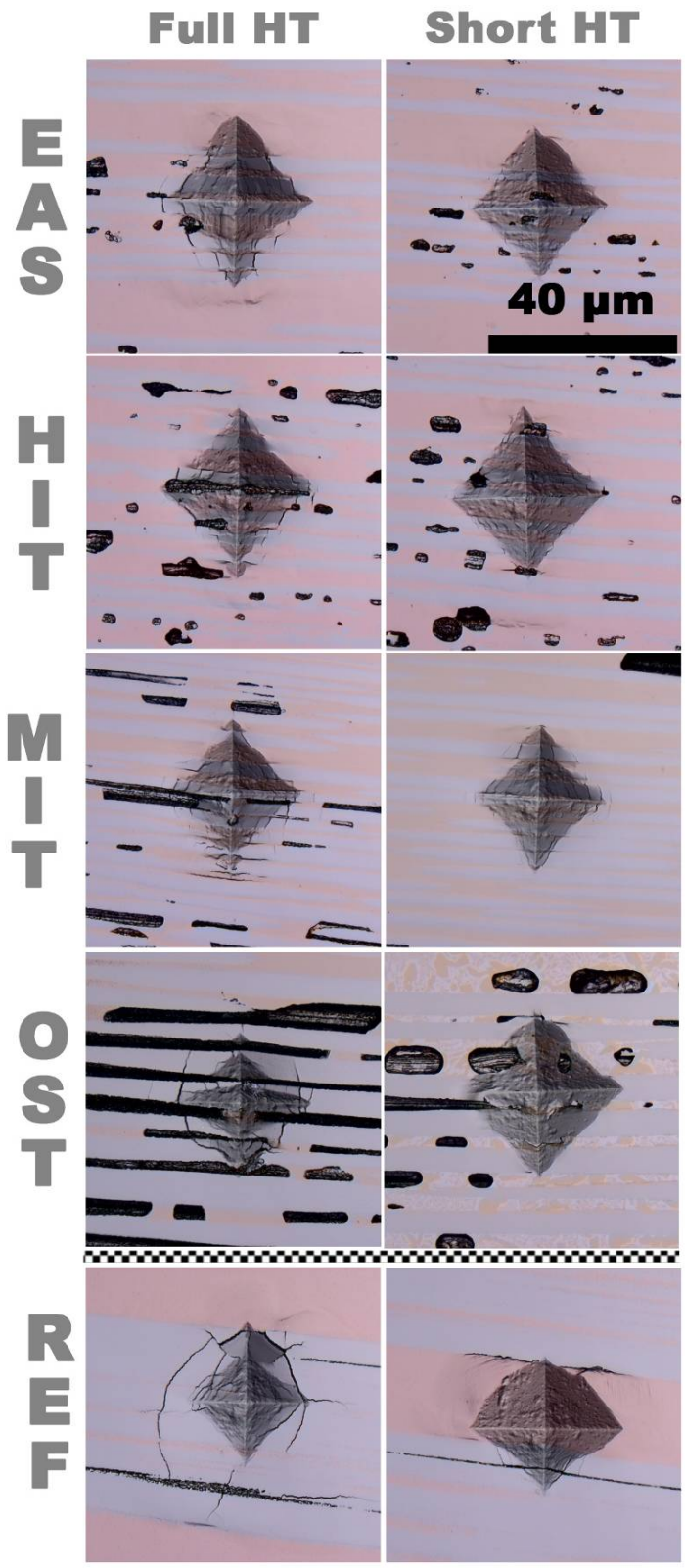

Figure 7.1 (at right). Indentation testing of polished longitudinal cross-sections of four ITER candidate strands and a reference Oxford strand. Note that the reference strand was not subjected to varying heat treatment.

or Hitachi images. Additionally, the Oxford sample, with its large filaments and higher level of agglomeration, does show a qualitatively different fracture pattern, but these architectural differences could more easily (and cheaply, from a QA testing point of view) be observed with a simple transverse cross-section of the sample. Finally, because it is a local test, the indentation technique is sensitive to the local volume fraction of Cu to Nb_3Sn. This is demonstrated graphically by the reference Oxford dipole sample. By changing the location of the indent to a more Cu-rich area, the fracture pattern is almost eliminated, despite the highly agglomerated filament structure. Generating statistically-significant results would require a large number of tests and become unwieldy.

Despite its unsuitability for quality control testing, the microhardness indentation technique can very successfully reveal the local strain state of the conductor. Figure 7.2 shows two strands (one ITER-style bronze and one HEP strand) that have been indented, each under 0.5% bend strain, with a 300g load near the tensile and compressive axes. Under compression, both strands exhibited no indentation-induced fracture, despite the larger load than the neutral (strain-free) strands shown in figure 7.1. However, under a small tensile force, both strands fracture, with the ITER bronze strand exhibiting cracks extending ~10 microns from the indent area and the HEP strand exhibiting cracks extending over 100 μm from the indent area. This result very graphically reinforces the point made earlier by the HEP strands under bend strain (section 5.1.2), which is that even a small tensile force can cause significant crack propagation through the brittle layer, but even a small compressive force can substantially suppress crack propagation. This observation is entirely consistent with the Griffith fracture criterion, which will be discussed in more detail in chapter 8.

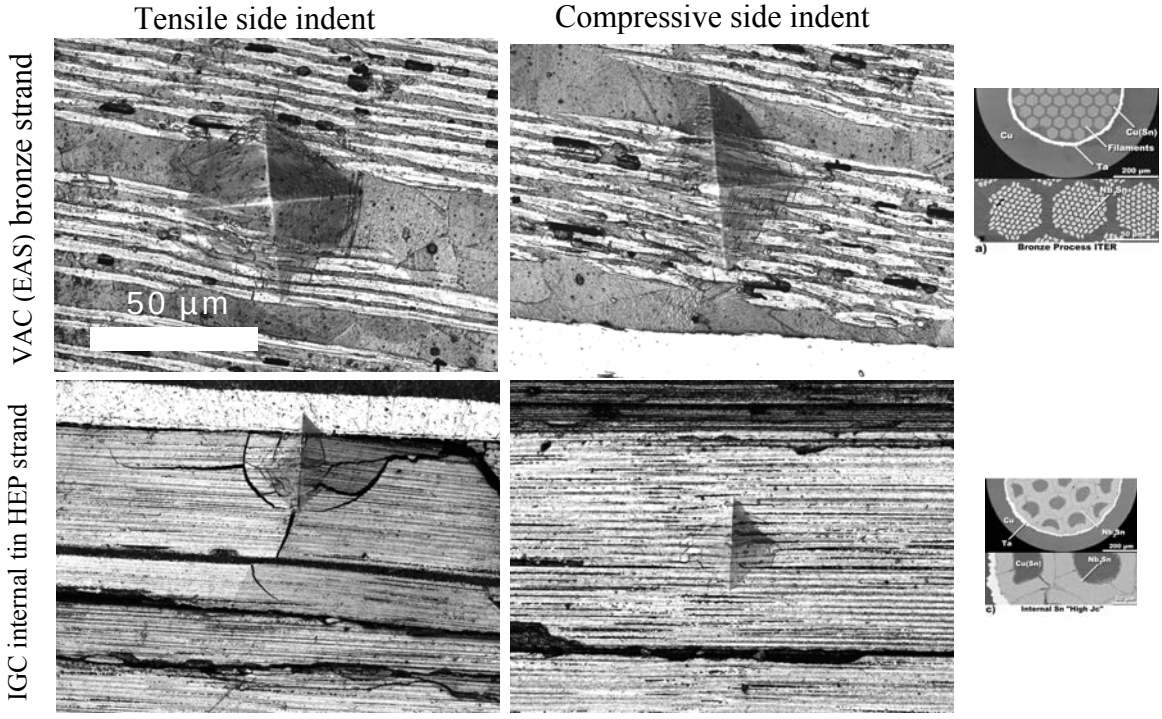

Figure 7.2. Indentation of ITER bronze and HEP strands under 0.5% bend strain, near both the tensile and compressive axes. The result is unambiguous – tensile strain significantly enhances crack formation and growth, while even a small compressive strain suppresses crack formation and growth.

7.2 Bulk indentation and fracture toughness

When designing engineering systems with brittle components, the fracture toughness of the material is an important parameter used to describe the resistance of the material to crack propagation under tensile stress. Surprisingly, there is no evidence in the extant literature that the fracture toughness of Nb_3Sn has ever been specified.

By combining our indentation technique with a set of homogeneous, bulk Nb_3Sn samples fabricated for an unrelated project [43], we have calculated K_{IC} for Nb_3Sn at room temperature by measuring the length of the cracks emanating from the indent vertices as observed in the bulk material, as shown in figure 7.3. The results are summarized in table

7.1. Here, D_1 and D_2 are the length of the diagonals of the indent, and C_1 and C_2 are the lengths of the cracks propagating from the indent vertices. We measured a room temperature hardness of 786 ± 16 kg/mm^2, and room temperature fracture toughness of 1.1 ± 0.2 MPa•m^{½}. K_{IC} is calculated according to the following relationship [96]:

$$K_{IC} = \frac{\delta\left(\frac{E}{\sigma}\right)^{\frac{1}{2}} \bullet P}{a^{\frac{3}{2}}} \qquad (7.2)$$

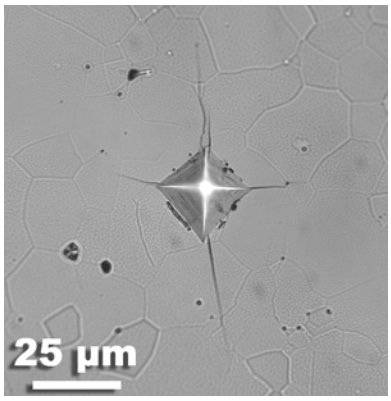

Figure 7.3 Conventional light microscope image of representative Vickers microhardness indentation in bulk Nb_3Sn. Notice the long cracks extending from the vertices of the indent, which allows for the calculation of K_{IC}.

Table 7.1 Hardness and fracture toughness testing by indentation

Indentation	D_1 (mm)	D_2 (mm)	H_v (kg/mm^2)	C_1 (mm)	C_2 (mm)
1	27.1	26.2	783	87.5	54.5
2	27.3	27.2	749	83.3	61.0
3	26.2	26.6	798	88.7	58.7
4	26.4	26.0	810	76.4	61.0
5	26.3	26.2	810	76.7	54.1
6	26.1	25.9	826	70.6	64.8
7	26.6	26.7	786	71.6	62.5
8	26.7	26.8	777	63.4	72.2
9	27.1	27.4	746	75.3	62.9
10	27.2	26.3	777	76.0	59.8
Average	26.7	26.5	786	76.9	61.2
St. Dev.	0.47	0.51	25.9	7.80	5.19
Max	27.34	27.43	826	88.7	72.2
Min	26.07	25.87	746	63.4	54.1
Count	10	10	10	10	10
95% C.I. ±	0.291	0.317	16.1	4.84	3.22
95% CI	26.7 ± 0.3	26.5 ± 0.3	786 ± 16	76.9 ± 4.8	61.1 ±3.2

In equation 7.1, δ is a technique-specific geometric variable (with a value of 0.016 for the Vickers method) E is the elastic modulus (165 GPa for Nb_3Sn at RT), and σ is the hardness, H_V, normalized to the same units (Pa) as E. P is the indentation load (in units of kgf) and a is the crack length (1/2 the average of C_1 and C_2). It should be noted that a statistically significant difference in crack lengths between C_1 and C_2 was observed, although the effect on K_{IC} is within the specified uncertainty.

The fracture toughness results obtained are very reasonable for a classic brittle material, as shown by the compilation of table 7.2 [97]. In fact, the result is very similar to that obtained for another intermetallic brittle superconductor, MgB_2 [98], and only slightly less than $YBa_2Cu_3O_{7-x}$ [99]. While the room temperature fracture toughness value may not be of use for designing magnet systems to operate at 4.2 K, it is very useful for building superconducting magnets by the react-and-wind technology [100], which is process in which the Nb_3Sn strand is heat treated on a large spool (not wound onto the magnet) with a bend radius such that the subsequent magnet fabrication procedure will not produce large strains in the now-formed Nb_3Sn.

Table 7.2 Comparison of measured K_{IC} value to engineering materials and other superconductors, adapted from [97].

Material	**K_{Ic} (MPa $m^{1/2}$)**
Concrete	0.2 – 1.4
Soda-lime glass	0.7 – 0.8
Polystyrene	0.7 – 1.1
PMMA	0.7 – 1.6
Polycarbonate	2.2
Al_2O_3	2.7 – 5.0
Al 7075	24
Al 2024	44
Ti-6Al-4V	55
4340 steel	50 – 87
$YBa_2Cu_3O_{7-x}$	1.5
MgB_2	1.3
Nb_3Sn (this work)	1.1

CHAPTER 8 – SUMMARY AND CONCLUSIONS

8.1 Summary of significant results

Using a variety of loading conditions, we have specified the strand architectural variables important to crack nucleation and propagation in Nb_3Sn composite wires. In ITER strands subjected to bending, uniaxial tension, and microhardness indentation, small and well-separated filaments have been shown to both initiate fewer cracks and propagate fewer of those cracks to adjacent filaments. There is a strong correlation of crack location to tensile strain (in bending), and this cracking occurred primarily at local bend strain values above 0.7% for strands with reacted filaments of 3 – 4 μm diameter (EAS, Hitachi, and Mitsubishi), and at local bend strain values above 0.4% for strands with reacted filaments of 6 μm diameter (Oxford). In uniaxial tension, smaller filaments (EAS, 4 μm diameter) are shown to have a significantly higher fracture onset threshold (> 0.7% tensile strain) than larger filaments (Oxford, 6 μm diameter, 0.4% - 0.5% tensile strain). Under indentation tests, the fracture field surrounding larger, more agglomerated filaments has a significantly larger spatial extent (10 – 20 μm) than that surrounding the smaller and non-agglomerated filaments (~5 μm).

The high J_c, high energy physics strands, by contrast, exhibited long, collective cracks under bending that propagated across entire sub-bundles and even from sub-bundle to sub-bundle, beginning at the tensile bend axis and ending near the geometric neutral bend axis. Additionally, the fracture morphology was shown to change minimally for a wide variety of HEP strands, with J_c (12 T, 4.2 K) values ranging from 1700 A/mm^2 to 3000 A/mm^2.

8.2 Implications for strand design

For all the strands studied (ITER and HEP designs) the most obvious and significant implication of the fracture behavior observed is the importance of maintaining compressive strain on the filaments whenever possible. This is made clear by the fracture distribution in the bend test samples (figure 5.3) and by the lack of damage under indentation when compressive strains are present (figure 7.2). On the one hand, maintaining an environment of compressive strain can be accomplished at the cable or magnet level, but for CIC applications, there is a significant subtlety which requires some attention to the strand, as well. In principle, the pre-strain on a CIC conductor can be increased by using a jacket material that contracts more (upon cooling) than does the Cu/Nb_3Sn composite strand. However, results by Martovetsky [81] show that using a jacket with a larger thermal contraction, while increasing the total compressive strain on the strand bundle (as measured by a decrease in the initial I_c of the cable relative to a jacket with lower thermal contraction) does not reduce the susceptibility of the conductor to I_c degradation after cyclic loading. This intriguing result can be understood in the context of the complicated, multi-stage cable architecture that characterizes CIC conductors. As demonstrated by the FEMCAM model of

CIC performance [25], the twisted, open structure of a CIC system implies that an imposed global pre-strain (by a cable jacket, for instance), will not necessarily result in an increased pre-strain *locally* in each strand. Because the strands in the cable are twisted and because there is void space in the cable, the pre-strain from the jacket can not be effectively transferred to each strand uniformly. This means that even with a large thermal pre-strain from the jacket, some sections of strand will not see the fracture toughness benefit of this imposed strain, and will still be susceptible to fracture under Lorentz loads. With this in mind, then, an aggressive jacket pre-strain is not the optimal design choice for fracture management. On the one hand, it decreases the reversible J_c by imposing a global strain [55] on the system, but the corresponding benefit of increased fracture toughness is not fully realized.

For this reason, a strand-level strain management approach is necessary to augment the cable-level approach. One such approach is to sheath the superconducting wire with a stiffer, higher thermal contraction material that will both provide additional pre-strain upon cooling to operating temperature and provide additional stiffness to resist deflection of the unsupported sections of strand in the cable. Dispersion strengthened copper (Glidcop), for instance, has a cryogenic strength 20% greater than OFHC Cu, and a Glidcop-sheathing approach is being pursued by, for example, Oxford Instruments [89]. Unfortunately, the costs of using such a sheath are not negligible, nor are there significant thermal contraction benefits with respect to OFHC Cu.

Managing the strain environment of the strand, then, is one approach to building additional fracture toughness into the strand. However, the results for the ITER strands also

clearly demonstrate the importance of filament size and spacing on the final fracture toughness of the composite. This is entirely consistent with established fracture mechanics approaches that consider the probability of fracture to be a function of the distribution of internal flaws in the material. One of the most widely useful approaches is the Weibull distribution [101], which predicts the probability of fracture as a function of element volume and stress. A variety of parametric approaches can be applied to the Weibull distribution, but the fundamental volume dependence is:

$$F(V) = 1 - EXP\left(\frac{-V}{V_0}\right) \tag{8.1}$$

Where $F(V)$ is the probability of fracture in a given sample volume and V_o is a volume normalization that can be interpreted as the average volume per internal defect. As a function of V/V_0, the probability relationship can be graphically expressed as shown in figure 8.1. The significant result here is that at small values of V/V_0, changes in the volume of the filament (or filament area, for a given length) will significantly impact the probability of fracture, but at large values of V/V_0, the effect

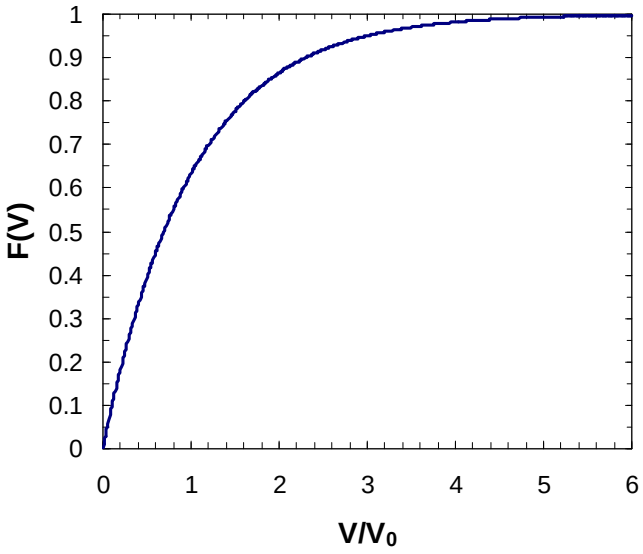

Figure 8.1. The probability of fracture in a brittle element as a function of normalized volume. Significant changes to the volume of the Nb_3Sn filaments have a significant impact on the probability of fracture at small ratios of V/V_0, but have a weak impact on fracture probability at large ratios of V/V_0.

of filament size change is minimal. This is consistent with our observation of increased fracture propensity in the Oxford ITER conductor, which has filaments 3 – 4 times larger (in area) than the EAS, Hitachi, and Mitsubishi strands, and suggests that further reductions in filament size will be beneficial to the performance of the strand. This is also consistent with irreversible J_c tests on fine-filament Nb_3Sn strand [102]. Additionally, the functional form of this relationship suggests that in the large, agglomerated sub-bundles of the HEP strands (which can be over 100 μm in diameter), small reductions in the sub-bundle diameter (by increasing the size of the restack, for example) are not likely decrease the probability of fracture initiation in the material. For completeness, it should be noted that different Nb_3Sn strands (with different grain size, alloying, etc.) may have different values of V_0, though the amount of variability is unknown.

Figure 8.2 shows the change in fracture probability as a function of the change in cross-sectional area of a filament (the parameter A is the fractional increase in the filament size, relative to some arbitrary initial filament size). Thus, A = 2, A = 3, and A = 4 represent doubling,

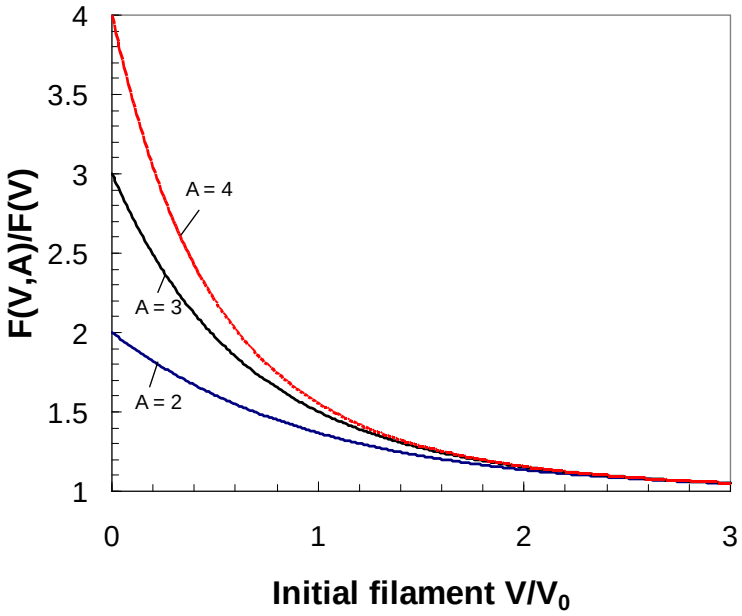

Figure 8.2. The fractional change in fracture probability as a function of initial filament size, for three different fractional increases in the filament cross-sectional area. The filaments are highly sensitive to area changes at small filament sizes, but very insensitive to changes at larger filament sizes.

tripling, and quadrupling (respectively) the filament size of some arbitrary initial filament. Note that at small values of V/V_0, the effect is significant and approaches a linear limit (e.g. tripling the filament size triples the fracture probability at $V/V_0 = 0$). At higher values of V/V_0 (larger initial filament size), the effect of further increases is weak. This reinforces the conclusion that for large agglomerated filament packs (HEP strands), changes to the sub-bundle size are unlikely to change the fracture toughness (although see the discussion in section 8.3, below), while for small filament materials (ITER strands), further reductions in the filament size could be very beneficial.

8.3 Strand design and stress concentrations

One final note should be made about the HEP strands that experienced collective fracture across the entire sub-bundle. As shown in figure 5.8, the Nb diffusion barrier around each sub-bundle is usually effective at arresting cracks at the perimeter of the sub-bundle. Nonetheless, the fracture pattern overall (see figures 5.5 – 5.7) is clearly a collective event, extending from the tensile bend axis to the neutral bend axis. The implication, therefore, is that the large crack across the sub-bundle introduces a stress concentration that locally increases the stress in the next sub-bundle, prompting initiation of a crack in that sub-bundle, and so on. Quantifying the magnitude of stress concentrations in filamentary composite materials is a significant undertaking. Highly idealized models can produce simple analytical expressions, such as assuming the material properties are homogeneous everywhere (ignoring the composite structure) or assuming the matrix material is weak and compliant relative to the fiber, and therefore carries no load and only transfers stresses via shear. This latter approach is called the shear-lag model [103] and has been applied to a variety of

material systems, including Nb_3Sn [104]. However, a careful accounting of the mechanical properties at cryogenic temperatures (table 5.1) shows that in fact Cu is actually *stiffer* than Nb_3Sn at 4.2 K, thanks to the cubic-to-tetragonal phase transition undergone by Nb_3Sn around 45 K. More sophisticated models of stress transfer that take into account the absolute differences in stiffness and strength between matrix and fiber exist for two-dimensional [105] and three-dimensional [106] systems, but in general require sophisticated finite element approaches that are beyond the scope of this thesis.

Whatever the functional form of the stress concentration, the key point (with respect to the discussion earlier in this section about filament size) is that one approach to reduce this collective fracture might be to add more Cu between the sub-bundles, which would add distance between the sub-bundles and therefore reduce the stress concentration imposed by one on its neighbor.

Also, this view of stress concentration inducing fracture modifies our conclusion in section 8.2 that, for large filaments (or agglomerated sub-bundles, in this case), changes in the filament or bundle diameter are unlikely to produce changes in the fracture probability of the material. This is still true with respect to crack *initiation*, but with respect to crack *propagation* across sub-bundles, the role of stress concentrations suggests that in fact reductions in the sub-bundle size might reduce the probability of a second sub-bundle cracking, since the stress concentration is proportional to the square root of the crack length (in the homogeneous medium approximation) [107].

8.4 Prospects for Nb_3Sn

The brittle nature of the Nb_3Sn phase is a significant impediment to its successful use as a magnet conductor in CIC systems. However, significant advancements in the cabling layout have improved the situation considerably (especially with regards to conductor for the ITER project) [108], and the results of this work suggest that the strand design can also be improved to produce a tougher wire that is more resistant to fracture and will be a realistic choice for a wider variety of CIC designs. Providing design flexibility to the CIC community is critical to maintaining the flexibility of this cabling approach to meet the demand of future magnet systems. Our results suggest that with a combination of strand-level strain management and further improvement and control over the filament size and spacing, Nb_3Sn composite wires can become a stable, robust engineering conductor for a diverse collection of high-field magnet system configurations.

REFERENCES

[1] G.B. Yntema, "Superconducting Winding for Electromagnet," *Phys. Rev.*, **98**, 1197 (1955)

[2] N.I. Salunin *et al.*, "Superconducting wires for NMR-applications," *IEEE T. Appl. Supercon.*, **32**, 2902 (1997)

[3] P. Liebyre *et al.*, "Pioneering superconducting magnets in large tokomaks: Evaluation after 16 years of operating experience in Tore Supra," *Fusion Eng. Des.*, **75-9**, 221 (2005)

[4] M. Huguet *et al.*, "The JET machine – design, construction, and operation of the major systems," *Fusion Technol.*, **11**, 43 (1987)

[5] G. Sabbi *et al.*, "Design of HD2: a 15 T Nb_3Sn dipole magnet with 35 mm bore," *IEEE T. Appl. Supercon.*, **15**, 1128 (2005)

[6] G. Ambrosio *et al.*, "Design of Nb_3Sn coils for LARP long magnets," *IEEE T. Appl. Supercon.*, **17**, 1035 (2007)

[7] D. Markiewicz *et al.*, "900 MHz wide bore NMR spectrometer magnet at NHMFL," *IEEE T. Appl. Supercon.*, **10**, 728 (2000)

[8] A very thorough overview of all the ITER systems may be found in the July 2001 issue of *Fusion Eng. Des.*, **55** (2-3), 97-357 (2001)

[9] R. Aymar, "ITER R&D: Executive summary: design overview," *Fusion Eng. Des.*, **55**, 107 (2001)

[10] Image courtesy www.iter.org, accessed 10 July 2008

[11] M. Huguet, "Key engineering features of the ITER-FEAT magnet system and implications for the R&D programme," *Nucl. Fusion*, **41**, 1503 (2001)

[12] A. Devred, "Status of ITER conductor development and qualification," oral presentation at 2007 Low Temperature Superconductivity Workshop, 29-31 October, 2007, S. Lake Tahoe, CA

[13] D. Bessette, ITER International Organization, private communication

[14] A. Godeke *et al.*, "The upper critical field of filamentary Nb_3Sn superconductors," *J. Appl. Phys.*, **97-9**, 093909 (2005)

[15] P.J. Lee and D.C. Larbalestier, "Microstructural factors important for the development of high critical current density Nb_3Sn strand," *Cryogenics*, **48**, 283 (2008)

[16] C. Sborchia *et al.*, "Design and specification of the ITER TF coils," *IEEE T. Appl. Supercon.*, **18**, 463 (2008)

[17] A. Portone *et al.*, "Design and procurement of the European Dipole (EDIPO) superconducting magnet," *IEEE T. Appl. Supercon.*, **18**, 499 (2008)

[18] A Vostner *et al.*, "Development of the EFDA dipole high field conductor," *IEEE T. Appl. Supercon.*, **18**, 544 (2008)

[19] J.R. Miller and M.D. Bird., "A new series-connected hybrid magnet system for the National High Magnetic Field Laboratory," *IEEE T. Appl. Supercon.*, **14**, 1283 (2004)

[20] I.R. Dixon *et al.*, "Performance of the ultra-wide bore 900 MHz NMR magnet at the National High Magnetic Field Laboratory," *IEEE T. Appl. Supercon.*, **15**, 1334 (2005)

[21] A.F. Lietzke *et al.*, "Test results for HD1, a 16 T Nb_3Sn dipole magnet," *IEEE T. Appl. Supercon.*, **14**, 345 (2004)

[22] N. Martovetsky *et al.*, "Test of the ITER central solenoid model coil and CS insert," *IEEE T. Appl. Supercon.*, **12**, 600 (2002)

[23] A. Vostner and E. Salpietro, "The European Nb_3Sn advanced strand development programme," *Fusion Eng. Des.*, **75-9**, 169 (2005)

[24] P. Bruzzone *et al.*, "Performance evolution of Nb_3Sn cable-in-conduit conductors under cyclic load," *IEEE T. Appl. Supercon.*, **12**, 516 (2002)

[25] Y.H. Zhai and M.D. Bird, "Modeling of the performance of Nb_3Sn CICCs for high field magnet design," *IEEE T. Appl. Supercon.*, **18**, 1127 (2008)

[26] A. Nijhuis, "A solution for transverse load degradation in ITER Nb_3Sn CICCs: verification of cabling effect on Lorentz force response," *Supercond. Sci. Tech.*, **21**, 054011 (2008)

[27] N. Mitchell, "Comparison between predictions and measurements of the superconducting performance of Nb_3Sn cable in conduit conductors with transverse load degradation," *Supercond. Sci. Tech.*, **21**, 054005 (2008)

[28] A. Nijhuis *et al.*, "Transverse load optimization in Nb_3Sn CICC design; influence of cabling, void fraction and strand stiffness," *Supercond. Sci. Tech.*, **19**, 945 (2006)

[29] J.R. Miller, presentation at 2007 ITER strand modeling workshop, 15 – 17 January 2007, Aix-en-Provence, France

[30] D. Leroy, "Review of the R&D and supply of the LHC superconducting cables," *IEEE T. Appl. Supercon.*, **16**, 1152 (2006)

[31] B.T. Matthias, "Superconductivity of Nb_3Sn," *Phys. Rev.*, **95**, 1435 (1954)

[32] M.T. Naus, "Optimization of Nb_3Sn Composite Wires," Ph.D. Thesis, University of Wisconsin – Madison (2002)

[33] R.N. Wright and G. Dixon, "The elastic modulus and flow stress of Nb_3Sn at elevated temperatures," *Met. Trans. A.*, **19A**, 1129 (1988)

[34] R.N. Wright *et al.*, "Plastic deformation in Nb_3Sn and V_3Si," *J. Metals*, **36**, 57 (1984)

[35] M. Hojo *et al.*, "Direct measurement of elastic modulus of Nb_3Sn using extracted filaments from superconducting composite wire and resin impregnation method," *Physica C*, **445-448**, 814 (2006)

[36] D.S. Easton *et al.*, "A prediction of the stress state in Nb_3Sn superconducting composites," *J. Appl. Phys.*, **51**, 2748 (1980)

[37] J.F. Bussière *et al.*, "Effects of ternary additions on Young's modulus and the martensitic transformation of Nb_3Sn," *Adv. Cryo. Eng. (Materials)*, **28**, 453 (1982)

[38] J.F. Bussière *et al.*, "Elastic behavior of polycrystalline Nb_3Sn, V_3Ga and Nb_3Ge," *Adv. Cryo Eng. (Materials)*, **30**, 859 (1984)

[39] R. Mailfert and B.W. Batterman, "Low temperature structural transformation in Nb_3Sn," *Phys. Lett.*, **24A**, 315 (1967)

[40] N. Mitchell, "Finite element simulations of elasto-plastic processes in Nb_3Sn strands," *Cryogenics*, **45**, 501 (2005)

[41] N.J. Simon *et al.*, "Properties of copper and copper alloys at cryogenic temperatures," NIST Monograph 177 (1992)

[42] J.P. Charlesworth *et al.*, "Experimental work on the niobium-tin constitution diagram and related studies," *J. Mater. Sci.*, **5**, 580 (1970)

[43] M.C. Jewell *et al.*, "The upper critical field of stoichiometric and off-stoichiometric bulk, binary Nb_3Sn," *Adv. Cryo. Eng. (Materials)*, **50B**, 474 (2004)

[44] V. Abächerli *et al.*, "The influence of Ti doping methods on the high field performance of (Nb, Ta, Ti)$_3$Sn multifilamentary bronze wires using Osprey bronze," *IEEE T. Appl. Supercon.*, **15**, 3482 (2005)

[45] J.A. Parrell *et al.*, "Nb_3Sn conductor development for fusion and particle accelerator applications," *Adv. Cryo. Eng. (Materials)*, **50**, 369 (2004)

[46] A summary of PIT drawing issues may be found in the *Research Readiness Exam* of B. Senkowicz, entitled "Progress in MgB_2 superconducting wire," University of Wisconsin – Madison (2003)

[47] A. Godeke, "Performance Boundaries in Nb_3Sn Superconductors," Ph.D. Thesis, University of Twente, Netherlands (2005)

[48] J.L.H. Lindenhovius, *et al.*, **"**Powder-in-tube (PIT) Nb_3Sn conductors for high-field magnets," *IEEE T. Appl. Supercon.*, **10**, 975 (2000)

[49] E. Barzi *et al.*, "Performance of Nb_3Sn RRP strands and cables based on a 108/127 stack design," *IEEE T. Appl. Supercon.*, **17**, 2718 (2007)

[50] S. Feher *et al.*, "Development and test of Nb_3Sn cos(theta) magnets based on RRP and PIT strands," *IEEE T. Appl. Supercon.*, **16**, 315 (2006)

[51] T. Boutboul, "Optimization of heat treatment schedule for NED PIT Nb_3Sn strand," oral presentation at 2008 WAMSDO workshop, May 19 – 23, 2008, Geneva, Switzerland

[52] V.V. Kashikhin and A.V. Zlobin, **"**Magnetic instabilities in Nb_3Sn strands and cables," *IEEE T. Appl. Supercon.*, **15**, 1621 (2005)

[53] A.K. Ghosh *et al.*, "Dynamic stability high-performance threshold in internal-tin Nb_3Sn superconductors for high field magnets," *Supercond. Sci. Tech.*, **18**, L5 (2005)

[54] D.P. Boso *et al.*, "Thermal and bending strain on Nb_3Sn strands," *IEEE T. Appl. Supercon.*, **16**, 1823 (2006)

[55] R. Flükiger *et al.*, "Long-range atomic order, crystallographical changes and strain sensitivity of J_c in wires based on Nb_3Sn and other A15 type compounds," *Adv. Cryo. Eng. (Materials)*, **30**, 851 (1984)

[56] C.B. Müller and E. Saur, "Influence of the mechanical constraints on the superconducting transition of Nb_3Sn-coated niobium wires and ribbons," *Adv. Cryo. Eng.*, **8**, 574 (1963)

[57] J.W. Ekin, "Strain scaling law for flux pinning in practical superconductors: 1. Basic relationships and application to Nb_3Sn conductors," *Cryogenics*, **20**, 611 (1980)

[58] J.W. Ekin, "Strain effects in superconducting compounds," *Adv. Cryo. Eng. (Materials)* **30**, 823 (1984)

[59] B. ten Haken *et al.*, "The strain dependence of the critical properties of Nb_3Sn conductors," *J. Appl. Phys.*, **85**, 3247 (1999)

[60] A. Godeke *et al.*, "Scaling of the critical current in ITER-type niobium-tin superconductors in relation to the applied field, temperature, and uniaxial applied strain," *IEEE T. Appl. Supercon.*, **9**, 161 (1999)

[61] D. Hampshire *et al.*, "Small reversible axial-strain window for the critical current of a high performance Nb_3Sn superconducting strand," *Appl. Phys. Lett.*, **91**, 132512 (2007)

[62] L.T. Summers *et al.*, "A model for the prediction of Nb_3Sn critical current as a function of field, temperature, strain, and radiation damage," *IEEE Trans. Mag.*, **27**, 2041 (1991)

[63] W.D. Markiewicz, "Comparison of strain scaling functions for the strain dependence of composite Nb_3Sn superconductors," *Supercond. Sci. Tech*., **21**, 054004 (2008)

[64] W. Zhang *et al.*, "Multiple fracture phenomenon of multifilamentary Nb_3Sn superconducting composite," *Mater. T. JIM*, **30**, 932 (1989)

[65] J.M. van Oort, "Critical Current Degradation in Nb_3Sn Superconductors in Accelerator Magnets," Ph.D. Thesis, University of Twente, Netherlands (2000)

[66] M.-R. Lee *et al.*, "A study of the microscopic deformation behavior of Nb_3Sn composite superconducting tape using the acoustic emission technique," *Compos. Sci. Technol.*, **64**, 1513 (2004)

[67] M. Ciotti *et al.*, "THELMA code electromagnetic model of ITER superconducting cables and application to the ENEA stability experiment," *Supercond. Sci. Tech.*, **19**, 987 (2006)

[68] Buehler 2008 U.S. Consumables Buyer's Guide, p. 25. Available for download at http://www.buehler.com/productinfo/cbg.htm

[69] R.A. Shahani, "Microstructural development during thermomechanical processing of aluminum-based composites," Ph.D. thesis, Cambridge University (1991)

[70] G. Vander Voort, *Metallography Principles and Practice*, 2nd ed., ASM International, Metals Park, OH (1984)

[71] F.M. Krill, "Vibratory polishing of metallographic specimens," *Metal Progress*, **70**, 81 (1956)

[72] E.L Long and R.J. Gray, "Better metallographic techniques…polishing by vibration," *Metal Progress*, **74**, 145 (1958)

[73] P. Rothstein and F.R. Turner, "Metallographic preparation by vibratory polishing," Symposium on Methods of Metallurgical Specimen Preparation, ASTM Special Technical Publication no. 285 (1961)

[74] D.J. Diaz, "New Concepts in Vibratory Polishing," *Microstructural Science*, **14**, 489 (1987)

[75] R. Thomas, "Acoustic Micro Imaging of Cracks," *Advanced Materials and Processes*, p. 49 June 2005.

[76] M. Di Michiel *et al.*, "Fast microtomography using high energy synchrotron radiation," *Rev. Sci. Instrum.* **76**, 043702 (2005)

[77] C. Scheuerlein *et al.*, "On the formation of voids in internal tin Nb_3Sn superconductors," *Appl. Phys. Lett.*, **90**, 132510 (2007)

[78] C. Scheuerlein, private communication, May 2008

[79] V.I. Pantsyrny, "Advances in ITER relevant NbTi and Nb_3Sn strands and low-loss NbTi strands in RF," oral presentation at 2008 WAMSDO workshop, 19 – 23 May 2008, Geneva, Switzerland

[80] J.A. Parrell *et al.*, "Development of internal tin Nb_3Sn conductor for fusion and particle accelerator applications," *IEEE T. Appl. Supercon.*, **17**, 2560 (2007)

[81] N. Martovetsky, "Effect of conduit material on CICC performance under high cycling loads," *IEEE T. Appl. Supercon.*, **15**, 1367 (2005)

[82] C.M. Fischer, "Investigation of the relationships between superconducting properties and reaction conditions in powder-in-tube Nb_3Sn conductors," Ph.D. thesis, University of Wisconsin – Madison, 2002

[83] J.C. Russ, *The Image Processing Handbook*, 5th ed., CRC Press (2006)

[84] P. Loveridge *et al.*, "Mechanical design of the Next European Dipole," *IEEE T. Appl. Supercon.*, **18**, 1487 (2008)

[85] M.T. Naus *et al.*, "Lack of influence of the Cu-Sn mixing heat treatments on the superconducting properties of two high-Nb internal-tin Nb_3Sn conductors," *Adv. Cryo. Eng. (Materials)*, **48**, 1016 (2002)

[86] M. DiMichiel and C. Scheuerlein, "Phase transformations during the reaction heat treatment of powder-in-tube Nb_3Sn superconductors," *Supercond. Sci. Tech.*, **20**, L55 (2007)

[87] M. Hansen, *Constitution of binary alloys*, McGraw-Hill, p. 634 (1958)

[88] M. Suenaga *et al.*, "Superconducting critical-temperatures, critical magnetic-fields, lattice parameters, and chemical compositions of bulk pure and alloyed Nb_3Sn produced by the bronze process," *J. Appl. Phys.*, **59**, 840 (1986).

[89] J.A. Parrell *et al.*, "Advances in Nb_3Sn strand for fusion and particle accelerator applications," *IEEE T. Appl. Supercon.*, **15**, 1200 (2005)

[90] J.A. Parrell *et al.*, "High field Nb_3Sn conductor development at Oxford Superconducting Technology," *IEEE T. Appl. Supercon.*, **13**, 3470 (2003)

[91] J. Ekin, *Experimental techniques for low-temperature measurements*, Oxford University Press, USA (2006)

[92] Y. Kubo *et al.*, "Derivation of I_c degradation rate for Nb_3Sn coils through react and wind technique," *IEEE T. Appl. Supercon.*, **14**, 991 (2004)

[93] A. Nijhuis *et al.*, "Critical current and strand stiffness of three types of Nb_3Sn strand subjected to spatial periodic bending," *Supercond. Sci. Tech.,* **19**, 1136 (2006)

[94] N. Cheggour *et al.*, "Determination of irreversible strain limits of ITER Nb_3Sn strands," oral presentation at 2007 International Cryogenics Materials Conference, 20 July 2007, Chattanooga, TN, USA

[95] D. Tabor, "Indentation hardness: fifty years on, a personal view," *Phil. Mag. A*, **74**, 1207 (1996)

[96] An introductory treatment can be found, for example in M. Meyers and K. Chawla, *Mechanical behavior of materials*, Prentice Hall, USA (1998)

[97] W.D. Callister, Materials *Science and Engineering: An introduction*, 7th ed., Wiley, (2006)

[98] S.S. Indrakanti *et al.*, "Hot isostatic pressing of bulk magnesium diboride: mechanical and superconducting properties," *Phil. Mag. Lett.*, **81**, 849 (2001)

[99] A. Leenders *et al.*, "Influence of thermal cycling on the mechanical properties of VGF melt-textured YBCO," *Physica C*, **279**, 173 (1997)

[100] P. Bauer *et al.*, "Fabrication and testing of Rutherford-type cables for react and wind accelerator magnets," *IEEE T. Appl. Supercon.*, **11**, 2457 (2001)

[101] W. Weibull, *Proc. Ing. Vetenskapsakad. Akad.*, p. 151 (1939)

[102] N. Cheggour and D.P. Hampshire, "Unifying the strain and temperature scaling laws for the pinning force density in superconducting niobium-tin multifilamentary wires," *J. Appl. Phys.*, **86**, 552 (1999)

[103] J.A. Nairn, "On the use of shear-lag methods for analysis of stress transfer in unidirectional composites," *Mech. Mater.*, **26**, 63 (1997)

[104] S. Ochiai *et al.*, "Strength distribution of filamentary Nb_3Al and Nb_3Sn compounds and its relation to mechanical and superconducting properties of multifilamentary composites: a review," *Intermetallics*, **4**, S201 (1996)

[105] P.F. Liu and J.Y. Zheng, "A Monte Carlo finite element simulation of damage and failure in SiC/Ti-Al composites," *Mat. Sci. Eng. A*, **425**, 260 (2006)

[106] M. Ryvkin and J. Aboudi, “Three-dimensional continuum analysis for a unidirectional composite with a broken fiber,” *Int. J. Solids and Struct.*, **45**, 4114 (2008)

[107] R. Solecki and R.J. Conant, *Advanced Mechanics of Materials*, Oxford University Press, 2003.

[108] P. Bruzzone *et al.*, “Results of a new generation of ITER TF conductor samples in SULTAN,” *IEEE T. Appl. Supercon.*, **18**, 459 (2008)